Dissertation

Taxis-Based Motion Control of Biohybrid Microrobots

Jiang Zhuang

2017

Submitted in partial fulfillment of the requirements
for the degree of Doctor of Philosophy.

Department of Mechanical Engineering
Carnegie Mellon University
5000 Forbes Ave
Pittsburgh, PA 15213

January 2017

Thesis Committee:
Metin Sitti, Chair
Rika W. Carlsen
Philip R. LeDuc
Radu Marculescu

Abstract

Miniaturization of on-board actuation and powering engenders the proliferation of biohybrid microrobots, which integrate motile bacteria or cells with synthetic functional components to achieve micron-scale actuations. Flagellated bacteria like *S. marcescens* are among the leading candidates for the actuators of swimming microrobots. However, the high intrinsic stochasticity in bacteria-driven microrobots severely limits their potential applications, such as targeted drug delivery. Taxis behaviors (e.g., chemotaxis), which help free-swimming bacteria to navigate towards favorable environments and away from hazardous ones, may offer an elegant means to control the motion of bacteria-driven microrobots. Therefore, this thesis focuses on: (a) addressing the motion guiding of bacteria-driven microrobots using common bacterial taxis behaviors, specifically chemotaxis and pH-taxis, (b) explaining the physical mechanisms associated with the tactic motions in bacteria-driven microrobots, and (c) developing a biophysical model to describe the bacterial propulsion and the chemotaxis in bacteria-driven microrobots.

In order to produce considerable chemotactic motion in bacteria-driven microrobots, an appropriate chemical concentration profile needs to be determined, which requires the knowledge of the chemotaxis response of the integrated bacterial species. Thus, we first propose an experimental and modeling framework to characterize bacterial chemotaxis. The chemotaxis response of a species against a chemoattractant is experimentally quantified under a linear concentration gradient of the attractant. A signaling pathway model is fitted to the experimental measurements over a series of gradients to determine the species-specific parameters in the model, thereby fulfilling an analytical characterization of the chemotaxis.

Subsequently, in a multi-bacteria-driven microrobotic system, we quantify the chemotactic drift of the microrobotic swarms towards a potent chemoattractant L-serine and elucidate the physical mechanisms associated with the drift motion by statistical trajectory analysis. It shows that the microrobots have an apparent heading preference for moving up the gradient, which constitutes the major factor that produces the chemotactic drift. The apparent heading bias is caused by a higher persistence in the heading direction when a microrobot moves up the the L-serine gradient compared to traveling down the gradient. Besides chemotaxis, we explore the potential of utilizing ambient pH to guide the motion of the bacteria-driven microrobots. Under three different pH gradients, we demonstrate that the microrobots exhibit both unidirectional and bidirectional pH-tactic behaviors. Two factors, a swimming heading bias and a speed bias, are found to be responsible for the pH-tactic motion while the heading bias contributes more. Like in chemotaxis, the heading directions of the microrobots are also significantly more persistent when they move towards favored pH regions.

Finally, a biophysical model is developed to describe the bacterial propulsion and the chemotaxis in an extensively adopted design of bacteria-driven microrobots. The model traces helical trajectories and chemotactic motion that resemble those observed from experiments, which validates the basic correctness of the model. The model simulation also suggests that the seemingly collective chemotaxis among the multiple bacteria attached to a microrobot could be explained by a synchronized signaling pathway response among these bacteria. Furthermore, we investigate the dependencies of the microrobots' performances on their system parameters, towards an optimized design of the biohybrid system.

Acknowledgments

First, I would like to thank my advisor, Dr. Metin Sitti, for his support and help over my research towards this thesis. He enlightened me on the subject of microrobotics and kept advising me on my research. To my committee members Rika W. Carlsen, Phillip R. LeDuc, and Radu Marculescu, thank you for your precious time and invaluable comments on my thesis, which definitely helped me improved the thesis work substantially. I specially want to thank Dr. Rika W. Carlsen for her continuous help on my research; as a mentor during my early-stage PhD, she taught me a proper way to conduct scientific research and helped me gain hands-on experiences with biological experiments.

I would also like to thank all my labmates in the NanoRobotics lab at CMU for their enormous comments and inspirations throughout my PhD research, and being with them also greatly enriched my campus life. To several of them whom I had the opportunity to collaborated with and published together, including Guo Zhan Lum, Eric Diller, Matthew R. Edwards, Cecile Pacoret, and Rika W. Carlsen, thank you for your help along our collaborations, and I enjoyed the experiences of working with you. I appreciate all the helps from my colleagues in the Physical Intelligence Department during my short stay there, and special thanks to Dr. Byung-Wook, Dr. Babak Mostaghaci, and Oncay Yasa for collaborating with me on research projects. I also had the opportunity to collaborate with Prof. Marculescu's group; thanks to Dr. Guopeng Wei and Dr. Paul Bogdan for their contributions in the collaborated work.

Resources and support provided by CMU are essential for my improvement in knowledge and skills during my PhD study; I would like to thank all the faculty and staff members at CMU, especially those in the Department of Mechanical Engineering and Office of International Education, for their education and administrative support. A special thanks to my academic advisor Chris Hertz for navigating me through the PhD degree program. I appreciate the financial support from the National Science Foundation (NSF) Cyberphysical Systems (CPS) program (grant number: CNS-1135850) for this thesis.

Finally, I thank most heartily of my family members, especially for the everlasting love and support from my parents and the continuous encouragement and support from my wife.

Contents

Abstract iii

Acknowledgments v

List of Figures viii

List of Tables xi

Nomenclature xii

1 Introduction 1
- 1.1 Motivation . . . 1
- 1.2 Literature Survey . . . 5
  - 1.2.1 Mobile Microrobots . . . 5
  - 1.2.2 Biohybrid Microrobots . . . 7
  - 1.2.3 Control of Biohybrid Microrobots . . . 9
  - 1.2.4 Model of Bacteria-Driven Microrobots . . . 11
- 1.3 Research Objectives . . . 12
- 1.4 Contributions . . . 14
  - 1.4.1 Contributions in Microrobotics . . . 15
  - 1.4.2 Contributions in Microfluidics . . . 16
  - 1.4.3 Contributions in Biophysics . . . 16

2 Characterization of Bacterial Chemotaxis 18
- 2.1 Introduction . . . 18
- 2.2 Analytical Models . . . 20
  - 2.2.1 Full Chemotaxis Pathway Modeling . . . 20
  - 2.2.2 Bacterial Transport Model . . . 25
- 2.3 Three-Channel Concentration Gradient Generator . . . 27
  - 2.3.1 Configuration of the Concentration Gradient Generator . . . 27
  - 2.3.2 Diffusion Time Calibration and Concentration Profile Probe . . . 28
- 2.4 Visual Tracking and Trajectory Analysis . . . 29
  - 2.4.1 Image Acquisition and Visual Tracking . . . 29
  - 2.4.2 Trajectory Analysis . . . 31

2.5 Framework Demonstration and Results . . . 33
2.5.1 Materials and Experiment Settings . . . 33
2.5.2 Characterization Results . . . 34
2.6 Discussion and Summary . . . 40
2.6.1 Discussion . . . 40
2.6.2 Summary . . . 45

3 Chemotaxis of Bacteria-Driven Microrobots 47
3.1 Introduction . . . 47
3.2 Bacteria-Driven Bio-Hybrid Microrobot . . . 49
3.2.1 Configuration and Propulsion Model . . . 49
3.2.2 Characteristics of Motion . . . 51
3.2.3 Prototyping Bacteria-driven Microrobots . . . 51
3.3 Chemotactic Response of *S. marcescens* to L-serine . . . 53
3.4 Chemotactic Drift of Microrobotic Swarms . . . 56
3.4.1 Experimental Setup and Conditions . . . 56
3.4.2 Drifting Process . . . 56
3.4.3 Probability Distribution at Final State . . . 60
3.5 Visual Tracking and Trajectory Analysis . . . 61
3.5.1 2D Tracking of Microrobots . . . 61
3.5.2 Trajectory Analysis . . . 61
3.6 Physical Mechanisms of Chemotaxis in Microrobots . . . 65
3.6.1 Heading and Speed Biases . . . 65
3.6.2 Direction Reversing Rate Bias . . . 66
3.6.3 Effect of Speed on Chemotaxis . . . 67
3.7 Discussion and Summary . . . 68
3.7.1 Discussion . . . 68
3.7.2 Summary . . . 71

4 pH-Taxis of Bio-Hybrid Microrobots 73
4.1 Introduction . . . 73
4.2 pH Gradient Calibration . . . 75
4.3 pH-Taxis of Free-Swimming Bacteria . . . 77
4.3.1 Bacterial Bidirectional pH-taxis . . . 77
4.3.2 Bacteria Tumble Rate Distribution . . . 79
4.4 pH Tactic Drift of Microrobotic Swarms . . . 79
4.4.1 Bidirectional Tactic Drift . . . 81
4.4.2 Unidirectional Tactic Drift . . . 81
4.5 Phenomenological Mechanisms of pH-Taxis in Microrobots . . . 83
4.5.1 Tracking of Microrobots and Trajectory Analysis . . . 83
4.5.2 Heading Bias . . . 85
4.5.3 Speed Bias . . . 87
4.5.4 pH Tactic Drift Velocity . . . 88
4.5.5 Direction Reversing Rate Bias . . . 89

4.5.6 Dependence on Speed . . . 89
4.6 Discussion and Summary . . . 90
4.6.1 Discussion . . . 90
4.6.2 Summary . . . 93

5 Modeling Bacteria-Driven Microrobots **95**
5.1 Introduction . . . 95
5.2 Biophysical Models for Bacteria-Driven Microrobots . . . 98
5.2.1 Multi-cellular Propulsion Model . . . 98
5.2.2 Bacterial Signaling Pathway Model . . . 102
5.3 Simulation Setup and Experimental Methods . . . 104
5.3.1 Simulation Setup . . . 104
5.3.2 Prototyping Bacteria-driven Microrobots . . . 108
5.3.3 Imaging and Visual Tracking . . . 109
5.4 Model Calibration and Validation . . . 109
5.4.1 Chemotaxis of Free-Swimming Bacteria . . . 110
5.4.2 3D Motion of Bacteria-driven Microrobots . . . 111
5.4.3 Chemotaxis of Bacteria-Driven Microrobots . . . 117
5.5 Parameter Studies . . . 123
5.6 Discussion and Summary . . . 125
5.6.1 Discussion . . . 125
5.6.2 Summary . . . 130

6 Conclusions and Future Work **132**
6.1 Conclusions . . . 132
6.2 Future Work . . . 135
6.2.1 Salt-Taxis of Bacteria-Driven Microrobots . . . 135
6.2.2 Optimize the Design of Bacteria-Driven Microrobots . . . 137

A Bacteria and Growth Conditions **144**
A.1 Serratia marcescens . . . 144
A.2 Escherichia coli . . . 144

B Microfluidic Setup **146**

C Tracking Algorithms **148**

D Microrobot Simulation Flow **153**

Bibliography **155**

List of Figures

1.1 Concept of applying bacteria-driven microrobots for targeted drug delivery. . . 3

2.1 Full signaling pathway model for bacterial chemotaxis. 24
2.2 An illustration of 1D bacterial transportation. 26
2.3 The three parallel-channel linear gradient generator. 28
2.4 Diffusion time and concentration profile calibration of the setup. 30
2.5 A sample frame showing traced trajectories of individual bacteria in the current video frame. 31
2.6 Tumble analysis of a sample trajectory. 32
2.7 Swimming speed and heading change of a sample trajectory. 33
2.8 Bacterial speed (2D) distribution. 35
2.9 Comparison of bacterial tumble rate without and with chemotaxis. 36
2.10 Dependence of the motility coefficient on the ligand concentration gradient. . . 38
2.11 Distribution of experimental datapoints. 39
2.12 Chemotactic response curve. 40
2.13 Relative gradient sensing measured from the experiment and captured by the simulation. 41
2.14 Chemotaxis migration coefficient (CMC) over concentration gradient of L-aspartate. 43

3.1 An illustration of the chemotactic guiding of bacteria-driven microrobots. . . . 48
3.2 Free-body diagram of a swimming bacteria-driven microrobot. 50
3.3 Near- and far-wall motion (2D) of bacteria-driven microrobots. 52
3.4 Fluorescent images of the prototype of bacteria-driven microrobots. 53
3.5 Chemotactic response of *S. marcescens* to linear concentration gradient of L-serine. 55
3.6 Bacterial distribution in the sample channel under the optimum concentration profile. 55
3.7 Biased distribution of bacteria-driven microrobots under a linear concentration gradient of L-serine. 57
3.8 Distribution of a swarm of bacteria-driven microrobots in the sample channel over time. 58
3.9 COM-y of bacteria-driven microrobot swarm over time. 59
3.10 Probability distribution of microrobots across the width of the sample channel at final state. 60

3.11 Sample swimming trajectories of bacteria-driven microrobots. 62
3.12 Trajectory analysis along the dimension of chemoattractant gradient. 64
3.13 The heading bias and speed bias of bacteria-driven microrobots over their swimming direction. 66
3.14 The direction reversing rate bias of bacteria-driven microrobots over swimming direction. 67
3.15 Dependence of relative reversing rate bias on mean speed. 68
3.16 The heading bias and speed bias of free-swimming *S. marcescens*. 70

4.1 Bacterial bidirectional pH-taxis away from both strong acidic and basic pH regions. 74
4.2 The microfluidic pH-gradient generator and three characterized pH-gradients. . 76
4.3 Bidirectional pH-taxis of free-swimming bacteria. 78
4.4 The biased bacterial tumble rate over their swimming direction under pH gradient. 80
4.5 Bidirectional pH-tactic drift of bacteria-driven microrobots. 82
4.6 Probability distribution of the microrobot position across the width of the sample channel under the Gradient 1. 83
4.7 Unidirectional pH-tactic drift of bacteria-driven microrobots. 84
4.8 Drifting process of bacteria-driven microrobotic swarm characterized by the COM-y of the swarm. 85
4.9 Sample swimming trajectories of bacteria-driven microrobots. 86
4.10 Biased heading of bacteria-driven microrobots under a pH gradient. 87
4.11 Biased swimming speed over swimming direction under a pH gradient. 88
4.12 Heading direction reversing rate with respect to the heading direction along the y-axis. 90
4.13 Dependences of motion biases on the swimming speed. 91

5.1 Bacteria-driven microrobots with a spherical body. 100
5.2 Tests of bacterial chemotaxis signaling pathway model. 105
5.3 Signal flow of the integrated model of the bacterial propulsion model and the chemotaxis signaling pathway model. 106
5.4 The bounded simulation space with a number of randomly distributed simulation agents upon initialization. 107
5.5 Different types of simulated wall effects. 107
5.6 Bacterial chemotaxis in a bounded channel with a linear attractant gradient. . . 111
5.7 Bacterial chemotaxis response over linear concentration gradient of L-aspartate. 112
5.8 Motion of microrobots propelled by a few (1-3) attached bacteria (experiment). 114
5.9 Illustration of angular velocity evaluation from the 2D projection of a helical trajectory. 115
5.10 Motion of microrobots propelled by a few (1-3) attached bacteria (simulation). . 116
5.11 MSD of bacteria-driven microrobots attached by a few bacteria. 118
5.12 Tumble reorientation angle of bacteria-driven microrobots. 119
5.13 Chemotaxis of multi-bacteria driven microrobots. 121

5.14 Dependence of the relative direction reversing rate bias of the microrobots on their swimming speed. 122
5.15 Synchronized MCP kinase activity of the multiple bacteria attached to a microrobot (simulation) 123
5.16 Chemotaxis response of microrobots over different attractant concentration profiles. 125
5.17 Performance of bacteria-driven microrobots on system parameters (simulation). 126
5.18 Unsynchronized MCP kinase activity of the multiple bacteria attached to a big microrobot (simulation). 127
5.19 Dependency of signaling pathway response on bacterial swimming speed under a linear spacial concentration gradient. 130

6.1 Distribution of microrobots in the sample channel at (a) 2 min and (b) 54 min after the initiation of the source and sink flows. 136
6.2 Effect of the number of attached bacteria on the swimming motion of bacteria-driven microrobots. 138
6.3 Idealized sequence of events in a tumble caused by the reversal of a single motor. 140

A.1 A plate culture of *S. marcescens*. 145

B.1 Three-channel microfluidic concentration gradient generator. 147

D.1 Simulation procedure of bacteria-driven microrobots. 154

List of Tables

2.1 Key parameters used in signaling pathway model simulation 34

5.1 Average propulsive force and torque 113

Nomenclature

$+x$	Positive direction of x-axis
$+y$	Positive direction of y-axis
$+z$	Positive direction of z-axis
$-x$	Negative direction of x-axis
$-y$	Negative direction of y-axis
$-z$	Negative direction of z-axis
$[L]$	Ligand concentration
α	Free energy contribution coefficient
α	Speed ratio
β	Heading ratio
β	Linear phosphorylation coefficient
η	Dynamic viscosity of water
$\frac{dC}{dx}$	Concentration gradient
μ	Motility coefficient
$\overline{C}$	Average concentration
ϕ	Average tumble angle
τ	Relaxation time
$\boldsymbol{\omega}$	Angular velocity
$\boldsymbol{\tau}$	Rotational drag torque
$\boldsymbol{F}$	Net propulsive force
$\boldsymbol{f}$	Stokes' drag force
$\boldsymbol{T}$	Net propulsive torque
$\boldsymbol{v}$	Translational velocity
a	Average activity of receptor
a	Average kinase activity
$B(x,t)$	Bacterial density at (x, t)
C	Concentration

$F(m, [L])$ Free energy difference as a function of m and $[L]$

$f_m(m)$ Methylation level dependent free energy difference

J Density flux

K_a Dissociation constant of aspartate to active receptor

k_B Demethylation rate

K_i Dissociation constant of aspartate to inactive receptor

k_R Methylation rate

m Receptor methylation level

m_0 Free energy contribution coefficient

N Number of receptors in a receptor complex

p^+ Average tumble rate up concentration gradient

p^- Average tumble rate down concentration gradient

R Radius of spherical microbeads

t Time

V_C Chemotactic velocity

V_{drift} Drift velocity

Y_p Conentration of CheYp

CCW Couterclockwise

CMC Chemotactic migration coefficient

CW Clockwise

FOV Field of view

MCP Methyl-accepting chemotaxis protein

Chapter 1

Introduction

1.1 Motivation

Although the term "microrobot" has not been defined exactly, it typically refers to controllable/guidable and possibly mobile devices whose component, workspace, or overall size is below 1 mm and down to 1 μm. Microrobots maintain the advantages of working in small spaces and/or accessing enclosed spaces via tiny openings. As such, they have been proposed for applications in various fields such as health care, bioengineering and lab-on-a-chip devices.

Constrained by the grand challenge of miniaturizing on-board actuation and powering, traditional untethered microrobots are often actuated off-board by delivering an energy field, in a form of magnetic field, laser, or acoustics, to their working spaces. Such remote actuation and control schemes not only require complex external equipments, but also may introduce non-biocompatible materials (e.g., magnets) or need special media or passages to deliver the energy field; this potentially limits their applications in certain areas, such as delivering therapeutics inside the human body. Biohybrid microsystems, which integrate motile microorganisms or contractile cells with synthetic functional components, have the potential to overcome the challenges in the miniaturization of on-board actuation and powering for mobile microrobots. Although there are cases where microrobots are specifically developed for working on

dry substrates (e.g., surfaces in air), the most likely working condition for mobile microrobots are inside liquid medium, as can be inferred from their potential applications, which are usually inside the human body or in microfluidic chips. Also, operating in a medium with higher viscosity increases the damping of microrobots and thus makes them easier to stabilize. Therefore, although biohybrid microrobots normally require a liquid medium to nourish their biological components, it does not affect their potential applications in the slightest.

The past decades has seen a proliferation of biohybrid microrobots actuated by different types of microorganisms and biological cells. Flagellated bacteria, such as *Escherichia coli* (*E. coli*) and *Serratia marcescens* (*S. marcescens*), is among the leading candidates for the actuators of mobile biohybrid microrobots, not only because of their ease of cultivation and high motility, but also due to their various environmental sensing capabilities, such as chemotaxis, which potentially offer natural ways to guide the motion of such microrobots. Another advantage of using bacteria as the actuators of microrobots is that they can be easily genetically modified, which provides an engineering approach to tune their behaviors based on application needs. To be more precise, we use "bacteria-driven microrobot" to refer to the type of biohybrid microrobots which integrate flagellated bacteria as their actuators. To improve the performance of bacteria-driven microrobots, such as motility and guidability, various design and fabrication heuristics have been explored, including patterning the bacterial attachment location on microrobots, aligning the orientation of bacterial attachment, and using different body shapes of microrobots. A very important application proposed for bacteria-driven microrobots is to be used as drug carriers for targeted delivery of therapeutics, as illustrated in Fig. 1.1. To this end, appropriate and reliable guiding approaches must be developed to control the motion of biohybrid systems. Although a number of studies have demonstrated the steering control of bacteria-driven microrobots at the single-agent level, control of such microrobots at the swarm level has remained challenging, partly because of their high intrinsic stochasticity and heterogeneity. The grand variance in the behaviors of bacteria-driven microrobots could result from

the factors such as the randomness in bacterial assembly process and the stochastic behavior of the assembled bacterial actuators.

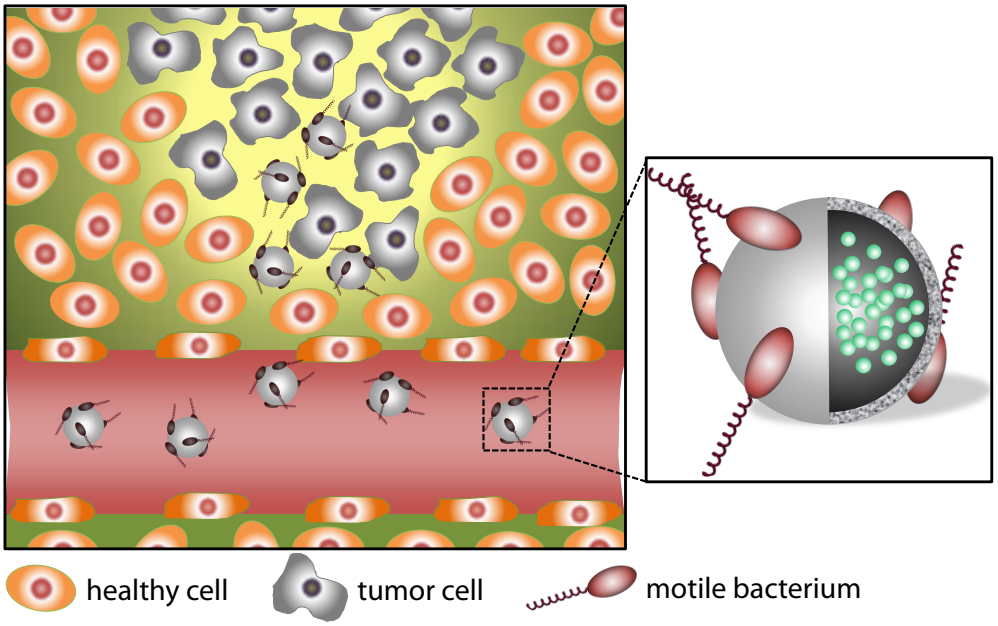

Figure 1.1: A concept of applying bacteria-driven microrobots for targeted drug delivery, where the microrobots are guided by a local chemical gradient in the site of interest, such as a chemoattractant gradient or a pH gradient.

It has been established that flagellated bacteria such as *Escherichia coli* (*E. coli*) and *Serratia marcescens* (*S. marcescens*) swim through a combination of runs and tumbles, which serve to translate and randomly reorient the cell body, respectively. In an isotropic environment, the tumble rate is uniform over all swimming directions, yielding a purely random walk in free-swimming bacteria. However, if the environment is anisotropic for bacteria, they spontaneously tune their tumble rate based on their swimming directions such that a biased random walk is performed, generating a taxis behavior. Chemotaxis is a common and well-understood taxis behavior for typical flagellated bacteria; it navigates bacteria towards favorable environments (e.g., nutrient sources) or away from hazardous ones and thus is crucial for bacterial survival. Under an appropriate concentration gradient of a potent chemoattractant, the random walk of free-swimming bacteria is changed into a biased random walk through a biased flagellar tumble

rate over bacterial swimming directions; the biased random walk associates with a chemotactic drift velocity towards the favorable direction in the gradient. Likewise, bacteria can also sense and respond to ambient pH, temperature, and salt level, producing corresponding taxis behaviors. These tactic behaviors of bacteria may offer elegant means to control the otherwise random motion of bacteria-driven microrobots. Although recent studies have observed chemotaxis in bacteria-driven microrobots, less is know about the underlying biophysical mechanisms of this behavior. In fact, the chemotaxis of bacteria-driven microrobots could be significantly different from the chemotaxis of free-swimming bacteria in that it is associated with a seemingly cooperative behavior among the multiple bacteria attached to a microrobot, and this kind of collective chemotaxis has never been studied to date.

Thus far, studies on bacteria-driven microrobots are mostly based on experiments. The development of such biohybrid systems have been heavily relied on intuitions and experimental observations, lacking a systematic method to optimize their design about the key performance indicators including motility and chemotactic guidability. The performances of bacteria-driven microrobots could be highly dependent on their system parameters, such as the concentration gradient attractant, size of microrobots, number of attached bacteria, etc. Not only is it time consuming to experiment on the entirety of these parameters, but also the experimental result is hard to generalize, since the trends applied to one specific system may work for another slightly modified one. If, instead, we could develop a biophysical model to describe the behaviors, particularly the swimming motion and the chemotaxis, of typical bacteria-driven microrobotic systems, the design optimization would be significantly easier to carry out: study the parameters of interest via the model simulation and choose the set of parameters that lead to the best performance. Such a model may not necessarily manifest every detailed aspect of a real physical system, but should describe the fundamental biophysical components of the system and reproduce the major motion characteristics observed from experiments. To build the model for a specifically designed bacteria-driven microrobots, the experimental characterizations of the

motion and the chemotaxis of the biohybrid system are essential, for model calibration and validation.

A critical prerequisite to characterize the taxis behavior, e.g., chemotaxis, of bacteria-driven microrobots is to find an appropriate environment setting that can elicit considerable tactic motion on the microrobots. Since the tactic motion of bacteria-driven systems is a result of the corresponding taxis behavior of free-swimming bacteria, it turns out that characterization of the free-swimming bacteria in response to a certain stimulus is a necessity; by which we could not only determine the potential environmental conditions for the taxis of bacteria-driven microrobots, but also fully characterize the bacterial tactic response through calibrating its signaling pathway model, if there exits one. Such a model for the bacterial taxis behavior may also be included as one component in the model of bacteria-driven microrobots.

1.2 Literature Survey

1.2.1 Mobile Microrobots

Untethered mobile microrobots have the advantages of motility in small working space, ease of deployment and potential to work cooperatively in a group or at the swarm level; these characteristics are essential for their future applications in health care, such as minimally invasive surgery and targeted drug delivery [1, 2, 3, 4, 5]. Advances in microelectromechanical systems (MEMS) during the last two decades engender the increasing developments of untethered microrobots by allowing microscale features to be fabricated using a wide range of materials. Recent technology of 3D printing at the micrometer or even nanometer level offers more freedom to the design of the functional structures of microrobots and thus is expected to promote the development of mobile microrobots. To actuate and operate the mobile microrobots, various different techniques have been proposed and developed.

Driven remotely by a rotating magnetic field, a screw-shaped micro-machine developed by

Ishiyama et al. (2001) can swim at a Reynolds number [6] smaller than swimming bacteria, though the overall size of the mcirorobot is at the millimeter scale. The screw-shaped propulsion is similar to the helical flagella which are commonly found on flagellated bacteria. In 2009, Zhang et al. fabricated an artificial bacterial flagella (ABF) using MEMS techniques [7], pushing the helical size close to its counterpart in nature, the bacterial flagella. The ABF has an length around 47 μm, and can be rotated to swim and reoriented by an external magnetic field. Using a vapor deposition method, Ghosh and Fischer further scaled the size of ABF down to 1 to 2 μm in length and demonstrated the control of the microrobot at a micrometer-level precision [8]. Tottori et al. (2012) used laser writing and e-beam evaporation to fabricate a helical structure with a load locking feature, which was also actuated and controlled by external magnetic field [9]. Different from helical propulsion, beating flagella/cilia is another common propulsive method in nature at low Reynolds number. Dreyfus et al. (2005) connected magnetic particles using DNA strands, obtained a chain structure with a length around 24 μm, and created beating patterns along the structure to propel itself in fluids by an external magnetic field [10].

Besides mimicking nature, a few studies created novel ways to achieve locomotion at the microscale both in fluids and on surfaces. Using magnetic gradient pulling method, Martel et al. (2007) and Kummer et al. (2010) demonstrated the remote 3D position control of magnets at the millimeter scale inside fluids [11, 12]. Also driven by magnetic field, a stick-slip microrobot was devised and characterized by Pawashe et al. (2009), which can both move on flat surfaces and surmount obstacles [13]. Electric fields have also been applied to actuated untethered microrobots. Donald et al. (2006) developed an MEMS microrobot which is actuated by a scratch drive actuator enabled by electrostatic forces and can move and steer on the flat driving plate [14]. A laser was used to power an impact-driven microdevice by thermal actuation, by Sul et al. (2006) [15], and to actuate a type of structured microrobots on dry surfaces relying on light deflections, by Búzás et al. (2012) [16]. Relying on light induced thermal gradients, a bubble microrobot driven by temperature gradients was developed by Hu et al. (2011) to manipulate

micro-objects in liquids for assembly tasks at the microscale [17]. Different fields can also be combined to actuate microrobots, such as the magneto-acoustic nanomotor devised by Li et al., which can be actuated by either magnetic or acoustic field or both [18]. As an example of on-board actuation, Solovev et al. (2009) used chemical reaction to generate bubbles inside a microtube, and the ejection of the bubbles propelled the microtube to swim in a fluid medium [19].

While magnetic fields are a popular way to provide remote off-board actuation for untethered microrobots, it has intrinsic limitations, which may severely limit the applications of magnetically actuated microrobots. For example, microrobots actuated by magnetic fields must contain magnetic materials, which are usually non-biocompatible and hard to collect back after deployment. Moreover, when scaling down the size of microrobots, the volume associated magnetic force decreases faster than the surface area related viscous drags do, which imposes an applicable size limitation on such microrobots. In addition, strong and high frequency magnetic fields may cause heating and bring damages to human tissues over long-time exposures, as a result of which, the application duration of magnetic fields may be limited. Other actuation methods may have their own major disadvantages for medical applications of untethered microrobots: delivery and control of laser and heating inside human body has remained challenging for effective and reliable actuation, and electric field is not only hard to deploy *in vivio* but also could induce changes in local pH level as well as potential damages to tissues.

1.2.2 Biohybrid Microrobots

To overcome the limitations of current off-board actuation techniques at the microscale, biohybrid methods have been heavily investigated over the past decade. Biohybrid microsystems, which integrate swimming bacteria [20, 21, 22, 23, 24, 25, 26, 27, 28, 29, 30, 31, 32, 33, 34, 35, 36, 37], algae [38], or contractile cells [39, 40, 41, 42] with synthetic functional components, has the potential of overcoming the grand challenges in miniaturizing on-board

actuation and power supply for microsystems. Prototypes, including swimming microrobots [22, 24, 29, 31, 32, 33, 34, 35, 36, 37, 38, 43], micromotors [23, 27, 28, 30], and microfluidic components [20, 21, 25, 26], have been extensively developed for potential applications in medicine, bioengineering, and lab-on-a-chip devices. As mobile swimming microrobots are of particular interest for use in future biomedical applications such as targeted drug delivery [1, 36, 37, 44], some major advances in biohybrid swimming microrobots are reviewed in this thesis briefly.

The first biohybrid swimming microrobots was developed using a biflagellated algae by Weibel et al. (2005). The swimming algae can carry a load with a size range of 1 to 6 μm (comparable to the size of the algae) and its swimming direction can be dictated by light [38]. Martel et al. (2006) used magnetotactic bacteria to push a 3μm bead along a preplanned path, by controlling the magnetic torque on the magnetosomes inside the bacteria [22]. In 2007, Behkam and Sitti fabricated a self-propelled microrobot by attaching multiple flagellated bacteria to a 10μm diameter microbead, and they performed on/off control on the motion of the microrobot through chemical mediated stopping and resuming of the bacterial motors [24]. Aiming to enhance the motility of bacteria-driven microrobots, Park et al. (2010) achieved selective attachment of bacteria on a certain surface of a microcube with surface patterning techniques, and an improved motility was observed on the microrobots with selective bacterial attachment [29]. Liposomes, commonly used as a drug delivery vehicle for controlled drug release, was firstly combined with motile bacteria by Kojima et al. (2012) via antibody and biotin-streptavidin to produce self-propelled liposomes [32]. Most of the studies characterized the motion of biohybrid microrobots in a condition close to surfaces or substrates, therefore the characterizations were subject to wall effects. Edwards et al. (2013) studied the far-wall motion of bacteria-driven microrobots for the first time; they found that the microrobots with a few bacteria attached traced out helical swimming trajectories, which was concluded to be produced by exerting a nearly constant force and a nearly constant torque on the microrobot [34]. Recently, motile sperm cells were utilized

by Magdanz et al. (2013) to propel a microtube wherein a sperm cell is trapped head-in [45]. *In vivo* studies of utilizing bacteria-driven microrobots for targeted drug delivery has also been conducted by Park et al. [36] and Felfoul et al. [37].

From the brief history of biohybrid microrobots, we can see that different types of cells, various shapes of the microrobots, and patterned attachment of bacteria have been investigated either to expand the scope of the design or to enhance the performance of the biohybrid microrobots. Bacteria, in particular, have several advantages as microactuators of biohybrid microrobots: (a) they typically maintain adhesion which allow for natural attachment to many materials; (b) they have versatile environmental sensing abilities which could offer potential ways to guide the motion of biohybrid microrobots; (c) they can be easily genetically engineered to fulfill desired properties; and (d) they are potentially scalable and configurable as the cells can be selectively patterned on the microrobot.

1.2.3 Control of Biohybrid Microrobots

Although it seems straightforward to harness the motility of swimming cells, by simply integrating intact cells with synthetic components, control of such systems is rather challenging, partially due to their intrinsic stochasticity and the heterogeneity among individual microrobots. Relying on external magnetic fields and magnetization of microrobots, steering control has been performed on single biohybrid microrobots with different designs. Martel et al. (2006) controlled the motion of a microbead propelled by a single magnetotactic bacterium to follow a path at an average speed of 7.5 μm/s [22]. Magdanz et al. (2013) used external permanent magnets to steer the swimming direction of a single sperm propelled microtube, which could reach a speed as high as 100 μm/s [45]. In a bacteria-driven microrobot which consists of a magnetic bead with multiple randomly attached bacteria, Carlsen et al. (2014) demonstrated the steering control of the microrobot [46]. Although the three microrobots have different designs, they share a similar actuation and control mechanism: the actuation is provided on board

by the integrated biological cells, while the control is applied by magnetically steering the body of a microrobot, which is off board.

In some applications, such as targeted drug delivery and particle sorting, control of mobile microrobots at the swarm level is required, where the microrobots may not necessarily follow a designated path but need to transport from one location to another at the population scale. Since the bacterial tactic behaviors are usually observed at the swarm level, taxis-based guiding approaches have been explored to navigate bacteria-driven microrobotic swarms. Using magnetic field, Chen et al. (2014) guided a swarm of magnetotactic bacteria in a microfluidic device to isolate pathogen [47], where the bacteria were pre-modified by an antibody to realize automatic loading of the pathogens. In a similar fashion, magneto-aerotactic bacteria were also demonstrated *in vivo* for the application of targeted drug delivery in a tumor by Felfoul et al. (2016) [37]. However, the off-board magnetic control are subject to the disadvantages that were discussed previously. Chemotaxis is a phenomenon that bacteria can respond to their local concentration changes of a certain chemical cue and choose to move to a favorable concentration of that chemical. Since concentration gradients are ubiquitous inside the human body, chemotaxis could possibly be applied to guide the motion of bacteria-driven microrobots for the medical applications such as targeted drug delivery. Chemotaxis of bacteria-driven microrobots has been reported by several studies. Traoré et al. (2011) and Kim et al. (2012) measured an increased directionality of microrobots when exposed to a chemoattractant gradient [48, 49]. Under a chemoattractant/repellent gradient, Park et al. (2014) recorded a biased distribution of bacteria-driven microrobots in a web-shaped microfluidic device [50]. A similar biased distribution of bacteria-driven microrobots was also observed by Sahari et al. (2014), in both spherical and ellipsoidal shaped microrobots [51]. Bacteria-driven microrobots whose motion is guided relying on bacterial chemotaxis has also been demonstrated for potential applications, such as for targeted drug delivery by Park et al. [36] and for particle sorting by Suh et al. [52]. Despite these remarkable results, the associated drift motion and the underlying physical mechanisms

of the chemotaxis in biohybrid microrobots have not been investigated yet. Studying of these aspects is not only crucial for a better understanding of bacteria-driven microrobots but also a necessity to model such systems and hence to optimize their designs.

1.2.4 Model of Bacteria-Driven Microrobots

The theoretical study of bacteria-driven microrobots is quite at a very preliminary stage; only a few studies have made attempts to model the type of mostly studied bacteria-driven microrobot which consists of a spherical shape propelled by multiple attached bacteria. Arabagi et al. (2011) proposed a simple linear propulsion model for the multi-bacterial propulsion in the biohybrid system [53]. However, this model failed to capture the helical shaped trajectories observed by Edwards et al. [34]. Traoré et al. (2011) adopted a similar propulsion model and a classical bacterial chemotaxis model, aiming to simulate the chemotaxis observed in the bacteria-driven microrobots, but they couldn't present any results regarding to the chemotactic drift of the simulated system. Recently, Cho et al. (2015) developed a population-scale model which was constructed by assuming a stochastic bacterial propulsion from all directions and introducing an imaginary factor of propulsion bias, named "chemotactic effect", in the presence of stimuli. Although their model simulated chemotactic drift, the model is strongly phenomenon-oriented by its construction, leaving the biophysical mechanisms of the bacterial propulsion and the chemotaxis of bacteria-driven microrobots as black boxes. To understand these mechanisms and optimize the design of bacteria-driven microrobots, it is necessary to have a model which explicitly accounts for the essential biophysical components of the system and also simulates the observed motion behaviors of the system.

1.3 Research Objectives

In this thesis, our studies are based on the most widely adopted design of bacteria-driven microrobots, which are made of spherical microparticles each attached by a few flagellated bacteria, as shown in Fig 1.1. In fact, almost all of the previous experimental studies were based on this design, for the convenience of prototyping. Therefore, the term "bacteria-driven microrobot", unless stated otherwise, refers to this specific design and its prototypes throughout this dissertation.

To utilize the bacterial taxis behaviors for motion guiding of bacteria-driven microrobots, it is essential to characterize the tactic behavior of both their actuators, the free-swimming bacteria, and the bacteria-driven microrobots themselves. We propose an experimental and modeling framework to characterize the chemotaxis of free-swimming bacteria under a chemical concentration gradient. The experimental results can be used to determine the parameters in a signaling pathway model of chemotaxis, which provides an analytical characterization of the bacterial chemotaxis. The framework is supposed to be also applicable for the quantification of taxis against pH gradients or other concentration-gradient-based stimuli. The bacterial taxis characterization serves to find an appropriate concentration profile of a certain chemoattractant/repellent to study the tactic behavior of bacteria-driven microrobots. We present the materials and fabrication procedure of a bacteria-driven microrobot prototype and the necessary characterizations of the prototype. For each taxis behavior (chemotaxis and pH-taxis), we characterize the tactic drift of a swarm of such bacteria-driven microrobots, and outline the physical mechanisms of the tactic drift motion by statistical analysis on their swimming trajectories. Finally, we develop a mathematical model based on the fundamental biophysical components involved in the propulsion and the chemotaxis of bacteria-driven microrobots. The model simulation helps understand the apparent "collective chemotaxis" among the multiple bacteria attached to a microrobot and also reveals the potential dependencies of the performances of bacteria-driven microrobots on their system parameters.

The main objectives of this thesis are:

- Develop a framework to quantify the chemotactic response of bacteria under a concentration gradient of certain chemoattractant/repellent;
- Characterize the tactic drift motion of free-swimming bacteria under chemotaxis and pH taxis;
- Characterize the tactic drift motion of bacteria-driven microrobots under chemotaxis and pH taxis;
- Through motion analysis, understand the biased drifting motion associated with the chemotaxis and pH-taxis in bacteria-driven microrobots;
- Develop a bio-physical model to simulate the 3D swimming motion and the chemotaxis of bacteria-driven microrobots;
- Via model simulation, understand the chemotaxis in bacteria-driven microrobots and perform parameter study for their design optimization.

Chapter Organization

Chapter 2 introduces an analytical and experimental framework to characterize the chemotaxis in typical free-swimming flagellated bacteria. The framework is demonstrated by characterizing the chemotaxis of *S. marcescens* towards L-aspartate. Results in this chapter are adapted from published work [54, 55]. Chapter 3 characterizes the chemotaxis in a bacteria-driven microrobotic system. The physical mechanisms of the associated collective chemotaxis are elucidated by statistical analysis on the swimming trajectories of the microrobots. Results in this chapter are adapted from published work [56]. Chapter 4 introduces a new approach that utilizes the pH-sensing capability of bacteria to perform drift control on a swarm of bacteria-driven microrobots. Both an unidirectional and a bidirectional tactic drift behaviors are demonstrated. The physical mechanism of pH-taxis in biohybrid microrobots are found to be similar to that of chemotaxis. Results in this chapter are adapted from published work [57]. Chapter 5 presents

a biophysical model to describe the mechanics of multi-bacterial propulsion associated with bacteria-driven microrobots. The model, in combination with the signaling pathway model of bacterial chemotaxis, simulates the chemotaxis of bacteria-driven microrobots, and the model simulation suggests that the collective chemotaxis among the multiple bacteria attached to a microrobot could be explained by a synchronized signaling pathway response among these bacteria. The dependences of the motility and the chemotaxis of bacteria-driven microrobots on their major system parameters, suggested from the model simulation, are also presented in this chapter. Finally, a summary and future work are outlined in Chapter 6.

Bacterial cultures (*S. marcescens* and *E. coli*) and details about the microfluidic concentration gradient generator used for chemotaxis characterizations are included in the appendix. The developed visual tracking algorithms for the motion tracking of bacteria and bacteria-driven microrobots and the program flow of the model simulation are also presented in the appendix.

1.4 Contributions

Major contributions of this thesis include: (a) developing a systematic methodology for studying the chemotaxis and other chemical-based taxis behaviors of bacteria-driven microrobots as well as free-swimming bacteria, (b) elucidating the physical mechanisms of the chemotactic and pH-tactic drift in bacteria-driven microrobots, (c) developing a biophysical model to describe the motion and the chemotaxis in bacteria-driven microrobots, and (d) predicting a possible driving mechanism of the collective chemotaxis of the multiple bacteria on a microrobot. With the proposed driving mechanism for the collective bacterial chemotaxis, results and conclusions in this thesis may engender broad interest in the disciplines of biology, bio-physics and engineering for follow-up studies. In addition, this thesis presents an experimental and modeling framework to characterize bacterial chemotaxis, which enables more accurate quantification of chemotaxis in flagellated bacteria. Finally, the proposed biophysical model for bacteria-driven microrobots could be extended to describe other designs of bacteria-driven microrobots and different types

of stimuli, and our simulation results would be helpful for optimizing the design of bacteria-driven microrobots to enhance their tactic behaviors.

In summary, this thesis is expected to provide contributions to the areas of microrobotics, microfluidics, and biophysics.

1.4.1 Contributions in Microrobotics

Motion guiding of bacteria-driven microrobots:

- Empirical determination of the optimal concentration profiles of L-serine and L-aspartate for the motion guiding of bacteria-driven microrobots;
- Specification of the pH gradients to realize both unidirectional and bidirectional drift control of bacteria-driven microrobots;
- Characterization of the chemotactic and pH-tactic drift processes of bacteria-driven microrobots in a microfluidic channel;
- Determination of the drift velocity of bacteria-driven microrobots by statistical trajectory analysis;
- Elucidating the physical mechanisms of the chemotactic and pH-tactic drifts in bacteria-driven microrobots;
- Corroborating the interchangeability of different taxis behaviors in the motion guiding of bacteria-driven microrobots.

Design of bacteria-driven microrobots:

- Identifying the importance of motility on the chemotaxis and pH-taxis of bacteria-driven microrobots;
- Proposing and demonstrating the approach of model-based simulation for the design optimization of bacteria-driven microrobots;

- Determination of a series of design heuristics to enhance the motility and the chemotaxis in bacteria-driven microrobots.

1.4.2 Contributions in Microfluidics

Particle transportation/sorting:

- Demonstration of targeted particle transportation by the chemotaxis and pH-taxis of bacteria-driven microrobots.

Three-channel microfluidic device

- Modification to the three-channel microfluidic device to reduce the undesired pressure-driven flows in the sample channel
- Fabrication process of the three-channel microfluidic device with an increased channel depth

Diffusion-based pH gradient in microfluidic devices:

- Generation of pH gradients in the three-channel microfluidic device by diffusion;
- Qualitative characterization of the pH gradients *in vitro* in the device using pH indicators.

1.4.3 Contributions in Biophysics

Bacterial taxes:

- Development of an analytical and experimental framework to characterize bacterial chemotaxis;
- Characterization of the chemotactic response of *S. marcescen* to L-aspartate;
- Characterization of the chemotactic response of *S. marcescen* to L-serine;

- Characterization of the chemotactic response of *E. coli* to L-aspartate;
- Observation of the unidirectional and bidirectional pH-taxis of *S. marcescens*.

Collective chemotaxis in microrobots:

- Developing a drift velocity model for 1D random walk and applying it to tactic drift analysis;
- Elucidating the physical mechanisms of the chemotactic and pH-tactic drifts in bacteria-driven microrobots;
- Development of a biophysical model to describe the multi-bacterial propulsion and the chemotaxis in bacteria-driven microrobots;
- Suggesting that the collective chemotaxis among the multiple bacteria on a microrobot could be explained by a synchronized signaling pathway response among the bacteria.

Chapter 2

Characterization of Bacterial Chemotaxis

2.1 Introduction

Flagellated bacteria have been actively explored as an integral part of biohybrid microsystems [20, 23, 24, 26, 27, 28, 29, 30, 31, 32, 33, 34, 40, 43, 48, 49, 53, 58, 59, 60, 61, 62], where the bacteria provide on-board actuation by transforming chemical energy into mechanical motions. Among the studied species, *S. marcescens* has shown promise to become an on-board bio-actuator due to its surface adhesion properties [63] and high motility [20]. Since chemotaxis of bacteria constitutes a potential way to guide the motion of bacteria-driven microrobots, several groups have demonstrated varying levels of chemotaxis-based control [48, 49, 50, 51]. However, these studies are empirical in nature because the chemotaxis of the associated bacteria has not been well-characterized. To bridge this gap, we propose an experimental and modeling framework for studying the bacterial chemotaxis under a stable linear concentration profile of a chemoattractant/chemorepellant, in a fashion that produces more accurate quantification of bacterial chemotaxis and is helpful to study the chemotaxis-based motion guiding of bacteria-driven microrobots. We characterize the chemotaxis of *S. marcescens* towards a canonical chemoattractant L-aspartate along with the introduction of the framework, but the bacterial species and/or the chemoattractant can be readily replaced for new characterizations.

The swimming behavior of flagellated bacteria is highly dependent on the arrangement of flagella on the cell body [64, 65]. *S. marcescens*, like *E. coli*, is a kind of peritrichous bacteria that can form a flagellar bundle to obtain self-propulsion [20, 65]. The chemotactic behavior of *E. coli* or *S. marcescens*, can be explained by studying the motion of individual bacteria. Swimming trajectories of *E. coli* in a liquid environment have been tracked by Berg and Brown using a 3D tracking microscope [66]; the tracked trajectories are composed of smooth directional runs that are interrupted by short periods of tumbles. The running state corresponds to the rotation of the flagella in a counterclockwise direction (CCW), while the tumble state corresponds to a clockwise (CW) rotation of the flagella. The tumble events help bacteria randomly reorient their swimming directions. In an isotropic environment, the tumble rate is the same in all swimming directions, yielding a persistent random walk in free swimming bacteria. For *E. coli*, the average value of the tumble rate was measured to be 1.2 s^{-1} [66]. However, when bacteria are exposed to certain stimuli, like a chemoattractant gradient, the tumble rate can be preferentially decreased when swimming up the gradient [66, 67]. A directionally biased tumble rate generates a directional drift velocity, defined as the *chemotactic velocity*, V_C [68]; this helps bacteria change their persistent random walk motion into a biased random walk.

In order to create an environment suitable for studying bacterial chemotaxis, various microfluidic assays have been developed [69, 70, 71, 72, 73, 74, 75, 76]. Among them, the three-channel gradient generator has been extensively used in recent chemotaxis studies [49, 70, 71, 72, 76, 77] since it eliminates the flow-induced force on bacteria. Consequently, we apply the design of the three-channel device in the characterization framework. For the three-channel gradient setup, a biased distribution in bacterial population can usually be observed in experiments and chemotactic response is evaluated by the chemotaxis migration coefficients (CMC) [70, 71, 76, 77]. However, the quantitative characterization of chemotaxis by measuring population density requires most bacteria to be motile, which is rather hard to guarantee in the experiment. In 2008, Ahmed *et al.* tried to calculate the chemotactic velocity by 2D

individual-cell tracking technique, where they used an average traveling time bias to approximate the tumble rate bias [72]. However, this approximation is not valid since the bacterial diffusion driven by the population density gradient contributes to the average traveling time asymmetry significantly. Instead, we directly measure the bacterial tumble rates with respect to their swimming directions using a bacteria tracking technique and a trajectory analysis method. By definition, the chemotactic velocity can thus be readily calculated from the tumble rates and other measured motility parameters.

In the following sections, we first introduce the major components of the characterization framework, including analytical models, microfluidic device, and tracking and analysis methods. Then, using the framework, we characterize the chemotactic response of *S. marcescens* towards L-aspartate by measuring V_C over a range of concentrations and gradients. A chemotaxis signaling pathway model is fitted to the experimental measurements and hence the major parameters in the model are determined for the species, fulfilling an analytical characterization of the chemotaxis.

2.2 Analytical Models

In this section, two models, the chemotaxis pathway model and bacterial transport model, are presented. The chemotaxis pathway model describes the signaling transduction from bacterial sensing of local concentration to flagellar dynamics. The transport model is for better understanding of bacterial transportation at the population level, and it introduces the chemotactic velocity, V_C.

2.2.1 Full Chemotaxis Pathway Modeling

Here, we describe the most widely used models for the bacteria chemotaxis pathway. In general, the chemotaxis pathway has three components: the cooperative chemoreceptor, the phosphory-

lation pathway, and the flagellar motor [78]. The chemoreceptor senses extracellular concentration changes and transduces the signal to a intracellular regulator, which regulates the tendency of flagellar motor rotation direction. For each component, there are several models available which have been used in various studies [77, 79, 80, 81, 82]. In the following subsections, we will discuss the applicability of these models in the chemotaxis characterization framework.

Cooperative chemoreceptor cluster

To describe the cooperativity of chemoreceptors, the Ising and Monod-Wyman-Changeux (MWC) models are commonly used [78]. The Ising model is based on the conformational spread of receptor proteins [83]. Specifically, it models the individual receptors and the interactions among them in a way that the states of the receptors tend to agree with each other, therefore showing high cooperativity in the receptor clusters. Due to the nature of this individual receptor based approach, the Ising model is suitable for single cell evaluations, but the computational requirements become prohibitive for population level simulations. The MWC model (also known as the concerted model or symmetry model) describes the allosteric effects of receptor clusters that are made up of identical receptors. This high level model is concise, easy to use, and has shown very good agreement with experiments [78, 84]. Therefore, we describe next the latest MWC models with two different methylation kinetics.

The first one is the SPEC (signaling pathway-based E. coli chemotaxis) model for the chemoreceptors that captures the essential features of bacteria chemotactic activity and adaptation [77, 81]. More specifically, each functional methyl-accepting chemotaxis protein (MCP) receptor complex can be either in the active or the inactive states, which are determined by a free energy difference $F(m, [L])$, where m is the methylation level of the receptors, $[L]$ is the concentration of the ligand, and N is the number of receptor dimers in a MCP complex. We use $N = 6$ for Tar receptors in a complex; the average activity of the receptor can be expressed as

[77, 85]:

$$a = (1 + \exp(F(m, [L])))^{-1} \ . \tag{2.1}$$

According to the MWC model, the free energy difference can be written as:

$$F(m, [L]) = f_m(m) + \ln\left(1 + \frac{[L]}{K_a}\right) - \ln\left(1 + \frac{[L]}{K_i}\right) \ , \tag{2.2}$$

where $f_m(m)$ is the methylation level dependent free energy difference, and K_a and K_i are the dissociation constants of the ligand to the active and the inactive receptors, respectively. For the binding of L-aspartate onto the Tar receptors, we use the values fitted to *in vivo* FRET (fluorescence resonance energy transfer) data [77], namely, $K_a = 3$ mM and $K_i = 18.2$ μM. The impact of receptor methylation on its free energy is considered to be a linear function of m as suggested by recent experimental work [86, 87]:

$$f_m(m) = \alpha(m_0 - m) \ , \tag{2.3}$$

where $\alpha \approx 1.7$ and $m_0 \approx 1$.

The first form of methylation kinetics is based on the Barkai and Leibler model for a near perfect adaptation system [88]. More precisely, the methylation kinetics is assumed to have a linear form:

$$\frac{\mathrm{d}m}{\mathrm{d}t} = k_R(1 - a) - k_B a \ , \tag{2.4}$$

where $k_R = k_B$ are the methylation and demethylation rates, respectively; the values are determined by fitting the experimental measurements of the characterized species to the model.

The second form of methylation kinetics is based on the fact that chemotactic behavior is related to the relaxation time of the receptor-kinase activity [89, 90, 91]:

$$\frac{\mathrm{d}m}{\mathrm{d}t} = -\frac{1}{\tau}[m(t) - \bar{m}(C)] + \sigma_m\sqrt{2/\tau}\Gamma(t) \ , \tag{2.5}$$

where τ is the relaxation time, σ_m is the variance of fluctuations in the methylation dynamics, $\Gamma(t)$ is a normally distributed homogeneous random process with zero mean and unit variance, and $\bar{m}$ is the average adapted methylation level at a given ligand concentration.

In order to model the chemotactic response of a bacterial species over a wide range of chemoattractant gradients, which is typical for flagellated bacteria like *E. coli*, it it beneficial to select the model with the widest response range. In the second form of methylation dynamics, the adaptation rate is determined by the difference between the current methylation level and the average methylation level. This only applies to a shallow gradient; in a deep gradient, the adaptation rate would be unrealistically fast and unlimited due to the large methylation difference. However, in the first form of methylation dynamics, the adaption rate would be constrained, since there is a range limit of $(0, 1)$ for the receptor activity a. Specifically, in a deep gradient, the receptor activity $a(t)$ would be suppressed to 0 for a long time before its methylation level catches up and regains activity, therefore the adaptation rate will not be unrealistically high. Consequently, in our simulations, we use the first form of methylation kinetics (Barkai-Leibler type receptor model) as shown in Fig. 2.1(a) [77, 88].

Phosphorylation relay and flagellar motor

An active receptor enhances the autophosphorylation of the receptor-associated kinase *CheA*, which transmits the signal to the flagellar motors by the phosphorylation of a diffusive response regulator *CheY*. In most chemotaxis full pathway models, the concentration of phosphorylated *CheYp* is assumed to be proportional to the kinase activity, $[Y_p] = \beta a(t)$ as shown in Fig. 2.1(b), without considering the nonlinear dependence [92].

Thermal fluctuations and upstream signaling cause the flagellar motor to spontaneously change between CCW and CW states. To model the state transition, the SPEC model uses a hill function to calculate the probability of tumble with $[Y_p]$, and assumes an average fixed tumble time $\tau = 0.2$ s [77]. Specifically, when a bacterium is running, the probability of the

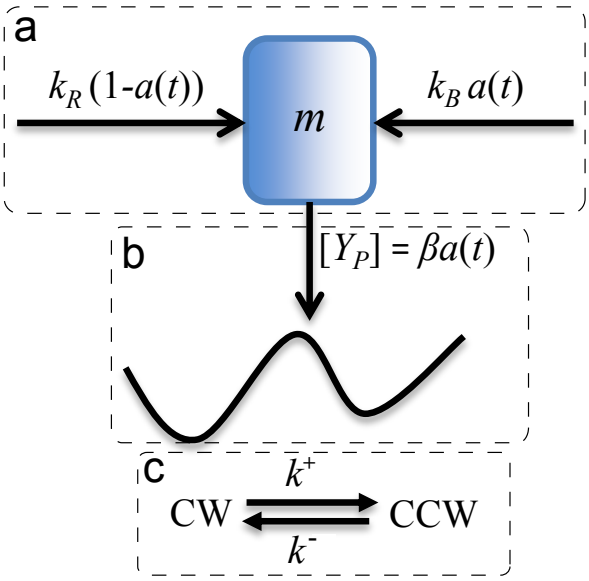

Figure 2.1: Full signaling pathway model for chemotaxis. (a) The methylation kinetics is based on the Barkai and Leibler model with a linear form: $dm/dt = k_R(1-a) - k_B a$. (b) The signal transduction from chemoreceptor to the flagellar motor regulator Y_p, where the concentration of phosphorylated *CheYp* is proportional to the kinase activity, $[Y_p] = \beta a(t)$. (c) The two-state model to describe the motor behavior of flagellated bacteria, where the transition rates of CCW to CW and CW to CCW are k^- and k^+, respectively.

cell going into a tumble state is $p(a) = \tau_1^{-1}(a/a_{1/2})^H$, where $a_{1/2}$ is a fitted constant, and H is the Hill coefficient of the motor response function. However, under some gradient conditions, the bacteria flagellar motor may stay in the tumble state for a time significantly shorter or longer than the average value, which biases the swimming dynamics considerably. Therefore, we adopt a two state potential well model to describe the motor behavior of flagellated bacteria, which sets their two states in two potential wells as shown in Fig. 2.1(c) [93].

The energy barriers of CCW to CW and CW to CCW transitions are $G_0([Y_p])$ and $-G_0([Y_p])$, with transition rates k^- and k^+, respectively [94]:

$$\begin{aligned} G_0([Y_p]) &= \frac{g_0}{4} - \frac{g_1}{2}\left(\frac{[Y_p]}{K_D + [Y_p]}\right) \\ k^+ &= w_0 \exp(G_0([Y_p])) \\ k^- &= w_0 \exp(-G_0([Y_p])) \end{aligned} \tag{2.6}$$

where parameters $w_0 = 1.3\ \mathrm{s}^{-1}$, $g_0 = g_1 = 40\ k_BT$, and $K_D = 3.06\ \mu$M are chosen to fit the experimental data [95]. The configuration of the implemented full pathway model is shown in Fig. 2.1.

2.2.2 Bacterial Transport Model

As discussed previously, in a bounded channel with chemical gradient, change in the motion of single bacterium leads to a biased distribution of bacterial density. Based on probabilistic modeling of individual bacteria, the model described in this section relates the population kinetics to the motility parameters of individual cells. The chemotactic velocity (V_C) introduced in the model quantifies the effect of chemotaxis on the bacterial population transport; by construction, V_C is directly related to the tumble rate bias of individual bacteria. Therefore, by extracting V_C from this model and determining it through tracking of individual bacteria, our approach quantifies chemotaxis from the measurement of individual cells, as opposed to most recent studies, which have made measurements at the population level [70, 71, 76, 77].

In an environment with a one-dimensional (along x direction) chemoattractant gradient, as shown in Fig. 2.2 the transport kinetics of bacteria density can be described with the following equation [68, 96]:

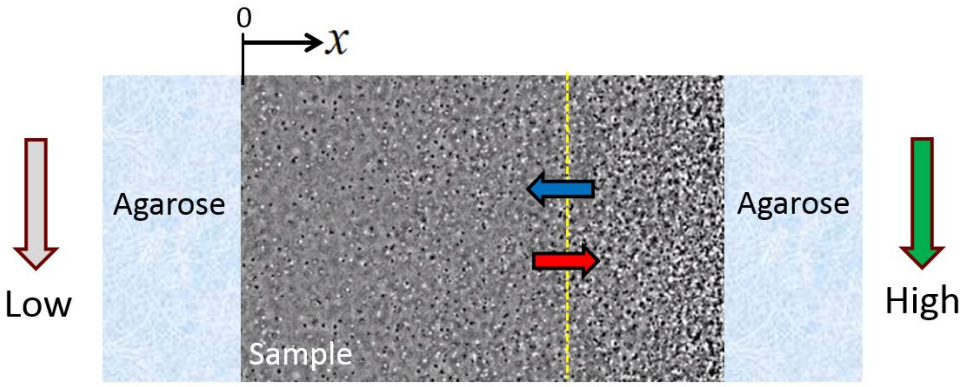

Figure 2.2: Bacterial transportation along a 1D (along the x-axis) chemoattractant gradient, in which bacteria show a biased distribution. The bacterial transportation across an arbitrary plane, denoted by the yellow dashed line, is contributed by two terms, random motility (blue arrow) and chemotactic drift (red arrow).

$$J_x = -\mu \frac{\partial B(x,t)}{\partial x} + V_C B(x,t) \,, \tag{2.7}$$

where J_x is the density flux of bacteria through a slice that is perpendicular to the x axis, μ is the motility coefficient, $B(x,t)$ is the bacteria density, and V_C is the chemotactic velocity as previously discussed. The motility coefficient, μ, similar to the diffusion coefficient, is a proportionality measure between the bacterial density flux and the gradient of the bacterial density. Bacteria transport in the channel is subject to two effects: the diffusivity motility and the chemotactic drift, which are described by the first and second terms on the right hand side of Eq. 2.7, respectively. The diffusivity motility keeps the transport of bacteria down the gradient of bacterial population density, while the chemotactic velocity pumps bacteria up the chemoattractant gradient. From the probabilistic modeling of individual bacteria, the motility coefficient and chemotactic velocity can be expressed as follows [72, 97]:

$$V_C = \frac{2(p^- - p^+)}{3(p^- + p^+)} v \ , \tag{2.8}$$

$$\mu = \frac{2v^2}{3(p^- + p^+)(1 - \cos\langle\phi\rangle)} \ , \tag{2.9}$$

where, p^+ and p^- are the average tumble rates when bacteria travel up and down the chemical gradient, respectively, v is the average 3D swimming speed of bacteria, and $\langle\phi\rangle$ is the average tumble angle, which is defined as the swimming direction change during a tumble. Instead of a simple model based on average rate processes, models based on random walk theories that consider distributions of running and tumbling durations are also available [98, 99]. These advanced models could provide a more accurate characterization of single bacterium motility and population transport if both the run and tumble durations of the characterized bacteria can be measured experimentally in the future.

2.3 Three-Channel Concentration Gradient Generator

This section introduces the concentration gradient generator and the calibrations of the setup. It has been shown that bacteria maintain different degrees of chemotactic response under different concentration gradient. In order to quantify the bacterial chemotactic response to concentration profile, it is crucial to keep the concentration profile constant over the duration of measurement. Therefore, we calibrate the time required to establish a stable linear concentration profile in the microfluidic device. A linear concentration profile also guarantees that bacteria at different locations in the channel see the same concentration gradient.

2.3.1 Configuration of the Concentration Gradient Generator

The configuration and geometry of the device are shown in Fig. 2.3. The device consists of three channels: the source, sample, and sink channel. The channels are all 500 μm wide and

around 80 μm high. They are separated from each other by two 250 μm wide agarose gel ridges. Two flows containing higher and lower concentrations of chemoattractant are pumped into the source and sink channel, respectively, by a programmable syringe pump (Braintree Scientific Inc.). The manufacturing and assembly process of the setup is described in Appendix B.

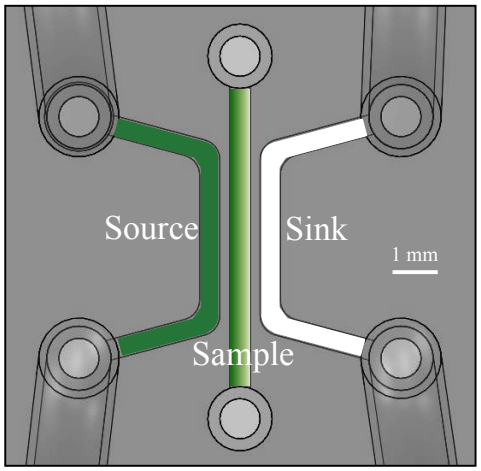

Figure 2.3: The three parallel-channel linear gradient generator. Top view of the three channels, where the green color (source side) indicates a higher concentration and the white (sink side) stands for a lower concentration. A linear gradient can be seen in the sample (center) channel at steady state.

2.3.2 Diffusion Time Calibration and Concentration Profile Probe

To calibrate the diffusion time and concentration profile in the sample channel, we observed the diffusion of 10^{-4} M fluorescein (Sigma-Aldrich Co.) solution from the source to the sink. For small molecules like fluorescein, when the concentration is lower than 10^{-3} M, the intensity of the fluorescent image is proportional to the concentration [71]. The normalized intensity profiles of the fluorescent images therefore indicate the concentration profiles. During tests, flows of fluorescein solution and deionized water (DI water) were maintained in the source and sink channels, respectively, both at a rate of 5 μL/min. The middle channel was infused with DI water manually at the onset of the test.

We acquired the fluorescent images using a fluorescent microscope (Axiovert 200, 5X A-

Plan, 0.12) and a CCD camera (AxioCam HR). The original fluorescent images in a temporal sequence are shown in Fig. 2.4(a). From the normalized intensity profiles in Fig. 2.4(b) and the linearity error plot of the profiles in Fig. 2.4(c), it can be determined that a linear gradient between the source and sink channel is generated in 20 minutes from the input of the flows. L-aspartate has a diffusion coefficient of 9.0×10^{-6} cm^2/s [74], while it is 4.25×10^{-6} cm^2/s for fluorescein. Thus we can conclude that about 10 minutes are needed for L-aspartate to generate a linear gradient. To guarantee a linear gradient in the experiments, all of the data were measured 15 minutes after the input of the source and sink flows.

2.4 Visual Tracking and Trajectory Analysis

This section introduces the methods of image acquisition, visual tracking of bacterial motion from recorded images, and trajectory analysis.

2.4.1 Image Acquisition and Visual Tracking

To record bacterial swimming motion, the chemotaxis setup was put under an inverted phase contrast microscope (Zeiss Axiovert 100, 32× or 40×, Carl Zeiss, Oberkochen, Germany) and video data was recorded by a camera (Foculus Inc.). The frame rates of the videos were around 88 frame/s and each video was 30 seconds long. Videos were taken at locations that were far from the top and the bottom walls and near the center line of the sample channel, which well eliminated the wall effects on the swimming bacteria. For each data point, at least 4 videos were taken and analyzed.

Two different in-house visual tracking programs for 2D and 3D tracking, were developed in MATLAB (R2012a, The MathWorks, Inc, Natick, MA) to analyze the video data. The basic algorithms used for the visual tracking is included in Appendix C, Algorithm 1 and Algorithm 2. The 2D tracking program can accurately capture the x-y plane projections of the

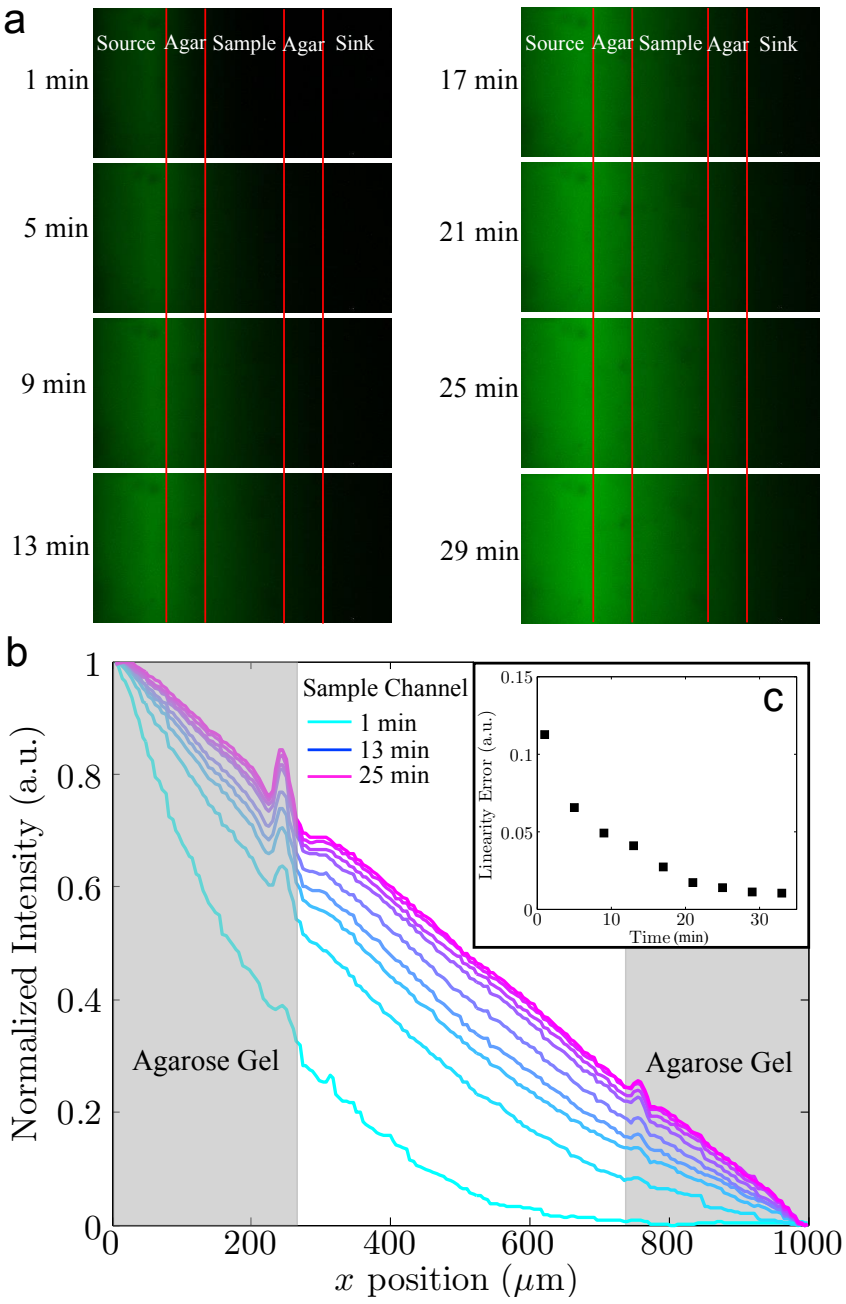

Figure 2.4: Diffusion time and concentration profile calibration of the setup. (a) Original fluorescent images across the three channels in a temporal sequence. (b) Normalized fluorescent intensity profile. The curves colored from cyan (lighter) to magenta (darker) indicate that the concentration profile of fuorescencein becomes more and more linear with elapsed time. The bumps and dips appearing at the interfaces of the gel and solution are caused by optical diffraction. (c) Linearity error of the normalized intensity profiles at different times. A linear gradient can be approximately achieved after a diffusion of about 20 minutes.

three-dimensional trajectories, which was mainly used to perform analysis of tumble rates with respect to the swimming directions. Fig. 2.5 shows the trajectories of the bacteria captured in the current frame, where the displayed trajectories are tracked from previous video frames. The 3D tracking program is able to calculate the z position with an accuracy of ± 1 μm over a range of ± 20 μm, through a calibrated linear correlation between the size of the diffraction ring and the z-axis position. The tracking method is described in greater detail in Edwards *et al.* [55]. This way, we can calculate the average 3D swimming speed and the tumble angle distribution of the observed bacteria. A total of 1000 to 1500 trajectories with lengths varying form 1 to 15 seconds could be extracted from each sample video. At each concentration profile, at least four sample videos were taken and analyzed.

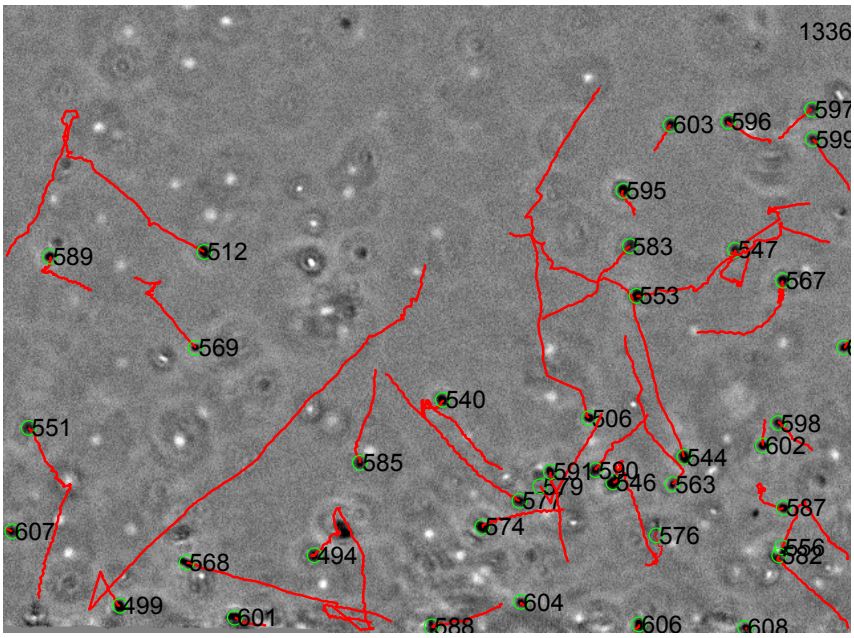

Figure 2.5: A sample frame showing traced trajectories of individual bacteria in the current video frame.

2.4.2 Trajectory Analysis

To detect the tumble events along a swimming trajectory, we apply an angle threshold (5 degrees) to the direction change between 10 frames; changes in the swimming direction that ex-

ceed this threshold correspond to tumbling events [55]. As shown in Fig. 2.6, a sample trajectory is analyzed by the program and seven tumble events are detected along the swimming trace. Fig. 2.7 plots the instantaneous 2D velocity and the heading direction change along the trajectory; it can be seen that the tumble events are normally associated with significant swimming speed changes. However, detection of tumble events based on the speed change can be misleading since it is usually very noisy during a tumble event. By such analysis, the entire information about the trajectory can be extracted, such as the instantaneous swimming direction, the swimming directions before (solid arrows in Fig. 2.6) and after a tumble (dashed arrows in Fig. 2.6), and the location of the tumble (T_i). Since the swimming bacteria in the microfluidic device only experience concentration gradient along y-axis, the x-y projection analysis is sufficient to calculate the tumble rate bias. In case of a tumble that purely occurs in x-z or y-z plane, the program may fail to detect it. However, such cases are considered to be rare events, and thus cause negligible effects to the statistical analysis of the tumble rate over swimming directions.

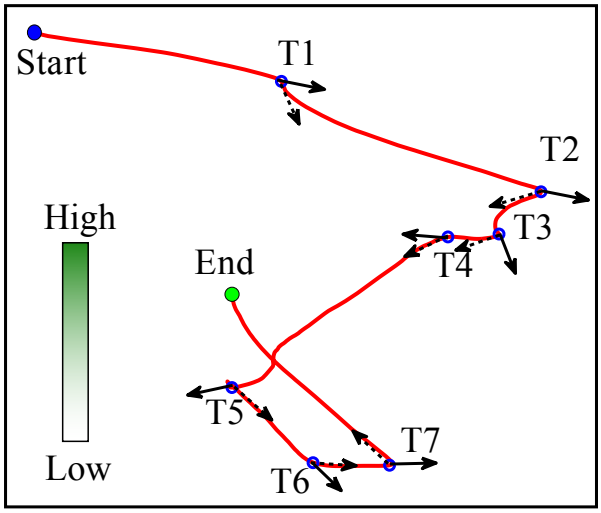

Figure 2.6: A sample trajectory with tumbles (T_i) detected by the tracking program, where the solid and dashed arrows stand for the swimming directions before and after the tumbles, respectively.

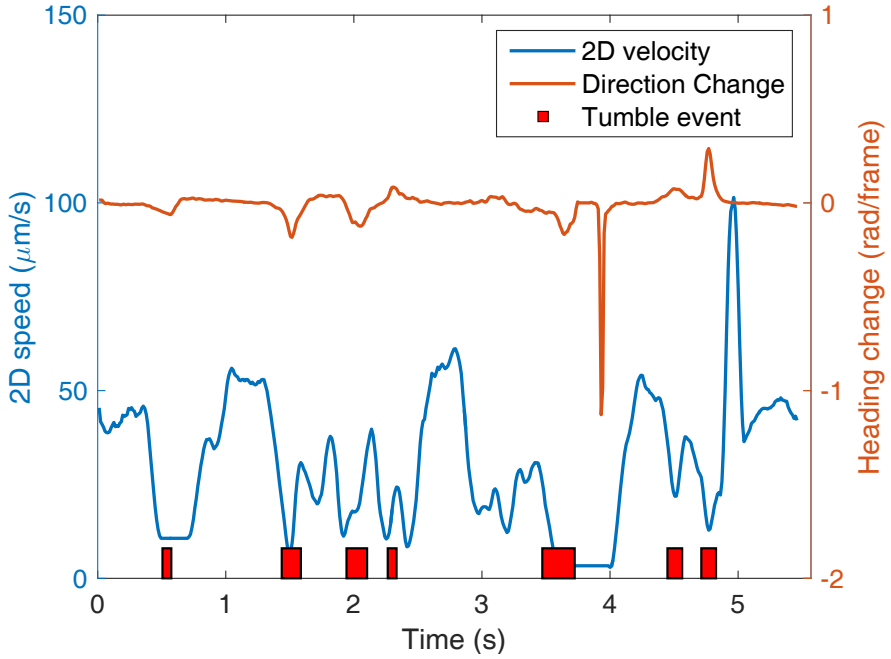

Figure 2.7: Swimming speed and heading change along a sample trajectory, as shown in Fig. 2.6, where seven tumble events were detected by applying a threshold to the heading change.

2.5 Framework Demonstration and Results

2.5.1 Materials and Experiment Settings

The chemotactic response of *S. marcescens* (see Appendix A for details) towards the concentration profile of L-aspartate was characterized as a demonstration of the framework. L-aspartate has been extensively used as a chemoattractant for *E. coli*, which exhibits the strongest chemotactic behavior at a concentration gradient around 0.1 mM/mm [71, 72, 74, 76]. We have determined experimentally that *S. marcescens* loses motility in L-aspartate solutions with concentrations higher than 10 mM. Therefore, we measure the chemotactic response of *S. marcescens* in a concentration gradient range of 10^{-3} mM/mm to 5 mM/mm, with 5×10^{-3} mM and 2.5 mM as the lowest and highest average concentration, respectively. All the concentrations of L-aspartate were obtained by suspending L-aspartate in the motility medium, therefore no gradient of other substances existed in the sample channel. The experiments were conducted at room tempera-

ture, around 20°C. To initialize the experiment, solutions with higher and lower concentrations of L-aspartate were flowed in the source and sink channels, respectively. Upon the infusion of solutions in the two side channels, we pipetted bacterial solution with appropriate density into the sample channel. Videos were taken after a linear concentration profile had been established in the sample channel.

2.5.2 Characterization Results

Parameters of full pathway model

We implement the full pathway model in a bacteria population simulator BNSim [100]. Based on the measurements at data points 1-7 in Fig. 2.11, the adaptation rates (k_R, k_B) and phosphorylation coefficient (β) are fit to 0.0033/s ($k_R = k_B$) and 5.8, respectively, by the least squared fitting method. We did not alter the values of other intrinsic parameters such as the dissociation constants since it is reasonable to assume that the Aspartate-Tar and CheYp-motor reactions of *S. marcescens* maintain similar kinematics to *E. coli* due to their high resemblance in other aspects. The values of major parameters in the full pathway model of *S. marcescens* in chemotaxis are presented in Table 5.1.

Table 2.1: Key parameters used in signaling pathway model simulation

Name	Description	Value	Source
N	Number of receptors in a receptor complex	6	[77, 85]
K_a	Dissociation constant of aspartate to active Tar receptor	3 mM	[101]
K_i	Dissociation constant of aspartate to inactive Tar receptor	18.2 μM	[101]
α	The free energy contribution coefficient	1.7	[77]
m_0	The free energy contribution coefficient	1	[77]
k_R	Receptor methylation rate	0.0033/s	This work
k_B	Receptor demethylation rate	0.0033/s	This work
β	Linear phosphorylation coefficient	5.8	This work

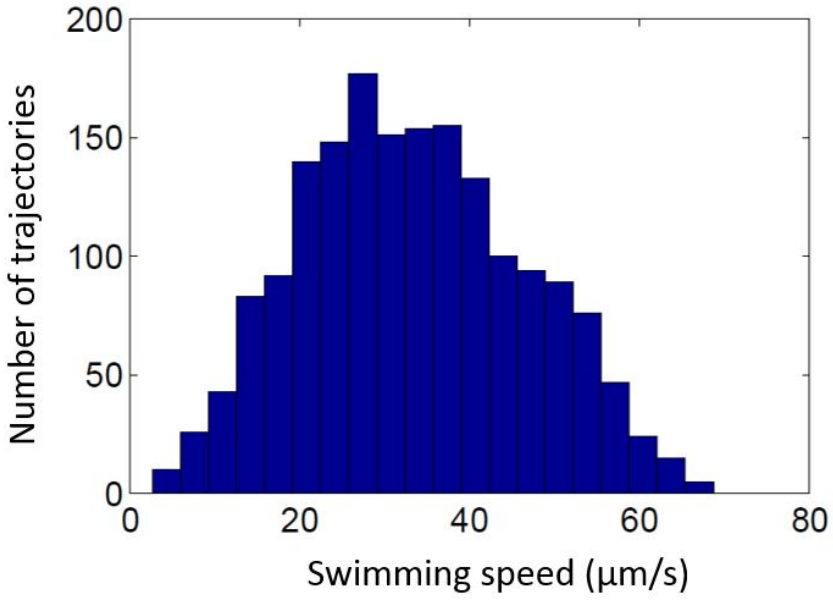

Figure 2.8: Bacterial speed (2D) distribution of a sample. The distribution was measured on all the bacterial trajectories tracked in the field of view (FOV) over the duration of the sample video.

Bacterial motility parameters

To determine the chemotactic velocity in Eq. 2.8, the parameters associated with the population of *S. marcescens* are needed, namely, the average swimming speed v, and the average tumble rates p^- and p^+. The average tumble angle ϕ is required to evaluate the motility coefficient μ via Eq. 2.9. All the parameters are measured from a population of 10,000 bacteria.

Swimming Speeds. Using the 3D tracking method, we measure the average swimming speeds of *S. marcescens* far away from walls in the agarose gel channel. The average 3D speed is 34 μm/s with an average speed of 30 μm/s in the x-y plane projection. The swimming speed of a measured sample generally follows a distribution close to normal distribution, as shown in Fig. 2.8, and the average swimming speeds are almost identical from sample to sample, with a variation smaller than 1 μm/s. The addition of L-aspartate gradient makes no significant difference to the swimming speed. We also observe the average swimming speed over elapsed time, but no obvious change is seen during a duration of four hours.

Tumble Angles. The tumble angle is also measured by 3D tracking. Our measurement of the mean tumble angle yields a similar distribution with that of *E. coli* with an average of 62 degrees [66]. The probability distributions of tumble angle with and without chemoattractant gradient are indistinguishable, which means that the L-aspartate gradient does not substantially change the tumble angle of *S. marcescens*.

Tumble Rates. Since the difference in the computed tumble rate between the 2D and 3D tracking was minimal ($< 5\%$) and the computational time was significantly less with the 2D tracking, the x-y plane (2D) projection of the trajectories was used to measure the tumble rate with respect to the swimming direction. The histograms in Fig. 2.9(a) and Fig. 2.9(b) show the tumble rates with respect to the swimming directions in the x-y plane, where the radius of each red segment indicates the average tumble rate when bacteria swim within that angle interval. We calculate the tumble rate for each angle interval through normalizing the cumulative number of tumble events occurring in an interval by the total time that bacteria swim in that interval.

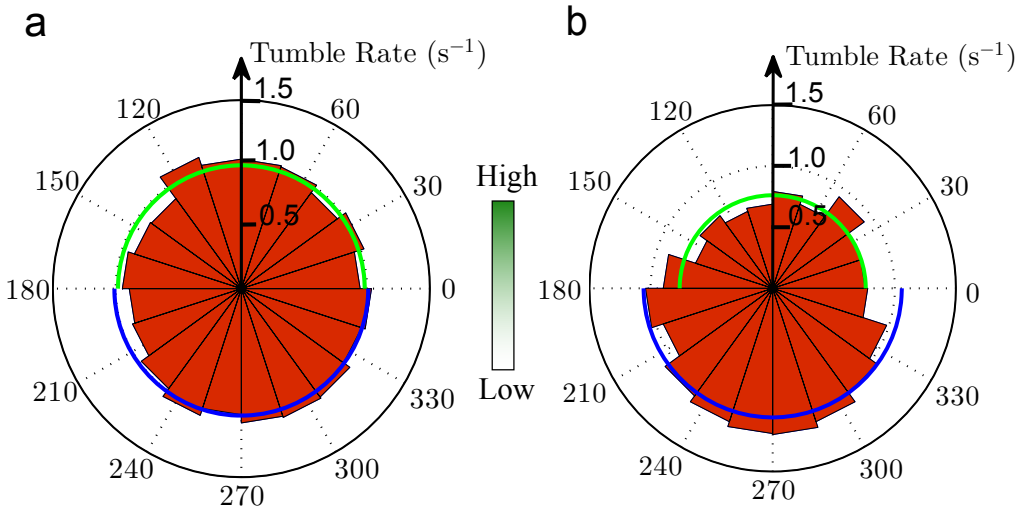

Figure 2.9: Comparison of bacterial tumble rate: (a) isotropic tumble rates over the swimming directions when there is no L-aspartate gradient in the channel, and (b) biased tumble rates when bacteria swim in an environment with a linear gradient of L-aspartate, which is 0.2 mM/mm for the case shown. In (a) and (b), the radii of the black (dashed) and blue (solid) semicircles indicate the average tumble rates when bacteria travel up and down the gradient, respectively.

For an environment without a chemoattractant gradient, in Fig. 2.9(a), the tumble rate is

same in all swimming directions, resulting an average tumble rate around 1.0 s^{-1}. However, under a concentration gradient, the tumble rate when bacteria swim up the gradient is substantially decreased, while no significant change is seen in the tumble rate when they swim down the gradient, as shown in Fig. 2.9(b). The average tumble rates when bacteria travel up and down the gradient are 0.75 s^{-1} and 1.05 s^{-1}, respectively. For a linear gradient of 0.2 mM/mm, the bias generates a drift velocity for bacteria towards higher concentration regions. Although bacteria experience a slightly different gradient according to the swimming direction, we neglect this difference and treat them identically. This approximation should not bias the results significantly since the difference in gradient from swimming direction is negligible given their wide sensing range in the ligand gradient.

Motility Coefficient. The motility coefficient quantifies the diffusivity of a population of bacteria when they are subjected to a random walk or a biased random walk. Based on Eq. 2.9, when there is no chemical gradient, an average tumble rate of 1.0 s^{-1} is used to calculate the motility coefficient, which gives a value for μ of 7.25×10^{-6} cm^2/s. For the case shown in Fig. 2.9(b), where the average of the tumble rate is 0.9 s^{-1}, the motility coefficient is calculated as 8.05×10^{-6} cm^2/s. A slightly higher diffusive motility is expected in the presence of a chemoattractant gradient since the average tumble rate of the population decreases. The motility coefficient does not vary significantly over different concentration gradients, as shown in Fig. 2.10. The motility coefficient for *E. coli* has been measured with different methods giving results varying from 1×10^{-7} cm^2/s to 7.2×10^{-5} cm^2/s [72, 102], but most reported values are on the order of 10^{-6} cm^2/s.

Chemotactic velocity

Data Distribution. The chemotactic velocity V_C is the primary index we use to study the response of *S. marcescens* to different gradients and average concentrations of L-aspartate. The value of V_C at each data point is calculated using Eq. 2.8 with the measured average tumble

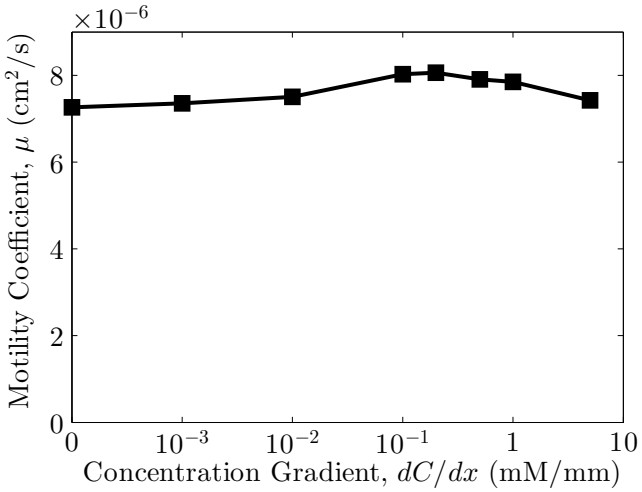

Figure 2.10: Dependence of the motility coefficient on the ligand concentration gradient.

rates up and down the gradients and the average swimming speed. A total of ten data points were measured as indicated in Fig. 2.11. The diagonal seven points are measured in a gradient generated by a non-zero concentration in the source and zero concentration in the sink, while the three off-diagonal points are created by inputing a higher concentration of L-aspartate in the source and a lower concentration of it in the sink.

For our gradient generator, there is an inequality between the average concentration and the concentration gradient: $\overline{C} \geq (l/2)dC/dx$, where $\overline{C}$ is the average concentration in the channel, dC/dx is the concentration gradient along the x-axis, and l is the diffusion distance (1 mm for our setup). Due to the physical constraint imposed by the inequality, we could not create data points in the gray region above the diagonal as shown in Fig. 2.11.

Chemotactic Response Curve. We measure V_C at points 1 through 7; the chemotactic velocity profile from the experiment and simulation is shown in Fig. 2.12. Since the average concentration is proportional to the concentration gradient, Fig. 2.12 also reveals the chemotactic response of *S. marcescens* against the average concentration. From the chemotactic response curve, a maximum chemotactic velocity is seen to occur at a gradient around 0.2 mM/mm with an average concentration of 0.1 mM. It can also be concluded that *S. marcescens* can respond to a wide range of chemoattractant gradients (average concentrations), as wide as three to four

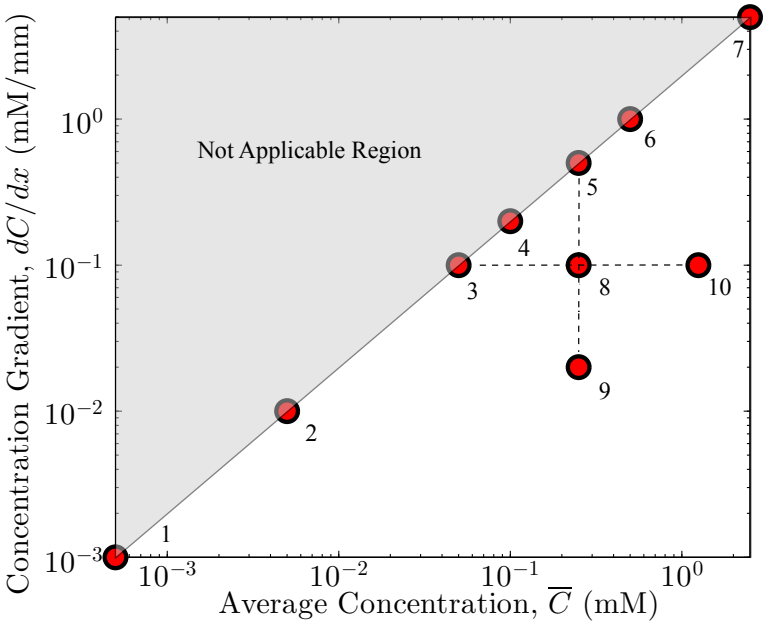

Figure 2.11: The distribution of experimental data points (circular markers). For data points 1-7, the gradient is generated by a known concentration of L-aspartate in the source and a zero concentration of it in the sink. For points 8, 9 and 10, the gradient is generated by a higher concentration of L-aspartate in the source and a lower concentration in the sink.

decades in concentration gradient (average concentration). Measurements based on the population density distribution of *E. coli* indicate a similar response trend, with a slight shift in the location of the peak [70, 77].

Relative Ligand Concentration Sensing. Chemotaxis behavior is not only dependent on the chemoattractant gradient, but it is also related to the local concentration [77]. Hence we measure the change in the chemotactic velocity with the gradient and the average concentration. Fig. 2.13(a) presents the change of V_C with respect to the concentration gradient, where the average concentration in the sample channel is kept constant at 0.25 mM (points 5, 8, and 9 in Fig. 2.11). It can be seen that the chemotactic velocity increases with an increase in the relative concentration gradient, denoted by $\frac{dC}{dx}\frac{1}{\overline{C}}$. We then fix the gradient (0.1 mM/mm), and measure V_C with an increasing average concentration (points 3, 8 and 10 in Fig. 2.11). As shown in Fig. 2.13(b), there is a consistent decrease in the chemotactic velocity with an decrease in $\frac{dC}{dx}\frac{1}{\overline{C}}$. Although the two trends are found from measurements at three data points, it should hold true for the

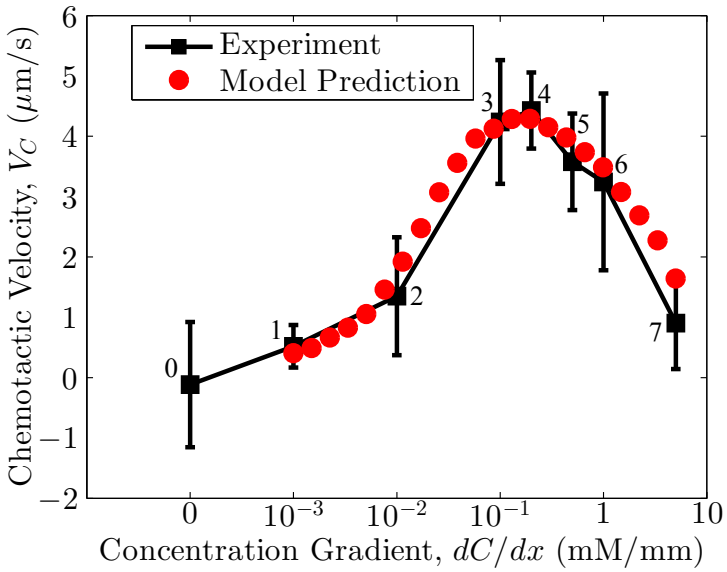

Figure 2.12: Chemotactic response curve. Plotted data for points 1-7 in Fig. 2.11 and a zero concentration gradient control experiment (data point 0). The strongest chemotactic response of *S. marcescens* occurs at a gradient around 0.2 mM/mm (0.1 mM in average concentration).

entire chemotaxis-response concentration domain due to the consistent inner regulating mechanism of chemotaxis. It can be concluded from the two figures that the chemotactic velocity increases monotonically with the value of $\frac{dC}{dx}\frac{1}{\overline{C}}$. The full pathway model with fitted parameters from Group 1 (points 1-7) is in agreement with the measurements from Group 2 (points 5, 8 and 9) and Group 3 (points 3, 8 and 10), as shown in Fig. 2.13. Measurements through the analysis of the density distribution of *E. coli* also show a similar sensing mechanism[77].

2.6 Discussion and Summary

2.6.1 Discussion

We have measured the chemotactic velocity and quantified the chemotactic response of *S. marcescens* to L-aspartate by the measured V_C. The accuracy of measured V_C for a population depends on the accuracy that we can obtain in the measurement of the tumble rates via Eq. 2.8. We applied an angle threshold (5 degrees) to detect tumbles from the swimming direction

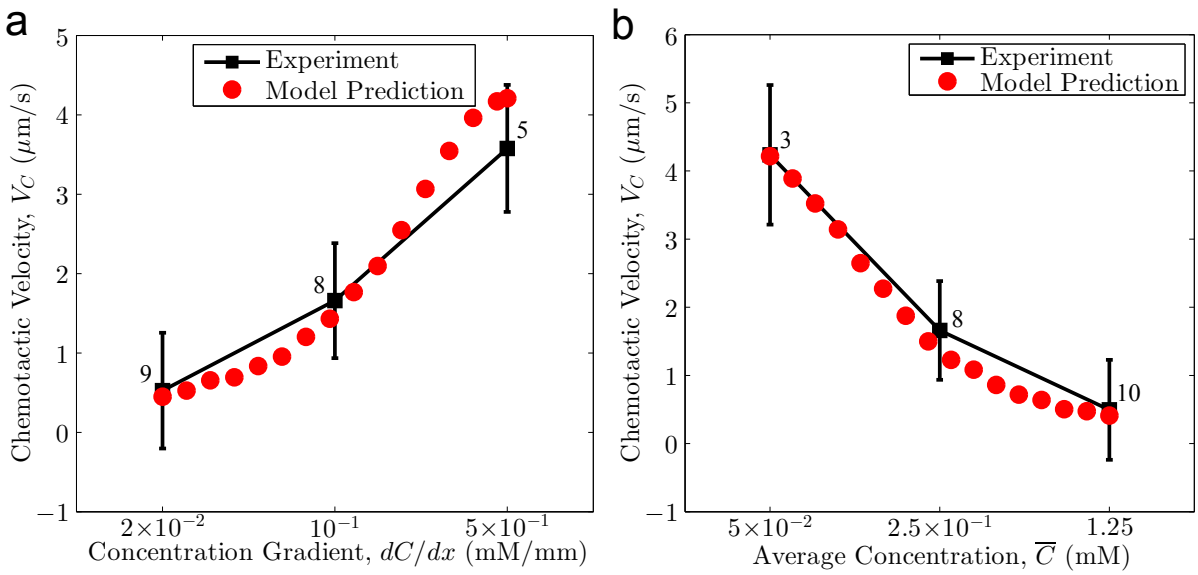

Figure 2.13: Relative gradient sensing measured from the experiment and captured by the simulation. (a) The chemotactic velocity increases with the gradient when the average concentration in the channel is kept as a constant of 0.25 mM. Experimental data points are the points 5, 8 and 9 in Fig. 2.11. (b) The chemotactic velocity decreases with average concentration when the gradient is kept as a constant value of 0.1 mM/mm. Experimental data points are the points 3, 8 and 10 in Fig. 2.11.

change in the 2D projection between frames. This could miss some tumbles and take direction change due to the bacterial collisions as tumbles. However, tumbles with angle changes smaller than 5 degrees can occur with a small probability, as verified from the 3D tracking of swimming bacteria [66].

By analyzing the mean free path of swimming bacteria, we can show that the swimming angle changes due to bacterial collisions are negligible . In particle mechanics, mean free path is evaluated by: $l = (n\sigma)^{-1}$, where l is the mean free path, n is the number of particles per volume, and σ is the effective cross sectional area. *S. marcescens* is a rod shaped bacterium with a diameter around 1 μm and length around 2 μm, leading to a cross sectional area smaller than 2 μm^2. The bacterial sample density is below 10^8 cm^{-3}, thus the mean free path is longer than 5 mm; since the swimming speed of the bacteria is around 34 μm/s, the mean free swimming duration is around 147 seconds, which is much longer than the the mean run duration of one second. Therefore the collisions (or apparent collisions) due to bacteria traveling over each other cannot induce considerable error in the measurement of the tumble rates.

We note that recent characterizations of chemotaxis in *E. coli* mainly rely on population density analysis and typically use the CMC to quantify the chemotactic response [69, 70, 74, 77]. CMC captures the extent of bias in the bacterial density distribution along the x direction and can be calculated by: CMC $= \sum (N_x(x - w/2))/(\sum N_x(w/2))$, where x is the bacteria position along the gradient direction, N_x is the number of bacteria in a small area that has a mean position of x, and w is the width of the sample channel. Although we used the chemotactic velocity to quantify the chemotactic response, the following analysis leads to a determination of the CMC from the measured V_C and μ in a bounded channel.

Considering an enclosed channel (assuming conservation of bacteria number), at steady state, we can find the bacterial density distribution profile from Eq. 2.7 by setting $J = 0$, then: $B(x) = B_0 e^{V_C x/\mu}$, where B_0 is bacteria density at $x = 0$. Thus, the model predicts an exponential density distribution of bacteria along the chemical gradient direction, which

is generally observed experimentally as a biased distribution of bacteria along the chemical gradient [70, 71, 76, 77]. The CMC can thus be integrated by substituting $B_0 e^{V_C x/\mu}$ for N_x in the previous formula, yielding CMC $= -[2e^{-V_C w/\mu}(-w/2-\mu/V_C)+2\mu/V_C-w]/[w(-e^{-V_C w/\mu}+1)]$. As a result, the CMC of *S. marcescens* can be calculated with the measured values of V_C and μ, as shown in Fig. 2.14. It can be seen that the V_C and CMC are nearly proportional to each other for a bounded channel, where the bacteria number is conserved.

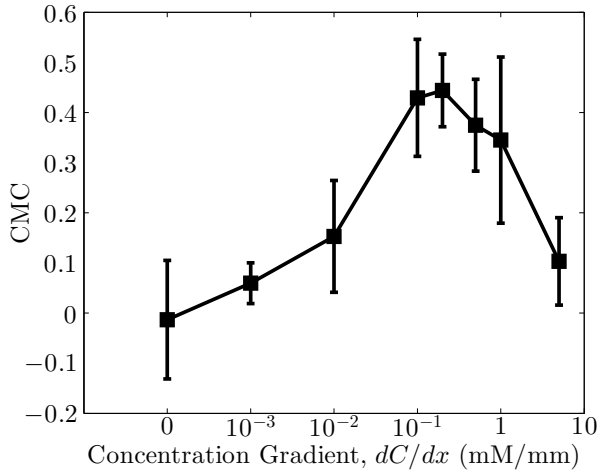

Figure 2.14: Chemotaxis migration coefficient (CMC) of *S. marcescens* over concentration gradient of L-aspartate. The maximum CMC corresponds to a concentration gradient of 0.2 mM/mm and an average concentration of 0.1 mM (L-aspartate).

The CMC curve of *S. marcescens* is similar to the studies on *E. coli* that measure CMC directly [70, 77]. Consequently, our characterization through individual bacterial analysis is consistent with the studies based on population density analysis. This also justifies that at low cell density, the population behavior in chemotaxis is indeed an aggregate rendering of individuals, and therefore the probabilistic modeling of individual bacteria in population transport is reliable.

In our results, the full pathway model is able to simulate the relative gradient sensing mechanism found in the chemotaxis of *S. marcescens*. Considering the concentration range we used in the characterization, we can perform a minimum interpretation of how the model treats the input of the ligand concentration profile and why the feature of the relative gradient sensing is

captured. In the full pathway model, Eq. 2.2 is in charge of the transduction of the the ligand concentration to a signal (the free energy difference F) for the inner pathway; when the bacteria travel in an environment with a one-dimensional gradient of chemoattractant, the rate of change of the free energy difference along the gradient $\partial F/\partial x$ ($\frac{\partial F}{\partial x} = \frac{\partial F}{\partial [L]}\frac{\mathrm{d}[L]}{\mathrm{d}x}$) is the signal that bacteria extract from the concentration profile. Notice that K_i is much smaller than K_a, then the differentiation can be approximated to $\frac{\partial F}{\partial x} = (\frac{-K_a[L]}{(K_a+[L])(K_i+[L])})(\frac{\mathrm{d}[L]}{\mathrm{d}x}\frac{1}{[L]})$. On the right hand side of this equation, $\frac{-K_a[L]}{(K_a+[L])(K_i+[L])}$ is a slowly changing term between 0.35 and 0.85 with $[L]$ varying from 0.01 to 5 mM. As a result, the sensed signal $\frac{\partial F}{\partial x}$ is dominated by the residual part: $\frac{\mathrm{d}[L]}{\mathrm{d}x}\frac{1}{[L]}$, which denotes the relative concentration gradient of the ligand. However, when $[L]$ is much higher than K_a, the sensed signal becomes proportional to $\frac{\mathrm{d}[L]}{\mathrm{d}x}\frac{1}{[L]^2}$, revealing a saturation kinetics at high ligand concentration in chemotaxis sensing. In practice, we use concentrations smaller or comparable with K_a, thus the model successfully traces out the relative gradient sensing trend as found in the experiments.

The calibrated setup and founded optimal concentration profile for *S. marcescens* can be used to perform a chemotactic steering control study of bacteria-driven micro-objects. *S. marcescens* generates a biased motion in a chemoattractant gradient by actively biasing its tumble rate according to the swimming direction, and the bias obtains a maximum at a gradient of 0.2 mM/mm (0.1 mM in $\overline{C}$) for L-aspartate. To realize directional control of bacteria propelled micro-objects, the minimum requirement is that the attached bacteria can generate a biased propulsion. It is reasonable to expect that the attached bacterial flagella still maintain the transition of rotational direction between CW and CCW, but do not necessarily form a bundle; the flagellum rotating in the CCW direction still generates a propulsive force to the beads but not for the flagellum rotating in the CW direction. Thus for a given micro-object with *S. marcescens* attached, on average, there should be more propulsive force exerted on the bead when the object moves up the chemoattractant gradient. Since the bacteria sensing machinery should be independent of their physical attachment, we expect that the concentration profile for

optimal control of *S. marcescens* propelled microbead should coincide with the concentration profile that yields the strongest chemotactic behavior. As will be shown in the next chapter, we observed prominent chemotaxis in bacteria-driven microbeads under the optimal concentration profile for the free-swimming bacteria.

2.6.2 Summary

This chapter presents an experimental and modeling framework to characterize the chemotaxis of free-swimming flagellated bacteria, such as *E. coli* and *S. marcescens*. The framework characterizes the chemotactic response of a species under a linear concentration gradient of a chemoattractant, which is generated and maintained in a flow-free microfluidic channel and thus eliminating any flow-induced effect on bacterial motion. The chemotactic response is quantified using chemotactic velocity (V_C), measured by tracking individual swimming bacteria and statistical trajectory analysis. This approach is not affected by the non-motile bacteria in a sample, which indeed causes measurement biases for the conventional methods based on density analysis. By fitting a signaling pathway model to the experimental measurements, the framework delivers an analytical description of the chemotaxis being characterized. This framework may also be readily adapted to study other bacteria taxis behaviors such as pH-taxis and salt-taxis. Chemotaxis of *S. marcescens* towards L-aspartate has been characterized using this framework. The chemotactic response was measured over a series of L-aspartate concentration gradients, ranging from 10^{-3} mM/mm to 5 mM/mm. It was found that the optimal concentration gradient of L-aspartate that leads to the strongest chemotactic behavior of *S. marcescens* is around 0.2 mM/mm. We have also verified the relative gradient sensing machinery in the chemotaxis of *S. marcescens*, by measuring the change of V_C with the average concentration and the gradient; about which, the adopted signaling pathway model with fitted parameters agrees with the experimental measurements. Our results suggest a high level resemblance between the chemotactic responses of *S. marcescens* and *E. coli*, which indicates that it is highly possible that the

two bacterial species share a similar biochemical regulating pathway for chemotaxis; this may in turn corroborate why the full pathway model for *E. coli* also applies well to describe the chemotaxis of *S. marcescens*. The chemotaxis characterization of *S. marcescens* brings new knowledge towards integrating the species for chemically-guidable biohybrid microrobots.

Chapter 3

Chemotaxis of Bacteria-Driven Microrobots

3.1 Introduction

As we discussed previously, flagellated bacteria, like *Serratia marcescens* (*S. marcescens*), is among the leading candidates for the actuators of self-propelled biohybrid microrobots, not only because of their ease of cultivation and high motility, but also due to their chemotactic behavior, which is a potentially elegant way to control bacteria-driven microrobots at the swarm level. Although several studies have observed chemotaxis of bacteria-driven microrobots [48, 49, 50, 51], none of them has quantified the associated chemotactic drifting motion and the importance of the microrobots' motility for their chemotaxis. Thus, the physical mechanisms of the collective chemotaxis among the multiple bacteria attached to a microrobot has been unclear to date. Despite the well established theory on bacterial chemotaxis [66, 67], it is not readily understandable how a bacteria-driven microrobot, consisting of a micro-structure propelled by multiple randomly attached bacteria, is endowed with chemotaxis. To shed light on this, notable chemotactic drift motion of bacteria-driven microrobots must be created and observed experimentally, and the motion should be characterized quantitatively to elucidate the

critical factors that drive their chemotaxis.

The major goal of this chapter is to investigate the chemotactic drift motion of bacteria-driven microrobots under a linear chemoattractant gradient, as illustrated in Fig. 3.1, in a fashion helpful to understand the associated chemotactic drift motion and meaningful to develop bacteria-driven microrobots with enhanced chemotactic behavior. To this end, we first introduce a prototype of bacteria-driven microrobots, including a brief introduction of its swimming dynamics and development procedures. Subsequently, relying on the three-channel microfluidic concentration gradient generator (see details in Appendix B), we characterize the chemotactic response of the free swimming bacteria *S. marcescens* to L-serine (chemoattractant), and an optimal concentration gradient that leads to the strongest chemotactic response is empirically determined. Using the optimal gradient, the chemotactic drifting process of the bacteria-driven microrobotic swarms are captured and quantified. By tracking the individual microrobots and statistically analyzing their swimming trajectories, we identify the critical factors and the physical mechanisms which enable the chemotaxis in the bacteria-driven microrobots. Finally, we present a dependency of the chemotaxis in the bacteria-driven microrobots on their swimming speed.

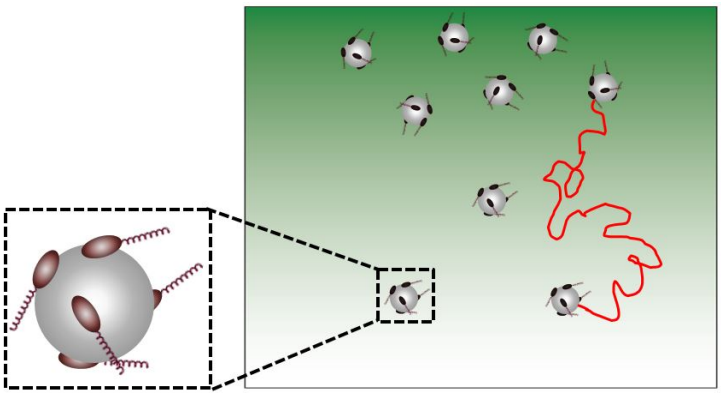

Figure 3.1: An illustration of the chemotactic guiding of bacteria-driven microrobots, where each microrobot is attached and propelled by a few chemotactic bacteria.

3.2 Bacteria-Driven Bio-Hybrid Microrobot

One of the advantages of utilizing bacteria as actuators of biohybrid microrobots is its scalability. The average density of bacterial attachment on a microrobot can be controlled by adjusting the bacterial density in the solution, attachment duration or other factors if more sophisticated attachment methods are being used. The most widely adopted design of bacteria-driven microrobots consists of a spherical structure with multiple bacteria attached in random locations and directions. Recent studies have tried to pattern the bacterial attachment [29, 50] and designing different body shapes [51, 103], aiming to enhance the performance of bacteria-driven microrobots, such as motility and directionality. In some special cases, such as in a cube-shaped design of bacteria-driven microrobots, an enhancement of the motility by selectional bacterial attachment has been reported [29]. However, since there is no effective way to align the orientation of the attached bacteria, the attachment patterning and shape optimization could not improve the motility or directionality of bacteria-driven microrobots in a considerable manner.

Without loss of generality, we adopted the mostly widely adopted design of bacteria-driven microrobots, which is a spherical body with a few bacteria attached randomly, to characterize the chemotaxis in such biohybrid systems. To the end of this section, it can be seen that the optimized designs, namely, attachment patterning and optimized shape, are expected to share the same mechanism of chemotaxis and may have enhanced chemotactic behavior.

3.2.1 Configuration and Propulsion Model

Fig. 3.2 shows a simplified depiction of bacteria randomly attached to a microsphere, where the bacterial flagella may not represent the reality, because they may not be bundled at low swimming speed or in tumble state. $\boldsymbol{F}$ and $\boldsymbol{T}$ are instantaneous net propulsive force and torque exerted on the sphere by all of the attached bacteria. As a result of the bacterial propulsion, there generates instantaneous translational velocity, $\boldsymbol{v}$, and angular velocity, $\boldsymbol{\omega}$, on the microrobot. Since bacteria-driven microrobots typically swim at the Reynolds number regime (Re $\approx 10^{-5}$),

any inertial effect can be neglected. For a spherical body, Stokes' law describes the viscous drag forces from the surrounding fluid when the microrobot swims through the fluid medium:

$$\begin{aligned} \boldsymbol{f} &= -6\pi\eta R\boldsymbol{v} \ , \\ \boldsymbol{\tau} &= -8\pi\eta R^3\boldsymbol{\omega} \ , \end{aligned} \tag{3.1}$$

where, $\boldsymbol{f}$ and $\boldsymbol{\tau}$ are translational and rotational drags, respectively, η is the dynamic dynamic viscosity of the liquid medium, and R is the radius of the spherical microrobot. Since there is no acceleration on the microrobot, the translation and rotational drags are balanced by the propulsive forces at every moment, namely,

$$\begin{aligned} \boldsymbol{F} &= -\boldsymbol{f} \ , \\ \boldsymbol{T} &= -\boldsymbol{\tau} \ . \end{aligned} \tag{3.2}$$

It should be noted that the propulsive vectors, $\boldsymbol{F}$ and $\boldsymbol{T}$, are usually not collinear due to the random configuration of bacteria on microrobots. This property is important for understanding the trajectory shape of bacteria-driven microrobot.

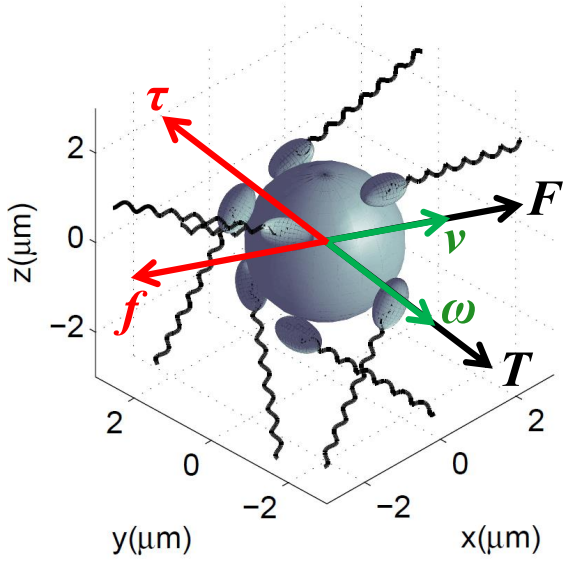

Figure 3.2: Free-body diagram of a swimming bacteria-driven microrobot, where $\boldsymbol{v}$ and $\boldsymbol{\omega}$ are instantaneous translational velocity and angular velocity of the microrobot.

3.2.2 Characteristics of Motion

Using the optical aberration ring of a defocused object under a phase contrast microscope, Edwards et al. were able to track the 3D motion of bacteria-driven microrobots. The studied microrobots were fabricated by randomly attaching bacteria to 5μm diameter polystyrene microbeads. For the microrobots swimming in the far-wall regime (Fig. 3.3(b)), they captured helical or approximately helical swimming trajectories in some microrobots, on each of which the attached bacteria exerted a nearly constant force and a nearly constant torque. In normal cases, the force and torque on a microrobot were not collinear, thus producing a helical trajectory on the microrobot. However, for the microrobots swimming in the near-wall regime, almost no trajectories were found to be helical or close to helical shape, as shown in Fig. 3.3(a). This difference suggests that the walls in close proximity of bacteria-driven microrobots can disturb the bacterial propulsion on microrobots and hence break their natural motions. Therefore, to avoid the wall effects on the chemotactic motion of bacteria-driven microrobots, we study the motion of bacteria-driven microrobots in the far-wall regime.

From 3.3(b), although durations of stable propulsion were manifested in some trajectories, frequent deviations from helical motions did show along the trajectory. Moreover, a substantial portion of the trajectories were more of random walks, indicating that the forces and torques applied on the corresponding microrobots changes constantly. The stochasticity in the motion of the bacteria-driven microrobots increased with the average number of bacteria attached to the microrobots. Over long durations, the motion of the bacteria-driven microrobot could be characterized as a random walk.

3.2.3 Prototyping Bacteria-driven Microrobots

The bacteria-driven microrobots used in our study were fabricated by randomly attaching bacteria to 3μm diameter fluorescent polystyrene beads (ρ = 1.05 g/cm^3, Fisher Scientific, Inc.). To enable natural attachment between the bacteria and beads, the original coating of the beads was

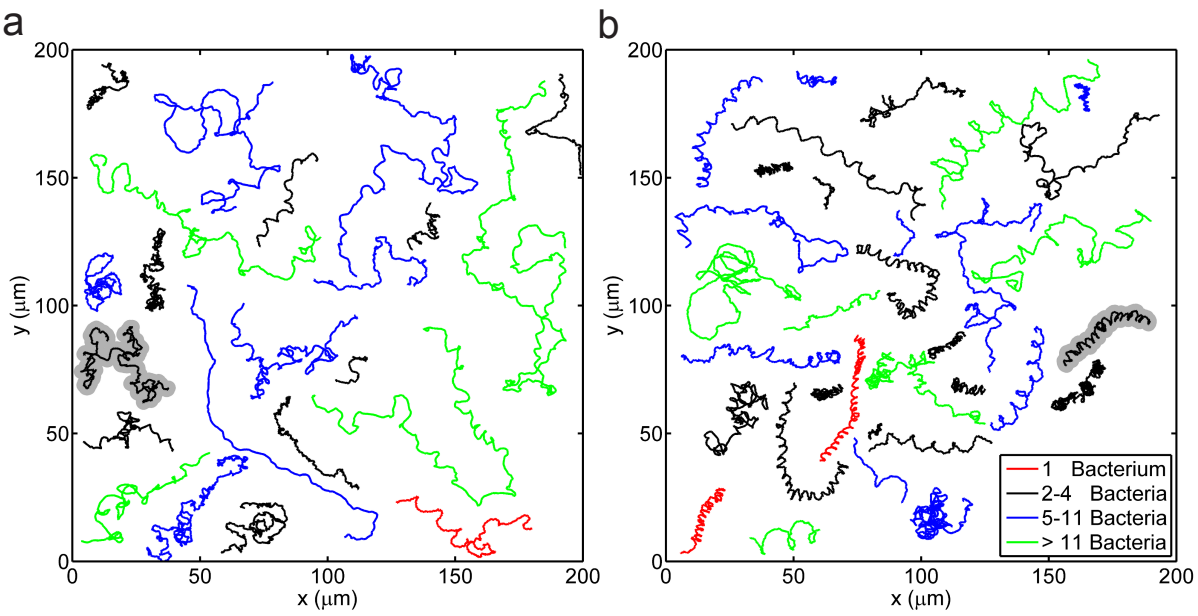

Figure 3.3: (a) Near- and (b) far-wall 2D swimming trajectories of a prototype of bacteria-driven microrobots (figure reprinted from [34]).

removed by alternately ultrasonicating the beads in deionized (DI) water or isopropyl alcohol (IPA, 50%) for a total of five cycles; residual IPA in the bead solution was removed by three more ultrasonication cycles with DI water. The washed beads were soaked in motility buffer at a volume concentration of 0.05%. The microrobots were assembled by placing an aliquot of 2.5 μL bead solution onto the leading edge of the bacteria colony on the agar plate and gently pipetting 3 - 5 times to mix the bacteria and beads sufficiently. The solution was collected back immediately and incubated at room temperature for 5 minutes, allowing for random attachment of the bacteria to the beads. Then, the solution was diluted by adding 40 μL of Percoll (ρ =1.13 g/cm^3, Sigma-Aldrich, St. Louis, MO) and 57.5 μL of motility buffer to the solution. Percoll was added to increase the density of the fluid, thereby making the microrobots neutrally buoyant. The final solution was further diluted to achieve an appropriate concentration for vision tracking of the microrobots.

Fluorescent staining of bacteria enabled the simultaneous visualization of the attached bacteria and bead (Fig. 3.4). The mean and standard deviation of the number of assembled bacteria

to each microrobot were determined to be 9.0 $\pm$ 3.4, based on an examination of 20 instances randomly picked from the whole population.

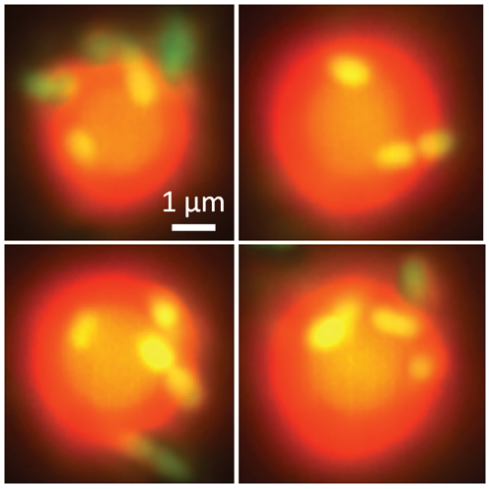

Figure 3.4: Fluorescent images of the prototype of bacteria-driven microrobots, which are composed of multiple attached bacteria (yellow-green) and a spherical polystyrene bead (red).

3.3 Chemotactic Response of *S. marcescens* to L-serine

According to the fabrication procedure, the position and orientation of the attached bacteria on the microbeads were purely random, resulting in high stochasticity in the configuration of bacteria on the microrobots (Fig. 3.4). To achieve considerable chemotactic drift in such a stochastic system, we first characterized the chemotactic response of the bio-actuator alone, *S. marcescens*, towards the chemoattractant L-serine. This step served to find the optimum concentration profile, which could elicit the strongest bacterial chemotactic response, to be used for the study of the chemotaxis in the prototyped bacteria-driven microrobots.

L-serine is a canonical and potent chemoattractant for bacteria like *E. coli* and *Salmonella typhimurium* [32, 66, 72, 77, 104, 105, 106], and has shown to be mainly sensed by the abundant transmembrane receptor *Tsr* [107, 108, 109]. *S. marcescens*, a species that highly resembles *E. coli* in terms of motility and taxis behaviors [55], is believed to exhibit remarkable chemotaxis to L-serine as well. It has been established that flagellated bacteria, such as *S. marcescens* and

E. coli, swim through a combination of runs and tumbles, which are responsible for translation and random reorientation of the bacteria, respectively. In an environment with a chemoattractant gradient, bacteria decrease their tumble rate when they move towards a favorable direction while maintaining at a normal state (i.e. normal tumble rate) when moving towards the unfavorable direction. Such a biased tumble rate on individuals produces a population level drift up the concentration gradient of the chemoattractant, which is described by the *chemotactic velocity*, V_C [68, 72], as follows

$$V_C = \frac{8v_{2D}}{3\pi}\frac{r^- - r^+}{r^- + r^+}\,. \tag{3.3}$$

where, r^+ and r^- are the mean tumble rates when bacteria travel up and down the chemical gradient, respectively, v_{2D} is the two-dimensional (2D) mean swimming speed of bacteria. Compared with Eq. 2.8, this equation evaluates the chemotactic drift velocity by using 2D data of bacterial swimming motion. Here, in the three channel concentration gradient generator (see details in Chapter 2 and Appendix B.), we tested the the chemotaxis of *S. marcescens* under a series of linear concentration profiles of L-serine, and quantified the chemotactic response using V_C, which can be readily determined from the 2D trajectories of the swimming bacteria [54]. For each concentration gradient, the chemotactic velocity, V_C, was measured over five independent video samples which were taken from different locations in the sample channel (far away from any walls to avoid any wall effects). Two-dimensional (2D, xy-dimension) swimming trajectories of bacteria under chemotaxis was extracted and analyzed with similar methods as introduced in our previous studies [54, 55]. The number of swimming trajectories captured in each video varied from 500 to 3000. As shown in Fig. 3.5, the chemotactic velocity peaks around a concentration gradient of 10^{-4} M/mm, which is of the same order of magnitude of that of *E. coli* [77]; moreover, the chemotactic response trend is similar to that of *E. coli*, which suggests a resemblance in the signaling pathway dynamics for L-serine chemotaxis between these two bacterial species.

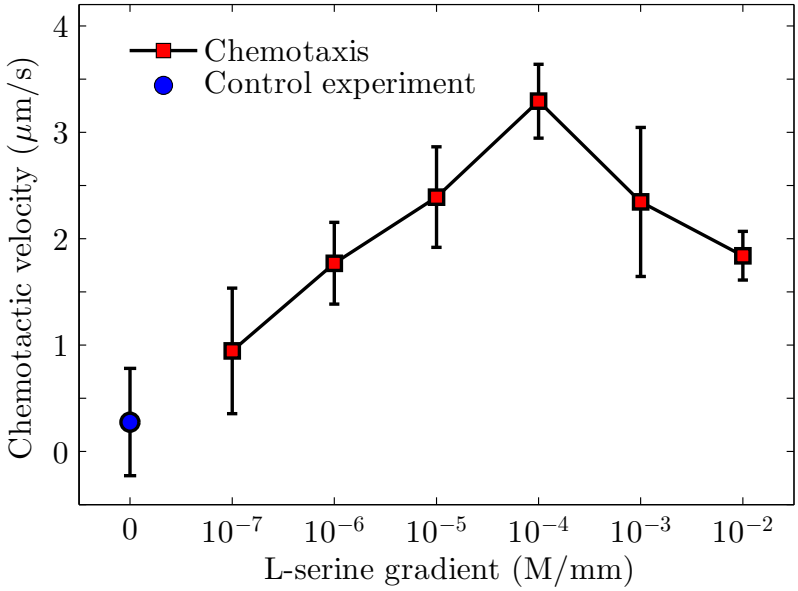

Figure 3.5: Chemotactic response of *S. marcescens* to linear concentration gradient of L-serine. At the data points of chemotaxis (red squares), the corresponding L-serine gradients were created by a nonzero concentration in the source channel and a zero concentration (buffer flow) in the sink; the gradient of control (blue circle) was zero, enabled by simply inputing both source and sink with a buffer flow.

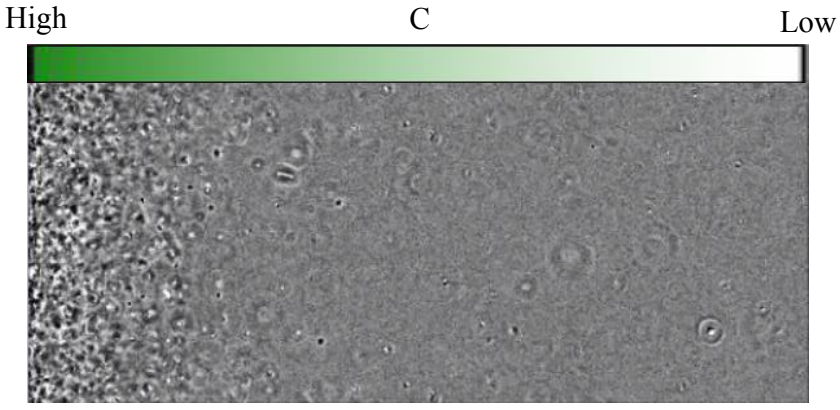

Figure 3.6: Bacterial distribution in the sample channel under the optimum concentration profile.

3.4 Chemotactic Drift of Microrobotic Swarms

3.4.1 Experimental Setup and Conditions

After finding the optimal concentration profile for the free swimming bacteria, we characterized the chemotaxis of bacteria-driven microrobots under the optimal concentration profile, which is 10^{-4} M/mm. We used the same design of the three-channel microfluidic device, but the height of the channels was increased to 200 μm to eliminate wall effects. Moreover, the sample channel were fully closed upon the loading of the sample to avoid undesired pressure driven flows. Therefore, in the sample channel of the microfluidic concentration gradient generation device (Fig. 3.7(a)), we created a quiescent fluid environment with a spatial concentration gradient of L-serine to characterize the chemotaxis of the prototyped bacteria-driven microrobots. Fig. 3.7(b) shows a fluorescent image of the biased distribution of the microrobots in the sample channel, where the entire width of the channel is fully captured in the image. The bright dots in the field indicate individual microrobots and the bigger bright areas closer to the source channel correspond to clusters of microrobots which were accumulated as a result of chemotactic drift. A sample microrobot is shown in Fig. 3.7. All the experiment were conducted in room temperature, around 20°C.

3.4.2 Drifting Process

The chemotactic drifting process was observed on five independent samples of bacteria-driven microrobotic swarms. Each sample started with a uniform distribution of microrobots in the sample channel. The drifting process of one of the samples is shown in Fig. 3.8. It can be seen that the initial uniform distribution of the microrobotic swarm in the sample channel evolved gradually into a highly biased distribution: the side with a higher concentration of L-serine was associated with a remarkably higher density of microrobots than the other side. This indicates that the bacteria-driven microrobots preserve the chemotactic behavior observed in the free

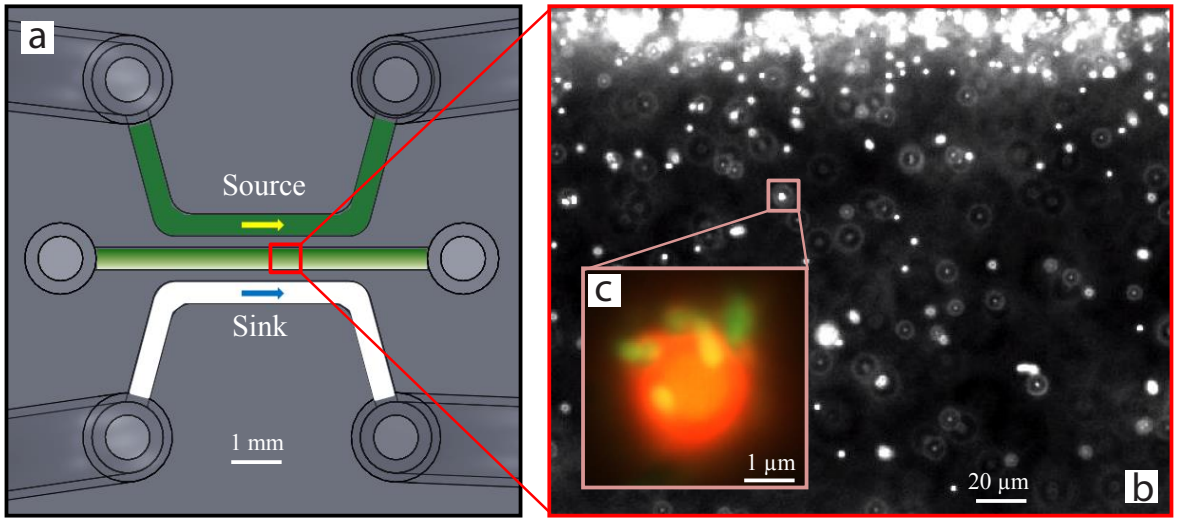

Figure 3.7: (a) *Top view* of the three parallel microfluidic channels. (b) Fluorescent image of a swarm of microrobots, where the topside corresponds to higher concentration of L-serine. (c) Fluorescent image of a sample microrobot.

swimming bacteria of *S. marcescens*.

To quantify the chemotactic drift of the bacteria-driven microrobots, we examined the center of mass (COM) position of the microrobots captured in each imaging frame and plotted its y component (COM-y) over time (Fig. 3.9). The COM-y of a frame can be calculated by: COM-$y = \frac{1}{n}\sum_{i=1}^{n} y_i$, where y_i is the y-position of the i-th microrobot, and n is the number of the captured microrobots in the frame. As can be seen in Fig. 3.9, the initial drift process (up to 7.5 min) traces out a linearly increasing COM-y over time, which suggests an approximately constant chemotactic drift velocity of the swarm. After the linear region, the distribution tends to stabilize to a *final state*. We observed that the microrobots gradually drifted to the higher concentration side of the sample channel and then formed clusters, whereas those scattered in the channel were non-motile, typically without attached bacteria. The clusters initially appeared because the motion of the microrobots were constrained by the walls of the sample channel. Since both groups, the clusters and the scattered individuals, had rather low motilities, the system reached a relatively stable final state.

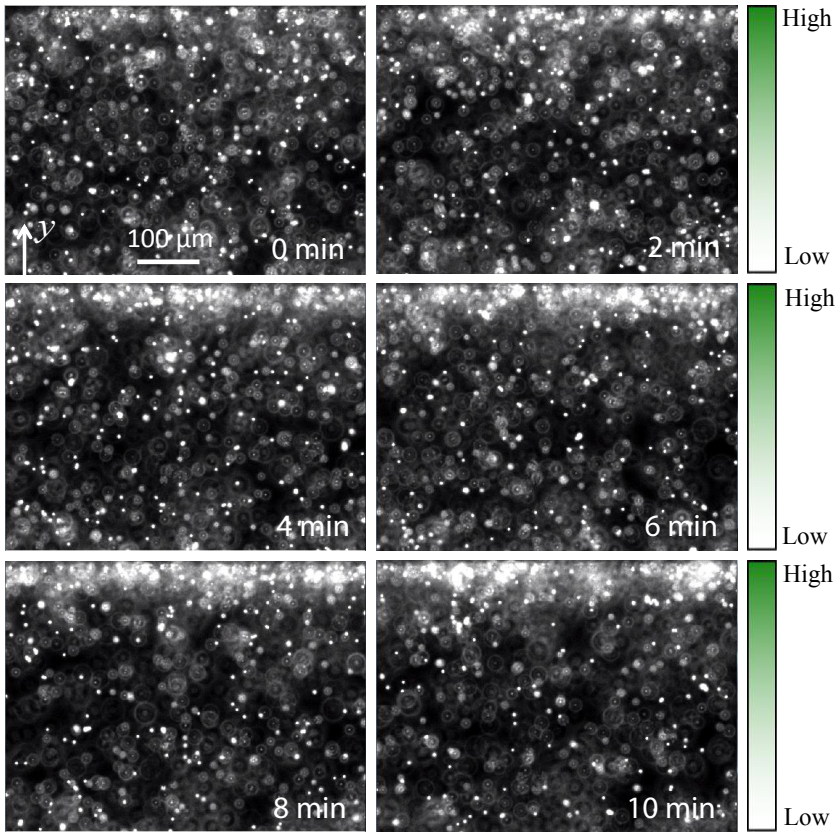

Figure 3.8: Fluorescent images show the distribution of a swarm of bacteria-driven microrobots at a fixed location in the sample channel over time, of which the starting point is when the diffusion of the chemoattractant starts, i.e., when the flow is initiated in the source and sink channels. As indicated by the gradient color bars, the chemoattractant gradient is aligned with the y-dimension of the images along the width of the sample channel. The initial two minutes were not recorded in order to allow for disturbance-induced flows to settle down.

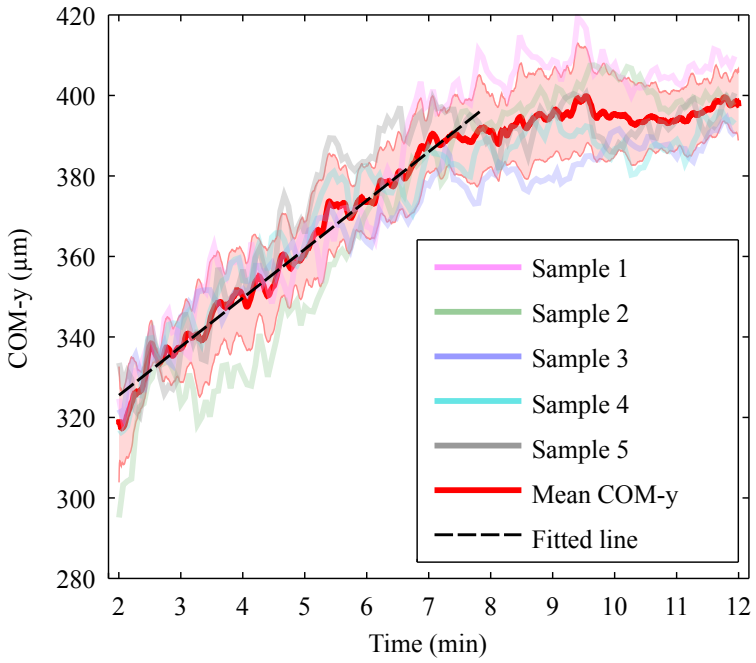

Figure 3.9: COM-y of bacteria-driven microrobot swarm over time. For each of the five samples, 3,000 image frames were captured over 10 min and the COM-y of each frame is plotted. The red curve and the shaded area indicate the mean and standard deviation found among the five samples.

3.4.3 Probability Distribution at Final State

Fig. 3.10 presents the probability distributions of the y-position of the bacteria-driven microrobots for both the chemotactic samples at final state and the control samples at steady state. The chemotactic sample manifest a significant bias in the distribution: most of the microrobots located within 100 μm from the source-side channel wall. However, the control sample (without L-serine gradient) trace out a more uniform distribution with a slight higher density at the near-wall regions, because the walls confined the motions of the microrobots close to the walls. By the comparison between these two distributions, it can be concluded that the unidirectional drift of the bacteria-driven microrobots under the L-serine gradient was due to chemotaxis rather than other factors, such as wall effects.

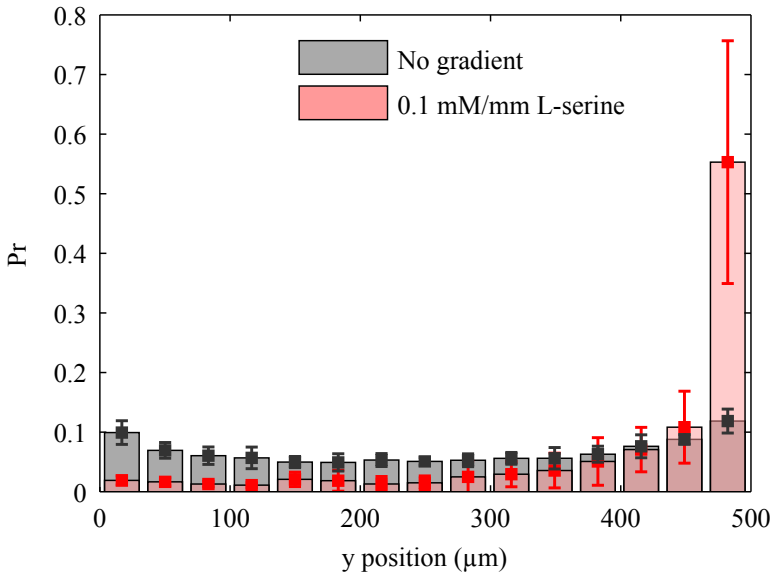

Figure 3.10: Probability distribution of microrobots across the width of the sample channel at final state. The means and standard errors of the chemotaxis group (0.1 mM/mm gradient) were evaluated on five different samples while the control group (no gradient) was based on three independent samples.

3.5 Visual Tracking and Trajectory Analysis

3.5.1 2D Tracking of Microrobots

The microfluidic device was placed under an inverted microscope (Axio Observer 100, Carl Zeiss, Oberkochen, Germany), and the samples were imaged with either a 10x (fluorescence imaging of microrobots) or 40x (phase contrast imaging of bacteria) objective. Videos of microrobots were captured at frames rates of 5 fps (QICAM, 520 $\times$ 696 pixels, QImaging). A custom visual tracking program developed in MATLAB (R2012a, The MathWorks, Inc, Natick, MA) was used to capture the moving trajectories (2D, xy-dimension) of microrobots. Image intensity thresholding was applied to detect the likable bodies of microrobots in a video frame, the bodies belonged to the same microrobot in consecutive frames were linked by a moving search from every frame to their own adjacent next one. The basic algorithms used for the visual tracking is included in Appendix C, Algorithm 1 and Algorithm 2. The motion of microrobots was recorded far from (≥ 10 body lengths) any walls of the sample channel to eliminate wall effects.

3.5.2 Trajectory Analysis

Drift analysis based on swarm distributions hides the important information about the physical mechanism that enables the chemotactic motion of the individual microrobots. In addition, calculating the chemotactic velociy from the COM-y leads to an underestimated value due to the restricted motion of the microrobots near the channel walls and the biased contribution from the non-motile microrobots. In light of these limitations, we tracked the swimming trajectories of the microrobots and performed statistical analysis on them, aiming to unveil the physical mechanism that allows the chemotaxis of the individual microrobots, which produces the swarm-level chemotactic drift. For each sample presented in Fig. 3.8, hundreds of trajectories were captured from the recorded video of drift motion, and Fig. 3.11 shows some randomly picked tracks of a

sample.

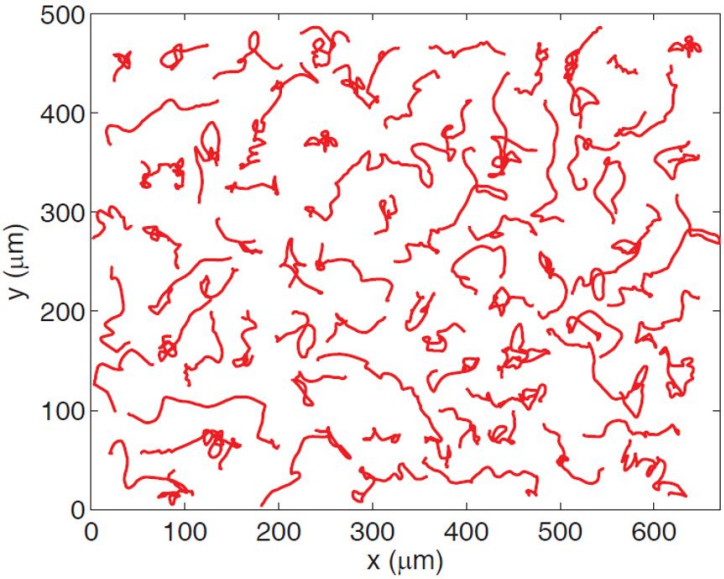

Figure 3.11: Sample swimming trajectories of bacteria-driven microrobots.

In the microfluidic device, the bacteria-driven microrobots were only subject to chemotactic stimulus along one dimension, namely along the y-axis; thus, the x- and z-components of the motion should be independent of the direction of the respective axis. In other words, their motion was only biased along the y-axis, and hence a 1D model is sufficient to capture the chemotaxis in the bacteria-driven microrobots.

Drift velocity of a 1D biased random walk

A particle that conducts random walk along one direction, namely the y-axis, is considered to determine the factors that can contribute to the drift velocity of a system exhibiting an inherent biased random walk. Assuming that the particle maintains different mean speeds when moving towards $+y$ and $-y$ directions, denoted by v_{+y} and v_{-y}, respectively; the particle can switch its direction of motion in a way such that the portion of time it spends moving towards the $+y$ direction, t_{+y}, is different from the time it spends moving towards the $-y$ direction, t_{-y}. It is straightforward to describe the 1D mean speed $\overline{v}_{1D}$ and the drift velocity V_{drift} (with $+y$ be the

default direction) of the particle,

$$\overline{v}_{1D} = \frac{v_{+y}t_{+y} + v_{-y}t_{-y}}{t_{+y} + t_{-y}} \, , \tag{3.4}$$

$$V_{drift} = \frac{v_{+y}t_{+y} - v_{-y}t_{-y}}{t_{+y} + t_{-y}} \, . \tag{3.5}$$

In Eq. 3.5, the drift velocity is essentially caused by the bias in swimming speed and the bias in the time spent in moving in a given direction. To include the two biasing factors, we define two ratios: the the speed ratio, $\alpha = v_{-y}/v_{+y}$, which is the ratio of the mean speeds in the $-y$ and $+y$ directions, and the heading ratio, $\beta = t_{-y}/t_{+y}$, which is the ratio of the time spent moving towards $-y$ and $+y$ directions. Substituting these coefficients into the two above equations, V_{drift} can be expressed in terms of the 1D mean speed $\overline{v}_{1D}$,

$$V_{drift} = \frac{1 - \alpha\beta}{1 + \alpha\beta} \, \overline{v}_{1D} \, . \tag{3.6}$$

Trajectory decomposition

The 2D swimming trace of a microrobot can be decomposed into segments persistently heading towards $+y$ (heading up) and segments persistently heading towards $-y$ (heading down) based on the y-component of its instantaneous heading direction, as illustrated in Fig. 3.12. Therefore, under the L-serine gradient, the motion of bacteria-driven microrobots along the y-axis is identical to a 1D biased random walk, and we can easily conform the trajectory analysis to the above model.

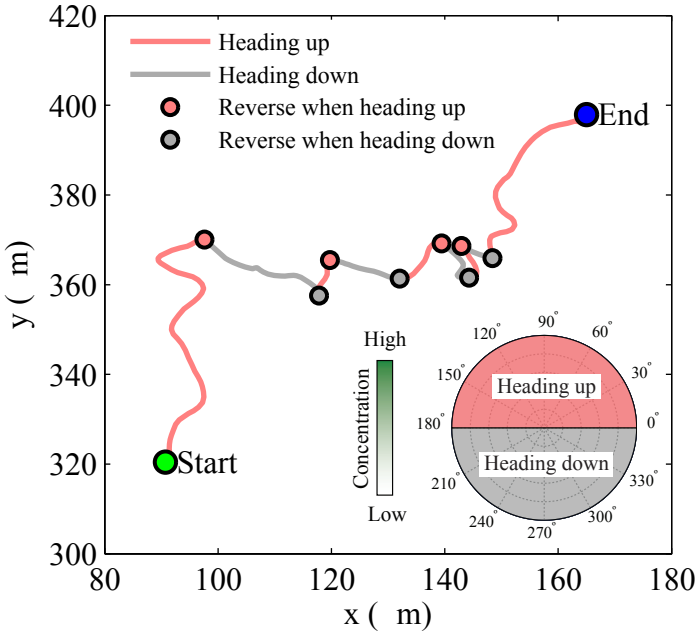

Figure 3.12: A sample trajectory is decomposed into two kinds of segments: the heading-up, during which the microrobot persistently moves up ($+y$) the L-serine gradient, and the heading-down, during which the microrobot persistently moves down ($-y$) the gradient. Correspondingly, along the trajectory, there are two types of direction reversing along the y-axis: reverse when heading up ($+y \rightarrow -y$) and reverse when heading down ($-y \rightarrow +y$).

3.6 Physical Mechanisms of Chemotaxis in Microrobots

3.6.1 Heading and Speed Biases

As revealed in Eq. 3.6, two factors could contribute to the drifting velocity, the heading bias and the speed bias. We quantified both of them by statistical analysis on the swimming trajectories of the microrobots in the five different samples.

Fig. 3.13(a) shows the time spent moving along each direction of the y-axis, represented by the number of frames counted in each direction. Across five independent samples, the portion of time spent moving up the L-serine gradient is considerably higher than that spent traveling down the gradient, which we call a "heading bias". This suggests that the bacteria-driven microrobots under the L-serine gradient exhibit a strong heading preference for moving up the gradient. Another factor that contributes to the 1D drift velocity is the speed difference, revealed by the speed ratio, α in Eq. 3.5. As shown in Fig. 3.13(b), a measurable mean speed difference exists between the components of motion heading up and heading down, which we refer to as the "speed bias". Though the speed bias is not as significant as the heading bias, the heading-up component has a higher mean speed, and the trend is consistent over all the samples. Since the translational speed is linearly related to the net propulsive force in the Stokes flow regime, the attached bacteria exert a slightly larger force when a microrobot moves up the L-serine gradient; presumably, the propulsive force is biased due to a lower probability of flagellar clockwise rotation (CW, corresponds to the tumble state of bacteria, and flagellar counterclockwise rotation, CCW, corresponds to the running state) in the attached bacteria when a microrobot swims up the gradient. The analysis based on swimming traces of the motile microrobots which were free from wall effects yielded a chemotactic drift velocity of 39.6 ± 12.9 μm/min, to which the heading bias contributes nearly five times more than the speed bias does based on the relative significance of the heading ratio and the speed ratio. Thus, the heading bias is the dominant driving factor of the chemotactic motion in the bacteria-driven microrobots.

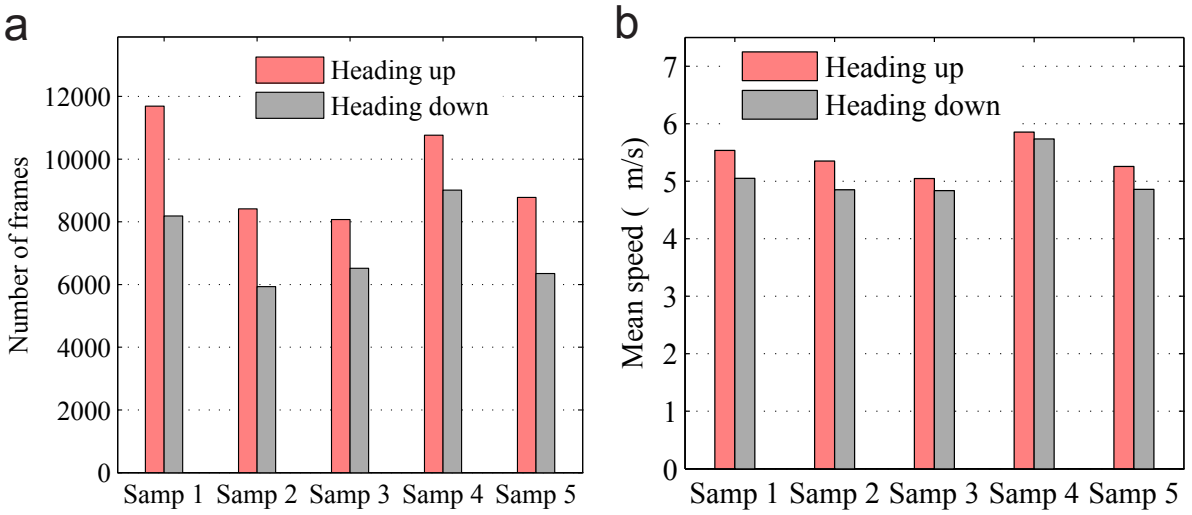

Figure 3.13: (a) Across all trajectories captured in each sample, number of frames (corresponding to time duration) counted for the heading-up and heading-down segments. (b) The mean speeds of the heading-up segments and the heading-down segments extracted from all trajectories captured in each sample.

3.6.2 Direction Reversing Rate Bias

To understand how the heading bias was generated in the bacteria-driven microrobots, we further inspected the relationship between the y-direction reversing rate and the heading direction. As illustrated by Fig. 3.13(a), the y-direction reversing events along a sample swimming trace were classified into two types; reverses associated with the heading-up segments ($+y \rightarrow -y$), and reverses associated with the heading-down segments ($-y \rightarrow +y$). The heading-up reversing rate is defined as the total number of direction reverses occurring while moving up the gradient divided by the total length of time traveling in the upward direction, and vice versa for the heading-down reversing rate. Fig. 3.14 shows the heading-up and heading-down reversing rates of each sample; the reversing rates when heading up are unanimously lower than those of heading down across the five samples. This concludes that, compared to moving down the gradient, the microrobots showed higher persistence in their y-direction heading when moving up the L-serine gradient. Given that the attachment between bacteria and the microbeads is merely

a physical adhesion [55], the signaling transduction pathway of the bacteria should not be distorted; therefore, the probability of flagellar CW rotation of the attached bacteria is expected to be higher when the microrobot which carries them moves down the gradient. The biased reversing rate of the bacteria-driven microrobots leads to the conjecture that the CW rotations of the flagella associated with the bacteria attached to a microrobot do increase the reorientation probability of the microrobot, which leads to the heading bias towards the up-gradient direction.

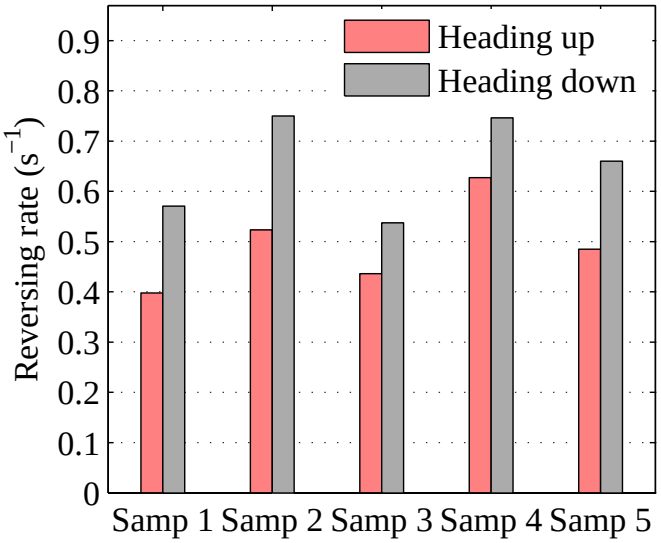

Figure 3.14: The direction reversing rates computed for the heading-up segments and the heading-down segments based on all the trajectories in each sample. More than 250 trajectories were captured for each of the five independent samples.

3.6.3 Effect of Speed on Chemotaxis

When described in 2D, as shown in Eq. 2.8, the chemotactic velocity is linearly dependent on the relative reversing rate bias, which can be described by $(r^{-y} - r^{+y})/(r^{-y} + r^{-y})$, where r^{+y} and r^{-y} are the reversing rates of the heading up and heading down cases, respectively. Fig. 3.15 plots the relative reversing rate bias with respect to the mean speed of the trajectories, where the relative reversing rate bias grows in a superlinear fashion, although it was shown earlier that the speed bias does not contribute significantly to the drift velocity. It can be concluded that the

mean speed influences the chemotactic velocity not only through being a scale factor of V_C as shown in Eq. 3.3, but also by affecting the relative reversing rate bias. Overall, the dependence of the chemotactic velocity on the mean swimming speed should be superquadratic. Since bacteria sense a spatial gradient in the form of temporal gradients as they swim through their environment, a higher translational speed usually produces a larger temporal gradient and thus, leads to improved bacterial sensing of the spatial chemical gradient.

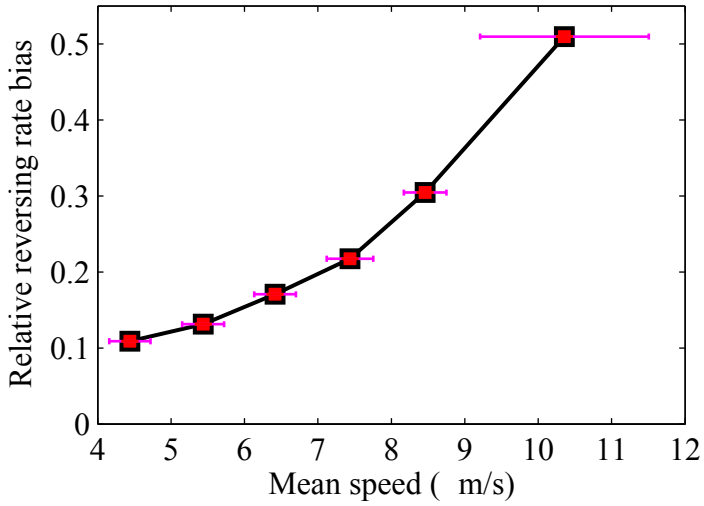

Figure 3.15: Dependence of relative reversing rate bias on mean speed. Trajectories from all five measured samples are classified into six speed intervals (4 - 5, 5 - 6, 6 - 7, 7 - 8, 8 - 9 and $\geq$ 9 μm/s) according to their mean speeds. The horizontal data points denote the mean speeds of the trajectories that fall within each range, with the error bars indicating the standard deviations of the means.

3.7 Discussion and Summary

3.7.1 Discussion

Chemotaxis is a rather common and understood behavior of flagellated bacteria, such as *S. marcescens* and *E. coli*; it is crucial for bacteria survival because chemotaxis navigates them towards nutrient sources or away from hazardous environments. Interestingly, recent studies

[48, 49, 50, 51] have observed chemotactic phenomenon in a microrobotic system driven by multiple bacteria, which implies a collective chemotactic behavior of the group of bacteria attached to a microrobot. By statistical analysis on the swimming trajectories of the prototyped bacteria-driven microrobots, for the first time this study elucidates the basic physical mechanisms which drive the seemingly cooperative chemotaxis among multiple bacteria attached to a common microstructure. Such chemotactic capability may prove to be beneficial for bacterial survival under certain conditions, such as when multiple bacteria are interlocked with each other, given that bacterial adhesion is ubiquitous in nature.

S. marcescens bacteria swim by a combination of runs and tumbles, of which the runs are directional movements with constant speeds, and the tumbles are random reorientations of the cell body with negligible displacements. However, the motion of the bacteria-driven microrobots is characterized as a movement with relatively stable speed but incessantly changing heading direction. The propulsive forces exerted on a microrobot at an arbitrary moment can be reduced to a force and a torque which are normally noncolinear [34]. In spite of the difference in the motion between the free swimming bacteria and the microrobots, they share the same driving mechanism for chemotaxis in a general sense, namely, the heading direction is more persistent when moving towards higher concentrations of chemoattractant. A consistent heading bias is also found on the free-swimming bacteria, as shown in Fig. 3.16(a), but it is less pronounced than that revealed on the bacteria-driven microrobots; this discrepancy is due to the prominent wall effect on the motion of free-swimming bacteria, where their natural chemotactic transport is constrained by the channel wall. The free swimming bacteria also manifests a slight speed bias during chemotaxis in a similar fashion, as shown in Fig. 3.16(b). Assuming no chemical interactions between the bacteria attached to the same microrobot, it is the flagellar rotation dynamics of the individual bacteria in response to their local chemical concentration changes that leads to the seemingly cooperative behavior of the attached bacteria during chemotaxis. As we will see in Chapter 4, a similar physical mechanism has also been found in the pH-taxis of the

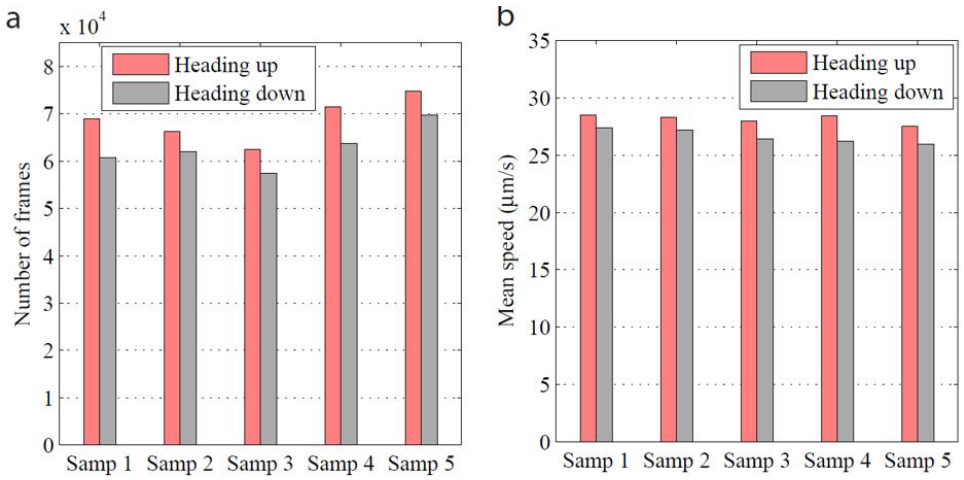

Figure 3.16: Heading bias (a) and speed bias (b) of free swimming bacteria under an L-serine gradient of 0.1 mM/mm. Five experiments were conducted on independent bacterial samples in the three-channel microfluidic concentration generator, and each sample has around 2000 bacterial swimming trajectories extracted and analyzed. The result shows that there is a consistent heading bias towards the up-gradient direction (a), where the time spent on moving towards the higher concentrations is about 10% longer than that spent on moving towards the lower concentrations. In addition, compared to the mean speed of down the gradient, the free swimming bacteria manifest a slightly higher (5% higher) speed when swimming up the chemoattractant gradient.

bacteria-driven microrobots, which in turn corroborates that a similar signaling pathway model is shared between pH-taxis and chemotaxis [110, 111].

Differences in the measured values are seen across the five analyzed samples, as shown in Fig. 3.13(a, b). One source of these differences is the variances in the fabrication process between samples. For example, the mean speed of the bacteria-driven microrobots mainly depends on the average motility of the bacteria and the mean number of bacteria attached to a microrobot. Since the bacterial motility and the percentage of motile bacteria are associated with the location where the bacteria are extracted from the colony [55], slight discrepancies in the extracting location of bacteria among the samples could introduce variances in the mean speed between samples. In general, the bacterial motility parameters, such as the mean speed and the mean tumble rate, as well as the average number of bacteria attached to a microrobot all affect the motion characteristics, such as the mean speed and the heading direction reversing

rate.

The results of this study not only help us better understand the physical mechanisms of chemotaxis in bacteria-driven microrobots, but also offer us some guidelines for designing and fabricating bacteria-driven microrobots with enhanced chemotactic performance. We find that the chemotactic drift velocity increases superquadratically with the mean speed. Therefore, an effective way to enhance the chemotaxis in bacteria-driven microrobots is to increase their mean speed, which can be achieved by various techniques, such as using bacteria with higher motility, aligning the bacteria on microrobots instead of random attachment, patterning the attachment location [50] to increase the net propulsive force, and possibly decreasing the size or modifying the shape [51] of microrobots to reduce the Stokes' drag coefficient. On the other hand, depending on the availability or ease of deployment of a certain chemical gradient, chemotaxis may be applied interchangeably with other taxes to implement drift control in bacteria-driven microrobots. The resemblance between chemotaxis and pH-taxis (studied in the next chapter) in the bacteria-driven microrobots suggests that any potent tactic behavior of free swimming bacteria that shares a similar signaling pathway with chemotaxis can be utilized to yield effective drift control of properly designed bacteria-driven microrobots.

3.7.2 Summary

In this chapter, we have shown that potent chemoattractant can perform effective drift motion control on properly designed bacteria-driven microrobots. The chemotactic drift in a multi-bacteria-driven microrobotic system has been characterized, and the physical mechanism of the associated chemotactic motion has been elucidated. First, we introduced the swimming model of the bacteria-driven microrobots, which will also be used for the pH-taxis study in Chapter 4. Before investigating the chemotaxis in the bacteria-driven microrobots, we studied the chemotactic response of their actuators, *S. marcescens* bacteria, towards a potent chemoattractant of L-serine, and the optimal concentration gradient (0.1 mM/mm) that elicits the highest chemo-

tactic velocity was found. Subsequently, using the optimal concentration profile of L-serine, we quantified the chemotactic drift of the bacteria-driven microrobots, and for the first time we elucidated the physical mechanism associated with the chemotactic motion by the statistical analysis of over a thousand swimming trajectories of the bacteria-driven microrobots. The results show that the microrobots have a strong heading preference for moving up the L-serine gradient, while their speeds do not change considerably when moving up and down the gradient; therefore, the heading bias constitutes the major factor that produces the chemotactic drift. The heading direction of a microrobot was found to be significantly more persistent when it moves up the L-serine gradient than when it travels down the gradient; this effect causes the apparent heading preference of the microrobot and is the crucial mechanism that enables the seemingly cooperative chemotaxis of the multiple bacteria on a microrobot. At last, we found that the chemotactic drift velocity of the microrobots increases superquadratically with their mean swimming speed, suggesting that chemotaxis can be enhanced by designing and building faster microrobots.

Chapter 4

pH-Taxis of Bio-Hybrid Microrobots

4.1 Introduction

Maintaining an appropriate pH level is vital to the survival of most microoganisms like bacteria, and they have evolved various sensing and regulatory strategies to adjust their cytoplasmic pH [112, 113]. Flagellated bacteria such as *E. coli* have also been found to exhibit bidirectional pH-tactic behavior [110, 111, 114], i.e., moving away from both strong acidic and alkaline pH environments, as illustrated by Fig. 4.1. Given the pH tactic response of these bacterial strains and knowing that cancerous tumors have a lower pH compared to that of periphery normal tissue [115, 116], it would be enticing to explore the potential of applying pH-taxis based control of bacteria-driven microrobotic systems for targeted drug delivery applications. To further explore the feasibility of such an approach, greater insight into the pH-tactic behavior of typical bacteria-driven microrobots is required.

In this chapter, we present a method that takes advantage of the bacterial sensing of ambient pH to achieve robust drift control of bacteria-driven microrobots. The same design and fabrication procedure are followed to prototype the bacteria-driven microrobots for the pH-taxis study. *S. marcescens* is employed as the bioactuator, not only because it is a typical flagellated bacterial strain with high motility and tactic behaviors, but also because of its natural adhesion

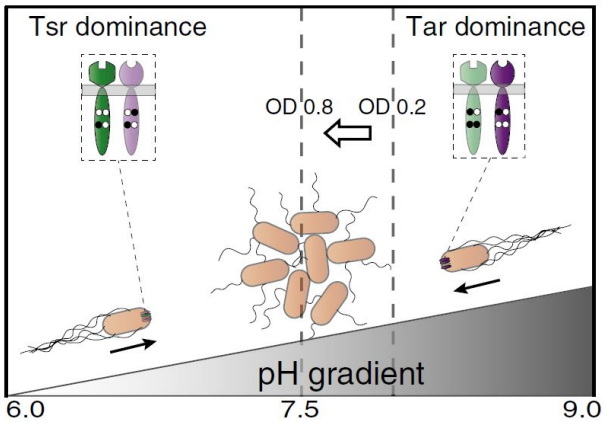

Figure 4.1: Bacterial pH-tactic migration towards their preferred pH region, enabled by the opposite pH-tactic responses of two major receptors *Tar* and *Tsr* (reprinted from [110]).

to negatively-charged, hydrophobic surfaces [55, 63], which greatly simplifies the assembly process of the microrobots. *S. marcescens* bacteria swim in liquid environments by incessant alternation of run and tumble states similar to *E. coli* [66], with an average tumble rate measured to be around $1.3\ \mathrm{s}^{-1}$ [55]. Their mean swimming speed can be as high as 47 μm/s [20]. Temperature responses and chemotaxis of *S. marcescens* have been characterized and have also been found to resemble those of *E. coli* [54, 55, 57]. Since a common signaling machinery is suggested for chemotaxis, thermotaxis, and pH-taxis [111], it is expected that *S. marcescens* also maintain a similar pH-tactic behavior as *E. coli*.

To perform a drift control study of bacteria-driven microrobots, we use the three-channel microfluidic device (see details in Appendix B) to generate three stable pH gradients. The bidirectional pH-taxis of free swimming bacteria is observed for the first time using the configured pH gradients; tracking of the swimming bacteria allows us to determine that the bacterial pH-tactic motion is mediated by the biased flagellar tumble rates. Subsequently, we study the distribution and motion of the microrobotic swarms driven by *S. marcescens*. Depending on the applied pH gradient profile, the bacteria-driven microrobots are shown to exhibit either bidirectional or unidirectional tactic motion. Since it is not intuitively clear how a microrobot with multiple bacteria attached in random directions can produce the similar pH-tactic response as

free-swimming bacteria, we perform a detailed analysis on the swimming trajectories of individual microrobots, which enable us to conclude that it is two motion bias factors that contribute to the tactic drift of the bacteria-driven microrobots.

4.2 pH Gradient Calibration

Unlike the generation of pH gradients by electrolysis [117], a diffusion-based method can eliminate the electrical field induced effects on the motion of bacteria-driven microrobots. Therefore, a flow-free diffusion based gradient generator design [70, 71] was applied to fabricate the pH gradient generator. As shown in Fig. 4.2(a,b), the gradient generator consists of three parallel channels, namely the sample channel and two side channels. The width of the channels is 500 μm and the height is around 200 μm. The channels are separated from each other by two 250 μm wide agarose gel ridges. A constant flow of fluid was pumped through the outlets of the two side channels, whereas the outlets of the sample channel were sealed to decrease undesired drift flows. A programmable syringe pump (Braintree Scientific Inc.) was used to pump fluid with different pH values into the two side channels at a flow rate of 5 μL/min. Generation of a linear concentration gradient in the device has been fully calibrated in Chapter 2.

To create solutions with different pH values, either HCl or NaOH solution was added to motility buffer (0.01 M KH_2PO_4, 0.067 M NaCl, 10^{-4} M EDTA, pH = 7.0). Three stable pH gradients were generated by pumping motility buffer with different values of pH into the two side channels of our device. To verify the existence of a stable pH gradient in the sample channel, the same concentration of an appropriate pH indicator was added to all three channels. The pH gradients were visualized *in situ* and the pH transition in the sample channel was determined, as shown in Fig. 4.2(b). Based on the indicator color charts and the resulting color profiles, the following pH ranges were measured: Gradient 1 maintains a pH range between 6.0 (bottom) and 7.6 (top) in the sample channel, and a neutral pH region lies close to the center line of the sample channel; Gradient 2 maintains a pH range between 3.8 (bottom) and 5.4 (top),

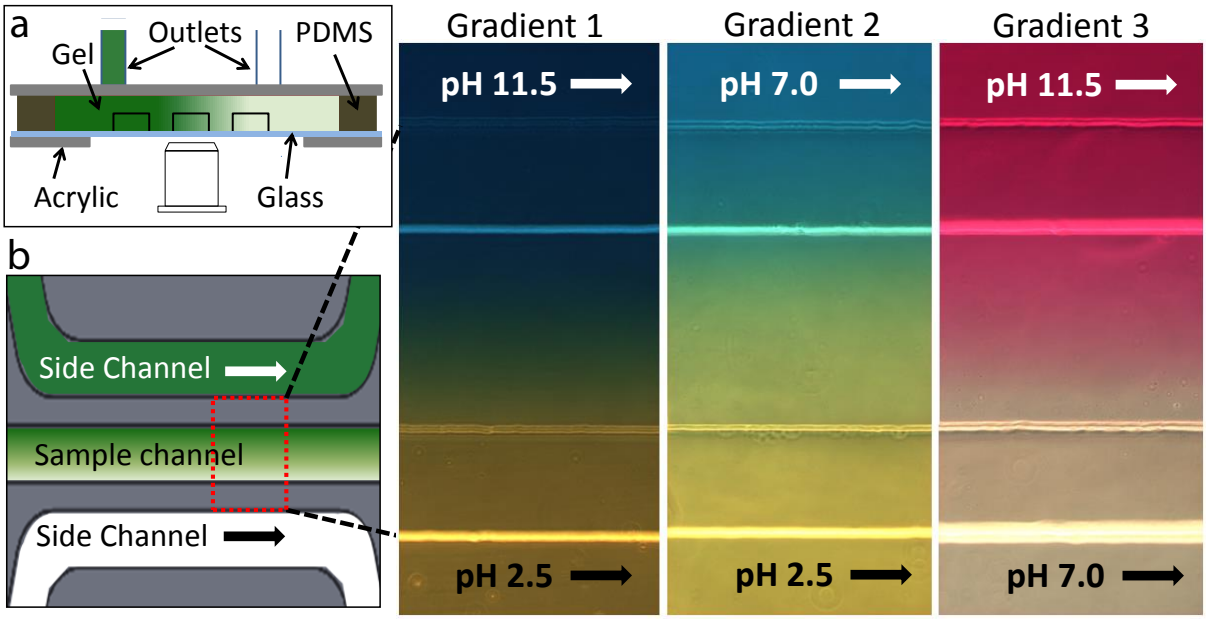

Figure 4.2: (a) Configuration of the three-channel diffusion-based pH gradient generator (side view). (b) Top view of the three parallel channels and the three gradient profiles visualized *in situ* by three appropriate pH indicators, where bright lines in the color profiles indicates the channel walls. The pH gradient in the sample channel was generated by pumping two fluids with different constant pH values into the side channels, while the sample channel was completely closed and quiescent. The pH indicators used to visualize the three gradients from left to right were Bromothymol Blue (sensitive pH 6.0 - 7.6, with color transitioning from yellow to blue), Bromocresol Green (sensitive pH 3.8 - 5.4, with color transitioning from yellow to blue) and Cresolphthalein (sensitive pH 8.2 - 9.8, with color transitioning from colorless to purple).

creating a more acidic environment along the bottom; the color profile of Gradient 3 indicates a pH range between 8.2 (bottom) and 9.8 (top), showing that the top is more alkaline. The pH gradients generated by the diffusion of ions were verified to be stable by the constant color profiles of the indicators after the estimated diffusion time. Since the time scale of ionization and recombination is negligible compared to that of diffusion, the diffusion time of H^+ (0.9 min) and OH^- (1.6 min) across the two side channels was used to characterize the stabilization time of the pH gradients. In addition, we can treat the ionization of the sample solution to be quasistatic at each moment, i.e., there was no electric field induced by the diffusion of ions.

4.3 pH-Taxis of Free-Swimming Bacteria

Using a diffusion based microfluidic gradient generator, three stable pH gradient profiles (named Gradient 1, 2 and 3 for convenience) were created in a quiescent fluidic channel, where samples of bacteria and bacteria-driven microrobots were loaded and tested. Gradient 1 was created to study the bidirectional pH-taxis of bacteria and also to demonstrate that the bacteria-driven microrobots can be navigated by the ambient pH distribution, while Gradients 2 and 3 were used to quantify the unidirectional drift of the bacteria-driven microrobots and therefore unveil the multi-bacterial driving and steering mechanism.

4.3.1 Bacterial Bidirectional pH-taxis

Based on recent fluorescence resonance energy transfer (FRET) results as well as mathematical models, it has been proposed that *E. coli* is capable of taxis away from both strongly acidic and alkaline environmental conditions, resulting in accumulation of the bacteria at an optimal pH region [110, 114]. However, such bidirectional taxis has never been visualized directly, and the associated swimming behavior has not been studied. Using Gradient 1 (pH: $\sim$6.0 to 7.6+), which is a stable pH gradient that covers the pH transition from acidic to alkaline, we were able

to observe the bidirectional pH-taxis of *S. marcescens* (see Appendix A for growing conditions.) directly. As shown in Fig. 4.3(a, b), the bacteria accumulate to form a band around the center line of the sample channel after about 1.5 min from the start of the experiment; the position of the band corresponds to a pH value slightly above 7.0. From the color chart of the pH indicator, the optimal pH was found to correspond to values between 7.0 and 7.3. The distribution profile shows a sharper decrease in bacterial number in the transition from ambient to alkaline pH than the transition from ambient to acidic pH; this is probably due to the drastic pH change at this corresponding location.

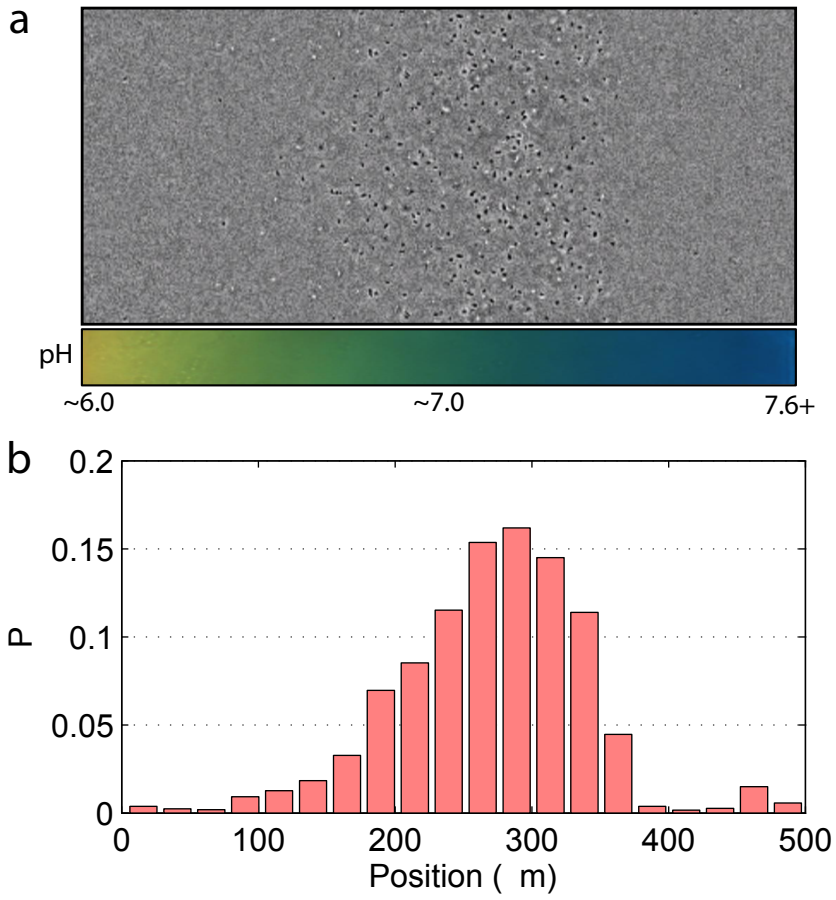

Figure 4.3: Bacterial bidirectional pH-taxis. (a) A phase contrast image of the free swimming *S. marcescens* at steady state (stabilized after ∼1.5 min) under Gradient 1, where the black and white dots are cell bodies of bacteria. (b) Probability distribution of bacteria position extracted from multiple images at steady state.

4.3.2 Bacteria Tumble Rate Distribution

Bacteria in an isotropic environment follow a purely random walk, which generates a uniform distribution of bacteria in a bounded space at steady state; a nonuniform distribution of incessantly moving bacteria in our sample channel reveals a motion deviating from a random walk. A biased distribution of bacteria is often seen in bacterial chemotaxis, which has been attributed to a biased tumble rate distribution based on swimming direction. Since FRET results [110] indicate that similar signaling pathways are employed in both bacterial pH-taxis and chemotaxis, it is reasonable to expect that the banded distribution of *S. marcescens* under a pH gradient is also a result of a biased tumble rate. By tracking the bacterial swimming direction and detecting the number of tumble events in two rectangular regions with pH values below and above the optimal value, we find that the tumble rate distribution is significantly biased and is dependent on the swimming direction (Fig. 4.4). For both regions, the average tumble rate (based on $\sim$2000 trajectories) of the bacteria is found to be substantially lower when swimming toward the optimal pH ($\sim$1.0 s^{-1}) than when swimming toward the opposite direction ($\sim$1.5 s^{-1}). Our results corroborate the reported bidirectional pH-taxis signaling pathway model [114] and indicate a resemblance between *E. coli* and *S. marcescens* in terms of pH-tactic behavior.

4.4 pH Tactic Drift of Microrobotic Swarms

In this section, we characterize the pH tactic drift of the bacteria-driven microrobotic swarms under: (a) bidirectional pH-taxis away from both acidic and alkaline regions (Gradient 1), and (b) unidirectional pH-taxis away from more acidic region or more alkaline region (Gradient 2, 3). All the experiments were done at room temperature, around 20°. The video recording was started immediately after the initiation of flows in source and sink channels.

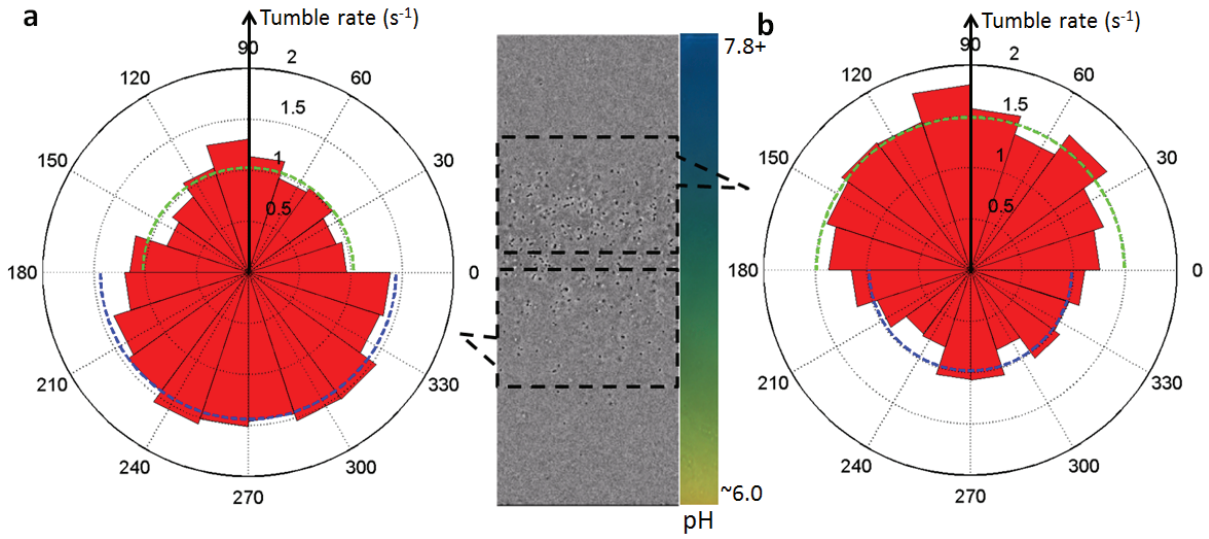

Figure 4.4: Bacterial tumble rate distribution (Gradient 1). A phase contrast image of the bacterial distribution in the sample channel is shown in the middle; the image height corresponds to the full channel width. (a) Tumble rate distribution on the acidic side of optimal pH ($\sim$7.0). (b) Tumble rate distribution on the basic side of optimal pH. In both cases, the average tumble rate when bacteria move towards the optimal pH is around 1.0 s^{-1}, while it is around 1.5 s^{-1} when moving towards unfavored pH regions.

4.4.1 Bidirectional Tactic Drift

By exposing a large number of microrobots to Gradient 1, we demonstrate pH-tactic drift of the bacteria-driven microrobots. As shown in Fig. 4.5, the microrobots were initially uniformly distributed. Over time, the uniform distribution evolves into a dense band of microrobots located around the centerline of the channel. This steady state distribution is achieved after about 6 minutes. The most probable location for the bacteria-driven microrobots at steady state, which is shown in Fig. 4.6, coincides with that of free swimming bacteria (the optimal pH value). A side by side comparison between the distribution profile of free swimming bacteria and microrobots indicates a high degree of resemblance; in both distributions, there is a sharp decrease on the alkaline side of the optimal pH.

4.4.2 Unidirectional Tactic Drift

While the bidirectional pH-taxis shows the versatility of bacterial pH-taxis, it is preferable to study the bias factors that drive the tactic behavior under unidirectional taxis. Therefore, two more pH gradients, Gradient 2 (pH: 3.8- to 5.4+) and Gradient 3 (pH 8.2- to 9.8+) (see more details in the methods section), were created to achieve the unidirectional drift control of the bacteria-driven microrobots. It took approximately 10 minutes for the majority of the microrobots to accumulate on one side of the channel in the two cases studied: taxis away from a more acidic condition (Fig. 4.7(a)) and taxis away from a more alkaline condition (Fig. 4.7(b)).

By image processing, the y component of the center of mass (COM-y, see details in Chapter 3) of the microrobots in the sample channel can be computed at different time points. In Fig. 4.8(a, b), the drift behavior is shown to be highly consistent among the three tested samples for the two cases. In the drifting process, some microrobots reached the channel wall and stopped their drifting motion but were still taken into account when calculating the average COM-y. This results in an artificial decrease in the slope of the COM-y over time as shown in Fig. 4.8(a, b). Thus, the time derivative of the COM-y produces an underestimation of the actual pH-taxis

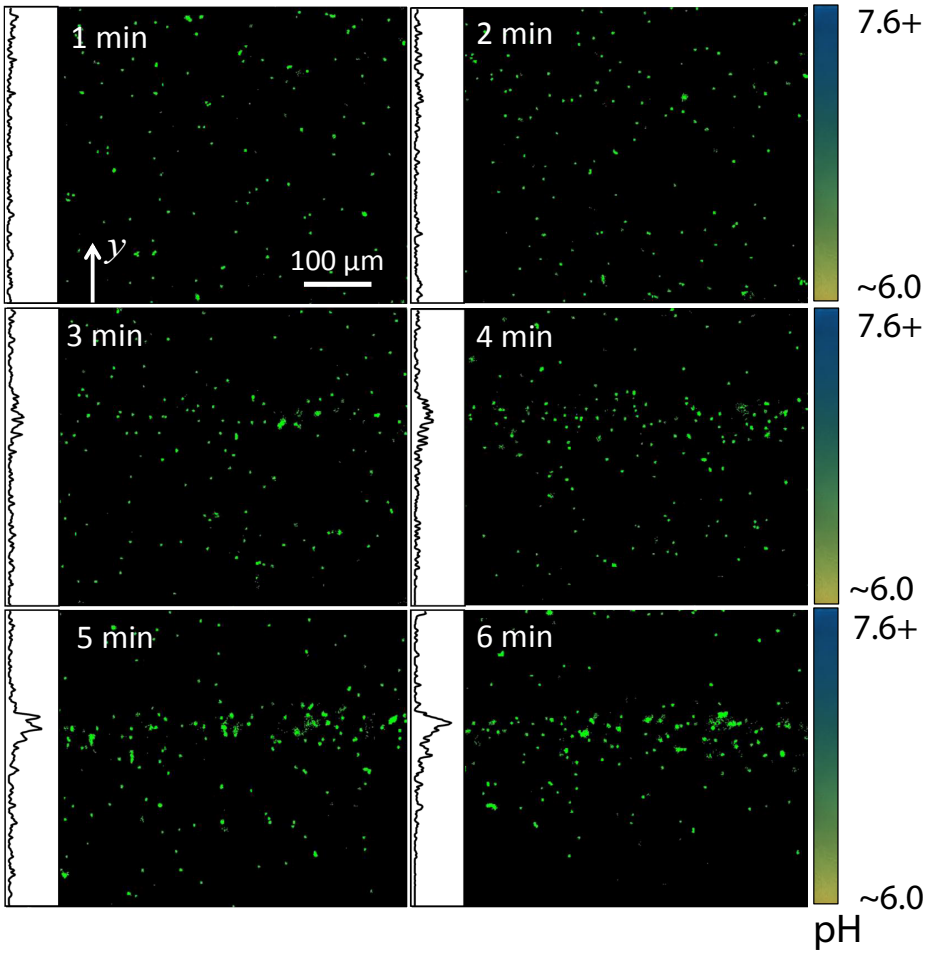

Figure 4.5: Fluorescent images of the microrobots (green dots) show the evolution of the microrobot distribution in a fixed focal plane over time. The height (y dimension) of each image covers the full channel width. The inset on the left side of each panel indicates the intensity profile of the frame along the y-axis. The color bars on the right hand side indicate the ambient pH gradient profile (Gradient 1).

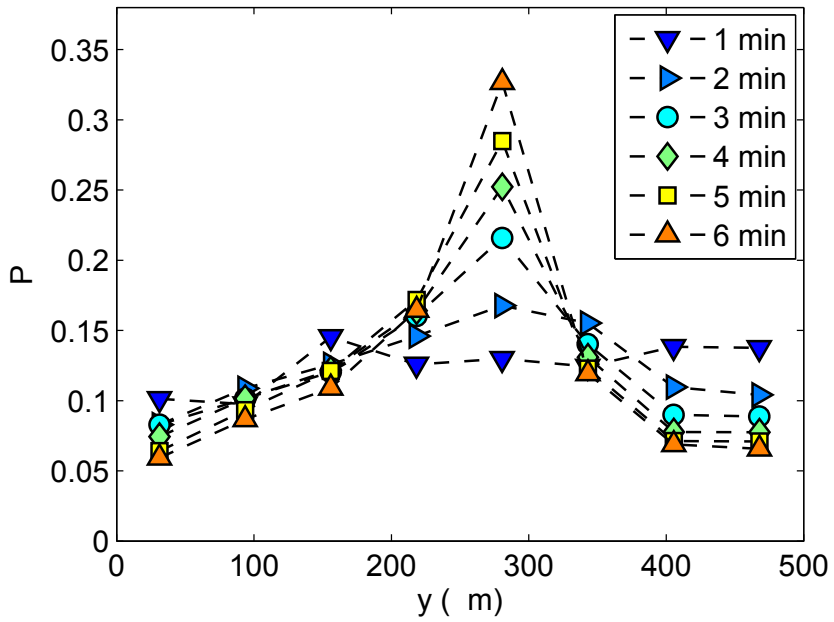

Figure 4.6: Probability distribution of the microrobot position across the width of the sample channel, where each distribution is averaged from 200 fluorescent images taken around the corresponding time point.

drift velocity of the microrobotic swarm; a more accurate characterization of the pH-taxis drift velocity is obtained in the following section via analysis of the swimming trajectories of the microrobots.

4.5 Phenomenological Mechanisms of pH-Taxis in Microrobots

4.5.1 Tracking of Microrobots and Trajectory Analysis

To understand how a bacteria-driven microrobot, which consists of a microsphere propelled by a group of randomly oriented bacteria, is endowed with pH-taxis capabilities, we tracked the individual microrobots subjected to unidirectional pH-taxis. Details of the visual tracking system were described in Chapter 3. Motions of slowly moving microrobots are susceptible to

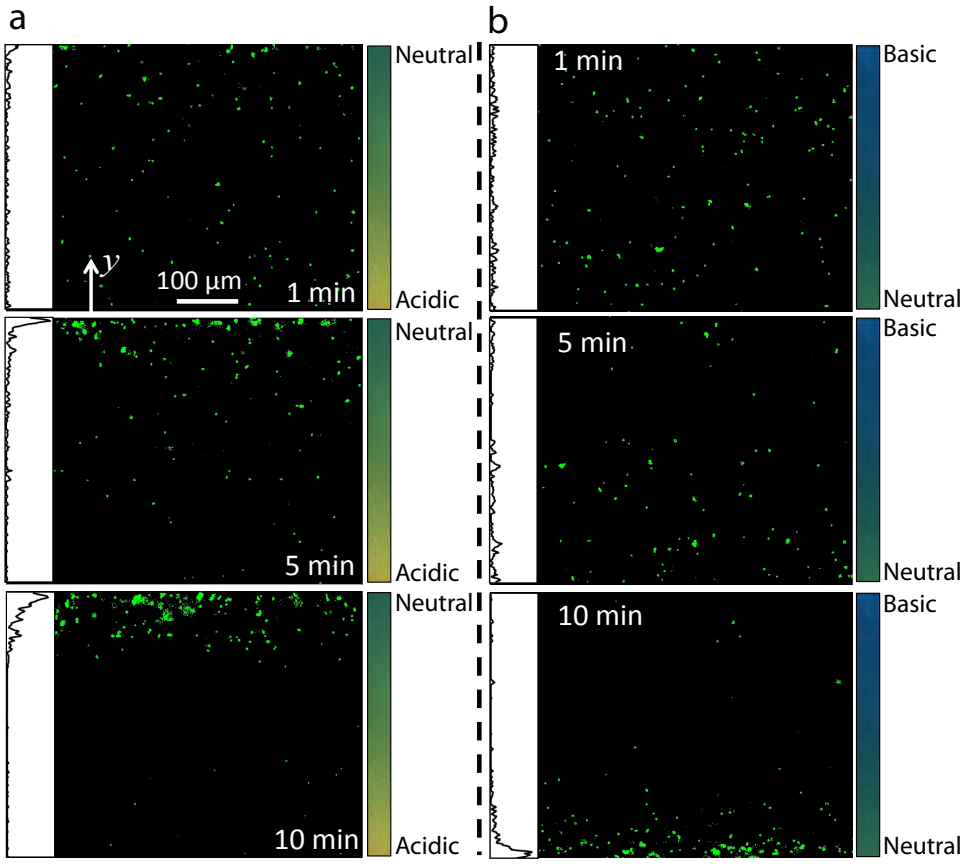

Figure 4.7: Unidirectional pH-tactic drift of bacteria-driven microrobots. Fluorescent images show the tactic motion of microrobots away from more acidic (a) and more alkaline (b) conditions in the sample channels, where Gradients 2 and 3 were applied, respectively. The inset on the left side of each panel in (a) and (b) indicates the intensity profile of the frame along the y-axis.

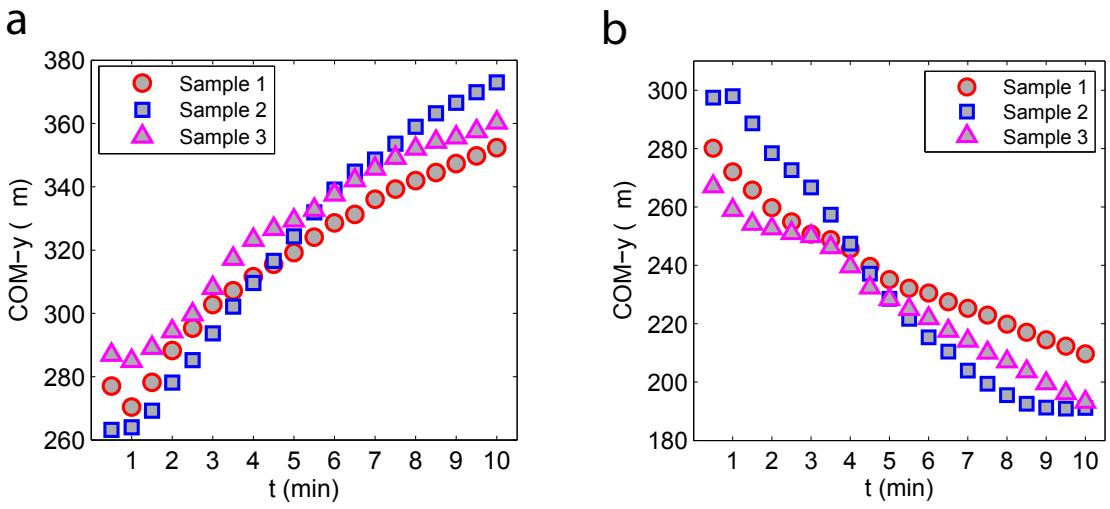

Figure 4.8: Drifting process of bacteria-driven microrobotic swarm characterized by the COM-y of the swarm: (a) and away from more alkaline regions (b). The results for three different system samples are shown for each case.

ambient flows (0.41 $\pm$ 0.21 μm/s); thus we only included the trajectories of the microrobots with an average speed greater than 4 μm/s ($\sim$10 times the ambient flow speed) in our analysis. In addition, trajectories that came within 50 μm ($\sim$15 times the body length of the microrobot) of the walls were removed from the analysis since these microrobots were subjected to wall effects. Using these two criteria, over 900 trajectories were collected and analyzed for each swarm sample undergoing unidirectional taxis. A number of sample trajectories are plotted in Fig. 4.9, where the locations of the trajectories represent their real locations in the sample channel. The same 1D drift model (Eq. 3.6) and trajectory decomposition method (see details in Chapter 3) were used to analyze the trajectories of the bacteria-driven microrobots under pH-taxis.

4.5.2 Heading Bias

The heading direction of all the trajectories (from three swarm samples) were determined on a frame-by-frame basis. By counting the number of frames where the swimming direction (i.e.

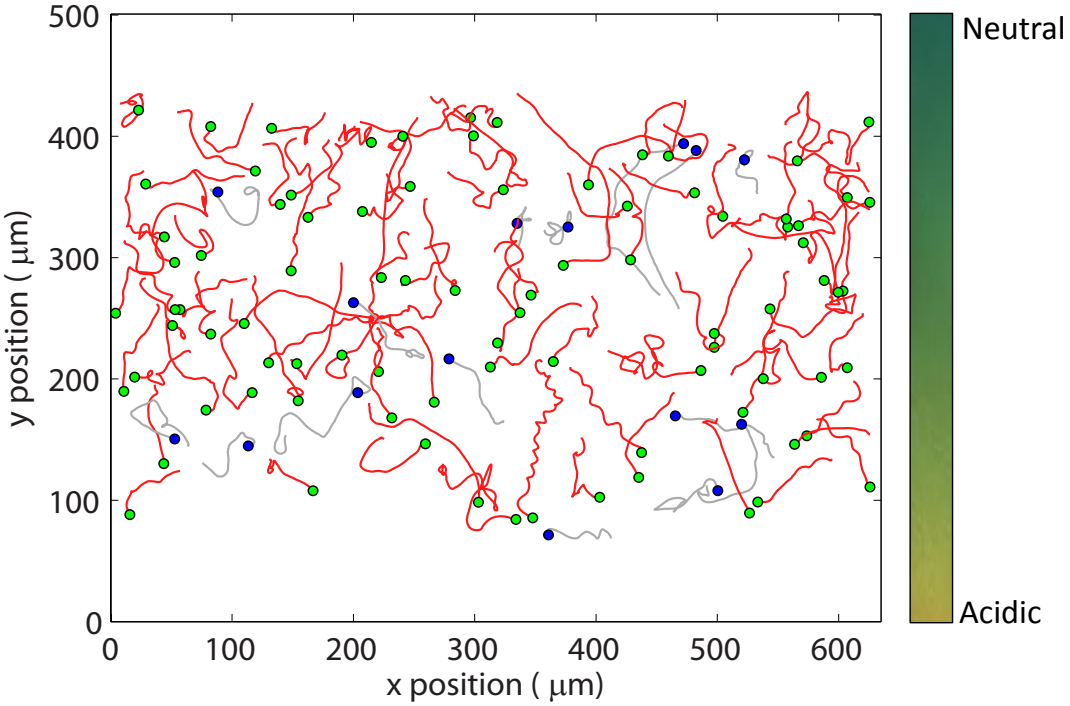

Figure 4.9: Sample swimming trajectories of bacteria-driven microrobots. The trajectories are randomly picked from the previous samples undergoing unidirectional taxis away from an acidic pH condition (Gradient 2). The starting positions are marked by circles (green and blue); the red trajectories have net y-displacements from acidic to neutral pH, while the gray ones have net y-displacements from neutral to acidic pH.

orientation angle) was within a defined angle interval, the probability distributions of the swimming heading could be generated. The distributions also represent the portion of time that the microrobots spend on swimming in each direction. Substantial biases in heading distributions are observed in Fig. 4.10(a, b). The least probable swimming directions correspond with the unfavorable conditions and the most probable directions correspond with the favorable conditions. The heading distribution provides a quantification of the swimming angle preference of the microrobots and can be used to calculate the tactic drift velocity; however, it is not intuitively clear how the heading bias is achieved. Our following study on the swimming direction reversing rate along the y-axis (pH gradient direction) sheds light on the answer.

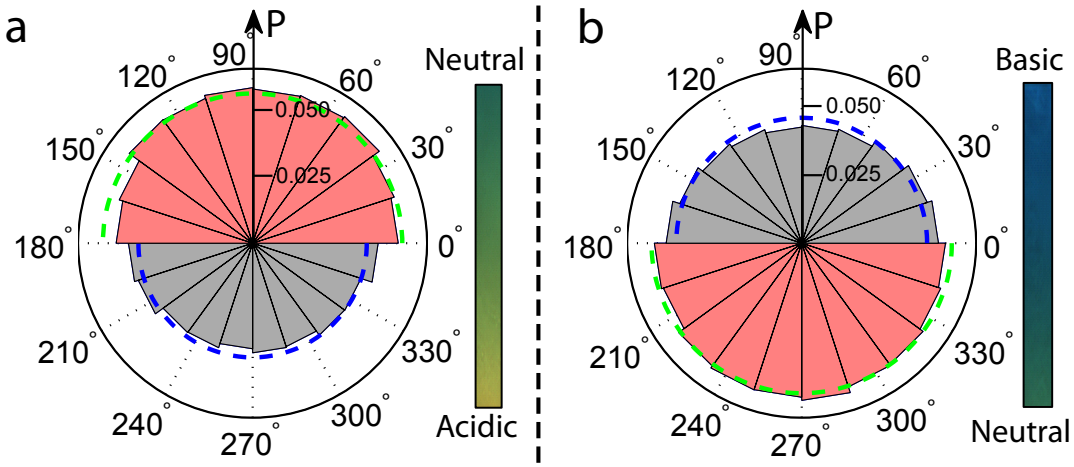

Figure 4.10: Probability distributions of the swimming heading in 2D, (a) Away from more acidic condition, (b) Away form more alkaline condition. The pink color indicates results from motion towards favored pH regions while the gray color shows the corresponding results from motion towards unfavored pH regions; this rule is also true for Fig. 4.11 and Fig. 4.12.

4.5.3 Speed Bias

In addition to the heading bias, there is also a bias in the average swimming speed with respect to the swimming direction (Fig. 4.11(a, b)); namely, a higher speed is observed when moving toward the favored pH region. Due to the low Reynolds number of the swimming motion, the hydrodynamics of a swimming bacteria-driven microrobot can be described by Stokes' law,

as described in detail in Chapter 3. From the linear relationship between $\boldsymbol{F}$ and $\boldsymbol{v}$, we can conclude that on average the bacteria attached to a microrobot exert a higher propulsive force on the microrobot when it moves towards a favored pH environment.

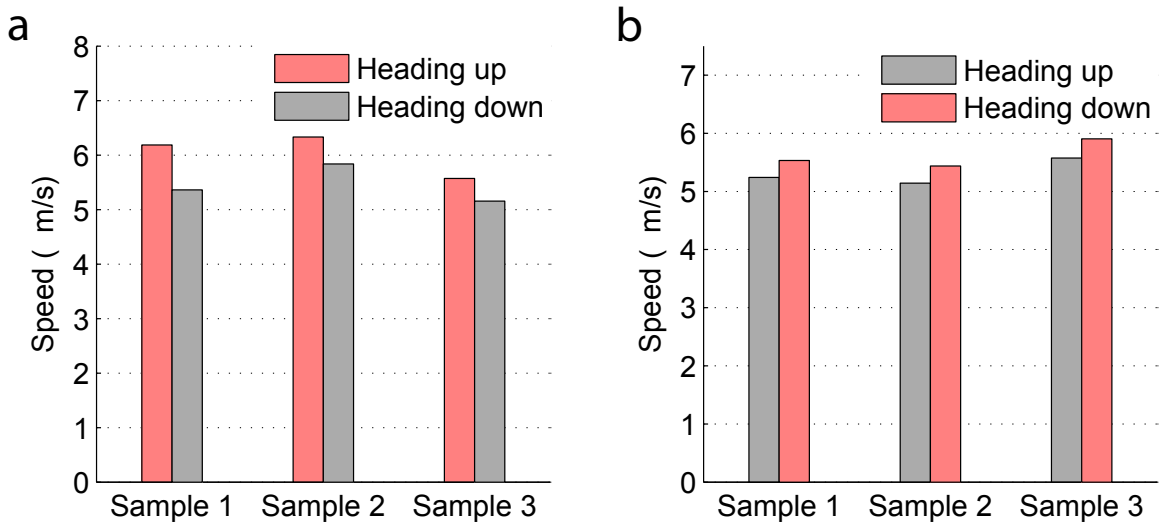

Figure 4.11: Average 2D swimming speed with respect to the heading direction along the y-axis. (a) Away from more acidic condition, (b) Away form more alkaline condition.

4.5.4 pH Tactic Drift Velocity

Base on Eq. 3.6, the 1D drift velocity of the bacteria-driven microrobots in the gradient direction can be readily computed from our measurements on the heading bias, speed bias, and the average swimming speed along the pH gradient direction. The average headings (the dashed arcs in Fig. 4.10) are used to evaluate the average heading time bias β (expressed in the methods section). The drift velocities of the two cases (moving away from more acidic pH regions and moving away from more alkaline pH regions) were calculated to be similar, both of which are around 0.5 μm/s. We further examined the relative contributions of the heading bias and speed bias to the overall drift velocity: the heading bias contributes to $\sim$75% of the total drift velocity while the speed bias contributes to $\sim$25% of the total. This indicates that, in addition to the

heading bias, the speed bias is an essential mechanism of the microrobot's tactic motion; this is a departure from the mechanisms known to cause the biased random walk observed in free swimming bacteria under pH-taxis or chemotaxis.

4.5.5 Direction Reversing Rate Bias

In Fig. 4.12(a, b), we present the heading direction reversing rate (y-component) of the bacteria-driven microrobots with respect to their heading directions. Since the y component of the velocity of a microrobot determines whether the microrobot is swimming towards the optimal pH region or not, we classified the headings of all frames into two groups in terms of their y direction: heading towards the optimal pH (shaded in red) and heading away from the optimal pH (shaded in gray). The direction reversing rate of each heading group is simply defined as the total number of y direction switchings (from $+y$ to $-y$ or vice versa) observed in that group divided by the total number of frames of that heading group. As shown in Fig. 4.12(a, b), across the three different samples of each case, the average direction reversing rate when the microrobots move towards favored pH regions is consistently smaller than that of moving towards unfavored pH regions. In other words, the orientation of the bacteria-driven microrobots is more persistent and less likely to change when they move towards the favored pH regions; this yields a larger portion of time spent moving towards an optimal pH region, as revealed by the heading bias in Fig. 4.10(a, b).

4.5.6 Dependence on Speed

Since a wide variance in the swimming speeds of the bacteria-driven microrobots was observed, it is meaningful to inquire about the potential influence of the absolute swimming speed on the motion bias. To analyze the dependence on swimming speed, the captured trajectories for each unidirectional pH-taxis case were divided into groups based on their mean instantaneous speed, as shown along the x-axis in Fig. 4.13. The relative reversing rate bias ($(r^- - r^+)/(r^- + r^+)$,

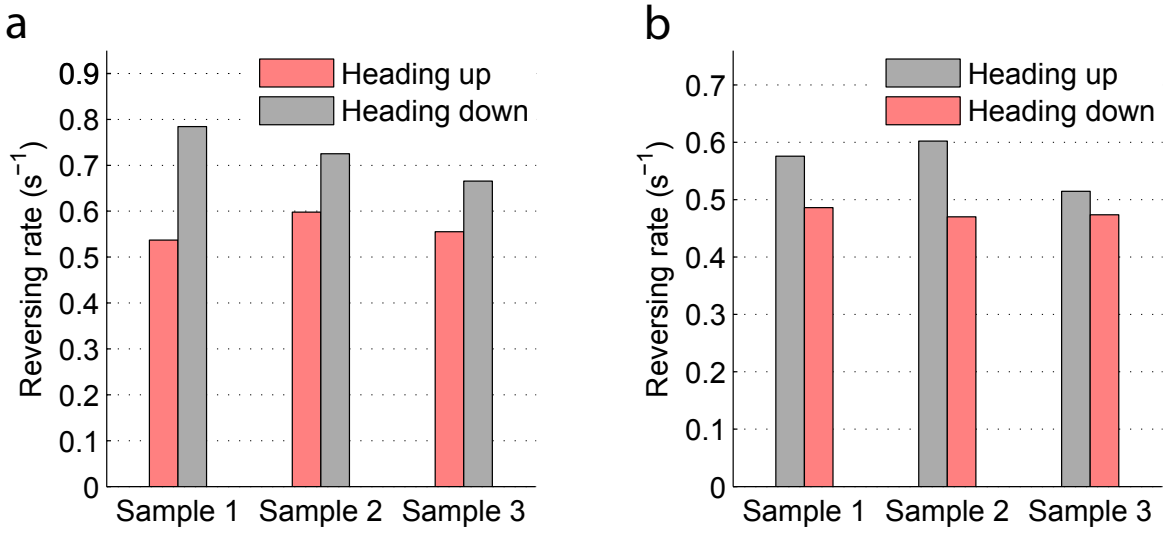

Figure 4.12: Heading direction reversing rate with respect to the heading direction along the y-axis. (a) Away from more acidic condition, (b) Away form more alkaline condition.

where r^- and r^+ are reversing rates towards and away from optimal pH, respectively) quantifies the dependence of the drift velocity on the direction reversing rate [68]. Both speed and relative reversing rate biases increase with increasing mean swimming speed, and this trend holds true for both cases (away from acid, away from base). Since the speed bias and reversing rate bias (or heading bias) are factors that contribute to a biased random walk, it can be concluded that the bacteria-driven microrobots exhibits a stronger tactic motion when a higher swimming speed is achieved.

4.6 Discussion and Summary

4.6.1 Discussion

We have studied the pH-tactic behavior of a large number of bacteria-driven microrobots in a microfluidic channel with a stable spatial pH gradient. It has been demonstrated that the spatial pH gradient can effectively and consistently generate drift motion in the biohybrid system. To

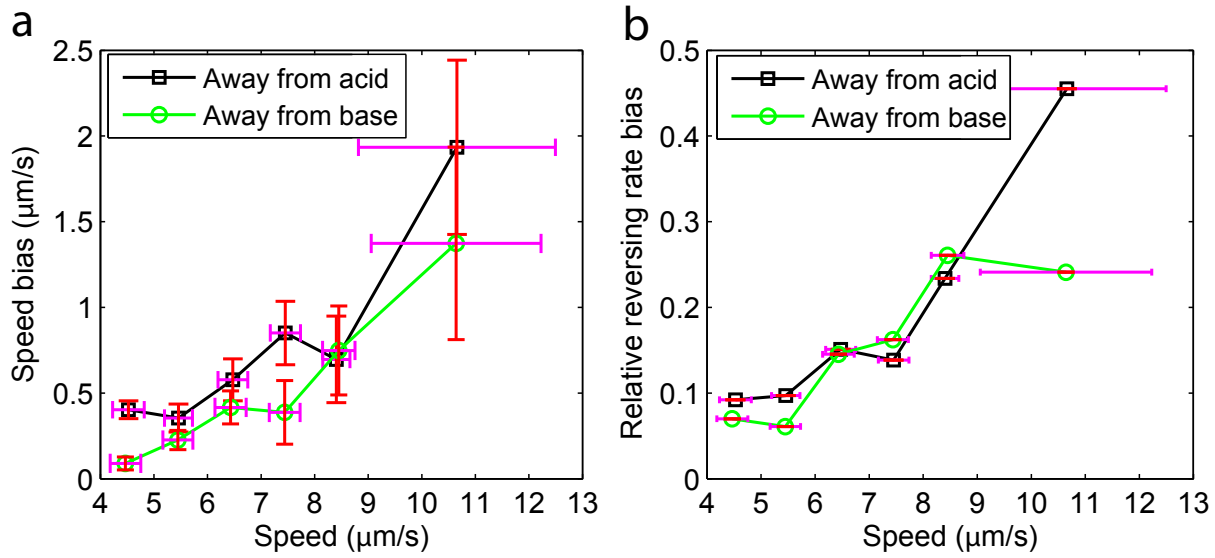

Figure 4.13: Dependences of motion biases on the swimming speed. (a) Swimming speed bias with respect to the average swimming speed. (b) Relative reversing rate bias with respect to the average swimming speed. The horizontal error bars indicate the standard deviation of mean speeds for the trajectories grouped within a given speed interval (4 - 5, 5 - 6, 6 - 7, 7 - 8, 8 - 9 and ≥ 9 μm/s). The vertical error bars in (a) denote the standard deviation of the speed bias for the trajectories falling within the corresponding speed intervals. In both (a) and (b), each speed interval has over 80 sample trajectories measured.

fully understand the biased motion of the bacteria-driven microrobots and the mechanisms that produce the biased motion, we tracked individual microrobots and analyzed their trajectories. For free swimming bacteria, the tumble rate is biased with respect to swimming direction, yielding a heading bias, which in turn generates a pH-tactic or chemotactic drift velocity. However, unlike the clear run and tumble switching pattern of free swimming bacteria, the motion of bacteria-driven microrobots can be described as an incessant translation with gradual changes in heading direction. From a trajectory analysis, the drift velocity of the bacteria-driven microrobots under a stable pH gradient is found to result from two factors, namely, the heading bias and the swimming speed bias.

To explain how the heading bias is produced in the bacteria-driven microrobots, we must understand the effect of pH on the flagellar tumbling rate. Free swimming bacteria increase their flagellar tumbling rates when moving towards unfavored pH regions or when sensing unfavored temporal pH changes. Since the assembly of bacteria onto micro polystyrene beads relies on physical adherence, we do not expect fundamental changes to the chemical sensing machinery of the bacteria after integration with the beads. Therefore, when a microrobot moves toward unfavored pH regions, the average flagellar tumbling rate of the attached bacteria tends to increase, and this introduces more disturbances to the motion of the microrobot by frequently changing the applied forces and torques. As a result, compared with the motion towards favored pH regions, the microrobots maintain less consistency in their swimming directions when moving towards unfavorable pH regions; this leads to the reversing rate bias and hence the heading bias.

As we already discussed, the swimming speed bias reveals a bias in the propulsive force on the bacteria-driven microrobot. Presumably, when a microrobot moves towards a favorable pH, less flagella are in a tumble state than when compared to moving towards an unfavorable pH. However, a detailed observation of the flagellar morphology when bacteria are attached to a moving objects is essential to fully understand the physical mechanisms. The dependencies of

the motion bias on the swimming speed is potentially due to the fact that bacteria sense the temporal change of the ambient pH [67]; since the spatial pH profile is constant, it is the swimming velocity that determines the temporal pH gradient seen by the bacterial receptors. Therefore, the enhanced motion bias at higher swimming speeds could be explained by a stronger temporal pH gradient being sensed.

The work of Hu and Tu indicates that a common biochemical signaling pathway is responsible for different kinds of bacterial taxis behaviors, including pH-taxis, chemotaxis, and thermotaxis [111]. We have demonstrated the motion guiding of bacteria-driven microrobots via chemotaxis, and it is highly possible that appropriate temperature gradients could also enable effective drift control of bacteria-driven microrobots; thermotaxis is expected to bear the same physical driving mechanisms that we have found in the pH-taxis and chemotaxis of bacteria-driven microrobots. To apply bacteria-driven microrobots for applications in bioengineering and medicine, reliable and efficient control of them at the swarm scale is a critical step. Our demonstrations of robust drift control using pH gradients expand the current scope of the motion control methods of bacteria-driven microrobots. The availability of a pH gradient or ease of deploying a gradient in the workspace will highly depend on the specific application. This study suggests the potential feasibility of applying pH-taxis, chemotaxis, and thermotaxis as motion control methods of bacteria-driven microrobots, and from which an appropriate method can be chosen based on the specific application.

4.6.2 Summary

In this chapter, we have characterized the pH-taxis in a prototype of bacteria-driven microrobots, which concludes that bacterial pH-taxis can be used an effective drift control means for properly designed bacteria-driven microrobots. In the three-channel concentration gradient generator we created and qualitatively calibrated three different pH gradients, which can induce two types of tactic behaviors on free swimming bacteria: (a) unidirectional pH-tactic behavior

away from more acidic pH or away form more alkaline pH, and (b) bidirectional pH-tactic behavior away from both higher and lower pH regions. Subsequently, we demonstrated that the bacteria-driven microrobots also exhibited both unidirectional and bidirectional pH-tactic behaviors, and the associated tactic drifting processes was quantified; in the case of unidirectional pH-taxis, the microrobotic swarm maintains an approximately constant drift velocity when free from wall effects. To understand the physical mechanism of pH-taxis in the bacteria-driven microrobots, thousands of the swimming trajectories of the microrobots were tracked by a visual tracking program. Based on the trajectory analysis, we have found that the swimming heading bias and the speed bias are two factors which contribute to their tactic drift motion, where the heading bias is dominant over the speed bias. The trajectory analysis also shows that the swimming direction of a microrobot is found to be more persistent when it moves towards favored pH regions, which is the cause of the observed heading bias. Furthermore, the pH-taxis is found to be enhanced on faster microrobots; this trend is also followed by the chemotaxis of bacteria-driven microrobots. Finally, the resemblance of the physical mechanism between the pH-taxis and chemotaxis of the bacteria-driven microrobots corroborates that a similar signaling pathway is shared between bacterial chemotaxis and pH-taxis. By demonstrating the pH-taxis of bacteria-driven microrobots and identifying the physical mechanism that drives the pH-tactic motion, this chapter opens up an new avenue towards improving the control of such biohybrid microrobots.

Chapter 5

Modeling Bacteria-Driven Microrobots

5.1 Introduction

Onboard micron-scale actuation and powering has been remained a grand challenge for the miniaturization of active devices down to scales of a few microns. However, nature has its own solutions since billions of years ago: flagellated swimming bacteria can efficiently convert chemical energy into mechanical actuation with their nanoscale biomotors. Over the past decade, numerous studies have been conducted on harnessing flagellated bacteria, such as *E. coli* and *S. marcescens*, as propellers for biohybrid microrobots [22, 24, 27, 28, 29, 30, 31, 32, 33, 34, 35, 36, 37, 52, 58, 62, 118], aiming to solve the pressing engineering problems like targeted drug delivery for tumor therapy [36, 37, 119, 120]. Recently, efforts have also been made to guide the motion of such bacteria-driven microrobots through taxis-based [36, 48, 49, 50, 51, 52, 56, 57] and magnetic steering [37, 46] approaches. Among these studies, the most common way to integrate bacteria into biohybrid microrobots is attaching intact bacterial cells onto the surfaces of synthetic microstructures, such as polystyrene beads, where the attachment could be enabled either by physical attraction [24] or through chemical bonding [36]. Current bacteria-driven microrobots vary vastly in materials, body shape and size, and bacterial attachment configurations; choices of these design parameters, however, have been

mostly based on human intuition and empirical observation, lacking a systematic method to optimize the design of such biohybrid microsystems with respect to the their performance indicators, such as motility and guidability. To this end, it is essential to develop an analytical model that can describe the motion of bacteria-driven microrobots by incorporating critical design parameters, bacterial propulsion mechanics, and common guiding mechanisms such as chemotaxis.

In fluid media, free-swimming peritrichous flagellated bacteria like *E. coli* propel themselves through a combination of running states, during which the flagella form a bundle rotating counterclockwise (CCW) and propel the cell body straight forward, and tumble states, during which the flagella fall apart by clockwise (CW) rotation and the cell body is randomly reoriented. Three-dimensional (3D) tracking results of bacterial swimming motion indicate that their speed during the running states is nearly constant, but it drops significantly or almost to zero during the tumble states [66]. Following from the linear force-speed relation characterized by Stoke's law, we can conclude that the propulsive force of the running states is approximately constant, while the propulsive force is relatively negligible during the tumble states. Apart from the translational motion resulted from the propulsive force, the bacterial cell body also rotates due to a reaction torque, and the rotation frequency is measured to be around 20 Hz for *E. coli* [121, 122]. The kinematic and dynamic quantities related to free-swimming bacteria propulsion can be measured through visual tracking methods [121] and optical tweezers [122]. Although the free-swimming propulsion of flagellated bacteria is well characterized, less is known about how the attached bacteria exert forces and torques on biohybrid systems, such as bacteria-driven microrobots. Recently, helical-shaped trajectories have been observed for bacteria-driven microbeads, each with only one or few bacteria attached [34], which suggests that the microbeads were propelled by near-constant forces and torques during the helical trajectory segments. Two simple stochastic models have been proposed to simulate the swimming motion of spheres propelled by bacteria [53, 123]; however, these models fail to capture the helical motion observed

experimentally, possibly due to oversimplified construction of the model.

Bacteria are generally sensitive to various environmental conditions, including chemoattractant/repellant, pH, oxygen level, temperature, and light. Some cues, such as spatial chemoattractant gradient, can elicit strong biased motion in bacteria, called taxis behavior, e.g., chemotaxis. Such natural sensing abilities of bacteria are considered to be ideal guiding mechanisms for the motion of biohybrid microsystems, especially for healthcare applications in the human body, where chemical cues are ubiquitous. Thus far, the taxis-based guiding method constitutes the major way to regulate the otherwise highly stochastic motion of bacteria-driven microrobots, which has been studied both *in vitro* [48, 49, 50, 51, 52, 56, 57] and *in vivo* [36, 37]. Chemotaxis, one of the most common taxis behavior in bacteria, has been well understood [124] and its signaling pathway has been mathematically modeled [79, 81, 84, 85, 86, 91, 94]. In general, the chemotaxis of free-swimming bacteria associates with a biased random walk, enabled by preferentially suppressed tumble tendency when the bacteria travel up a chemoattractant gradient; whereas in an uniform medium, the tumble tendency is isotropic over all swimming directions. Chemotaxis drift has been observed in bacteria-driven microrobots [48, 49, 50, 51, 52, 56], which typically consist of a spherical particle with multiple bacteria attached at random positions and orientations. Since the chemotaxis of bacteria-driven microrobots involves multiple bacteria whose cell bodies are interconnected through their commonly attached particle, this behavior is featured with some collective characteristics. As a result, despite the well-established mechanisms of bacterial chemotaxis, the chemotaxis of bacteria-driven microrobots can hardly be readily explained.

In this chapter, to shed more light on the bacterial propulsion and the chemotaxis in bacteria-driven microrobots, we propose a model to simulate the 3D motion of a multiple bacteria-driven microrobot system. The whole system is modeled though a combination of two subsystems: (a) multi-bacterial propulsion and microrobot swimming dynamics, and (b) bacterial chemosensing and flagellar rotation dynamics. For model validation, the results of model simulations

are compared to the experimental characterizations of bacteria-driven microrobots from different aspects: 3D swimming trajectory, motility characteristics, and chemotaxis. The simulation of the model indicates that the collective chemotaxis of the multiple bacteria attached to a microrobot could be due to the synchronized kinase activity among these bacteria as a result of their close spatial proximity. Furthermore, we use this model to study the critical parameters that affects the performance of bacteria-driven microrobots, serving as the first step towards the optimized design of bacteria-driven microrobots for specific application objectives.

5.2 Biophysical Models for Bacteria-Driven Microrobots

In general, the model treats each bacterium attached to a microrobot as a two-state machine, and describes the whole system with two subsystem models: the multi-cellular propulsion model and the bacterial chemotaxis signaling pathway model. The multi-cellular propulsion model describes how the attached bacteria exert forces and torques on a microrobot and how the microrobot swims in a fluid medium given its instantaneous propulsion force and torque. The bacterial signaling pathway model outlines the state transition dynamics of a bacterium in response to its local chemical concentration changes over time. Details of these two models are described in the following subsections.

5.2.1 Multi-cellular Propulsion Model

Most of the studies on bacteria-driven microrobots adopt a similar design, which is a sphere-shaped microobject driven by single or multiple flagellated bacteria attached to the sphere in random locations and orientations [24, 29, 32, 34, 35, 36, 48, 49, 50, 51, 52, 56, 57, 62]. This particular design is chosen for its easier fabrication, characterization, and analysis, and also isotropic physical properties, such as drag coefficient, in all orientations. Therefore, we focus on modeling and experimental validation of such design of bacteria-driven microrobots in this

study.

To simplify the system, we only consider the case that bacteria attached to the sphere are fully fixed (no position and orientation change) on the surface and perform rigid body translation and rotation with the sphere. Indeed, this condition is usually satisfied in practice by using relatively strong binding mechanisms, such as covalent and biotin-streptavidin binding. Scanning electron microscope (SEM) imaging (Fig. 5.1(a)) shows that bacteria typically attach to sphere surfaces on their sides or with a small tilt angle, but other than that, the attachment orientation of bacteria is purely random. Flagella morphology is another important consideration in the bacterial propulsion model, because it determines the propelling forces exerted on the microrobot. A video published by Carlsen et al. [46] indicates a bundling behavior of flagella over the bacterial propulsion of a 6μm diameter bead. In addition, through analysis of 3D swimming trajectories, Edwards et al. reported a near-constant propulsive force on the microsimmers, consisting of a 5μm diameter bead attached by a single *S. marcescens* bacterium [34], which suggests that the attached bacterium could be running over that period. Although the bacterial flagella could have more complicated morphologies over bacterial propulsion, based on the available observations, we conjecture that a "bundle-and-unbundle" dynamics, corresponding to the bacterial "run-and-tumble" motility, could still be the dominant flagellar morphology transition pattern. Following from this assumption, the attached bacteria can be modeled as a finite state machine with two states, running and tumbling, and the transition between these two states are determined by their chemical signaling pathway, discussed in the next subsection. The force and torques exerted by a bacterium on the sphere is state dependent, as illustrated in Fig. 5.1(b); the total propulsive force and torques on the sphere are the summed contributions of all attached bacteria under their current states (run or tumble). Furthermore, we adopted a relatively stiff flagella (bundle) models: each flagellar bundle has a predefined orientation but a stochastic oscillation is allowed around the predefined orientation, which tends to represent the experimental observations [46]. However, except for introducing some white noise to simulate

the stochasticity of the real system, the oscillation consideration does not affect the the model behavior.

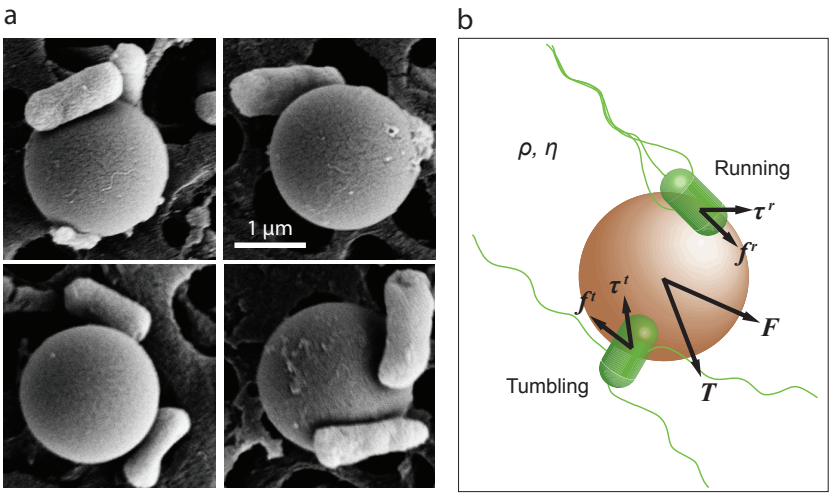

Figure 5.1: Bacteria-driven microrobots with a spherical body. (a) SEM pictures showing 2μm diameter polystyrene microspheres, each attached by a few *E. coli* bacteria. (b) An illustration of the forces and torques exerted on the spherical microrobot body by its attached bacteria, where the force and the motor reaction torque of each bacterium are state dependent.

Below is a summary of the major assumptions of the bacterial multi-cellular propulsion model:

- Attached bacteria maintain their positions and orientations over time and perform rigid body translation and rotation together with the sphere;
- Attached bacteria transition between run and tumble states and exert different forces and torques under different states;
- Interactions between the attached bacteria on a common sphere, if exist, are small and thus negligible for studying the average behavior of the microrobots;
- The swimming motion occurs at low Reynolds numbers and can be approximated by Stokes' law;
- Physical interactions among the microrobots are neglected due to their low concentration in medium.

With these assumptions, the instantaneous propulsive force $\boldsymbol{F}$ and torque $\boldsymbol{T}$ on a microrobot can be described as follows:

$$\boldsymbol{F} = \sum_{s\in\{r,t\}} \sum_{i=1}^{n^s} \frac{\bar{\boldsymbol{f}}_i^s + \tilde{\boldsymbol{f}}_i^s}{||\bar{\boldsymbol{f}}_i^s + \tilde{\boldsymbol{f}}_i^s||} ||\bar{\boldsymbol{f}}_i^s||, \tag{5.1}$$

$$\boldsymbol{T} = \sum_{s\in\{r,t\}} \sum_{i=1}^{n^s} \frac{\bar{\boldsymbol{\tau}}_i^s + \tilde{\boldsymbol{\tau}}_i^s}{||\bar{\boldsymbol{\tau}}_i^s + \tilde{\boldsymbol{\tau}}_i^s||} ||\bar{\boldsymbol{\tau}}_i^s|| + \boldsymbol{r}_i^s \times \frac{\bar{\boldsymbol{f}}_i^s + \tilde{\boldsymbol{f}}_i^s}{||\bar{\boldsymbol{f}}_i^s + \tilde{\boldsymbol{f}}_i^s||} ||\bar{\boldsymbol{f}}_i^s||, \tag{5.2}$$

where s indicates bacterial state, either running (r) or tumble (t), n^s is the number of bacteria currently in state s, $\bar{\boldsymbol{f}}_i^s$ and $\bar{\boldsymbol{\tau}}_i^s$ are the predefined force and torque of the i-th bacteria under state s, respectively, $\tilde{\boldsymbol{f}}_i^s$ and $\tilde{\boldsymbol{\tau}}_i^s$ are the oscillation force and torque of the i-th bacteria under state s, respectively, and r_i is the position vector of the i-th bacteria under state s with respect to the sphere frame. Described in Eq. 5.1, the current force vector of a bacterium is determined by its predefined force $\bar{\boldsymbol{f}}$, where the direction is aligned with the longitude of the cell body, plus a small oscillation component $\tilde{\boldsymbol{f}}$, which is a random vector perpendicular to $\bar{\boldsymbol{f}}$; the magnitude of the current force is regularized to an measure average value, $||\bar{\boldsymbol{f}}||$. The instantaneous resultant propulsive force $\boldsymbol{F}$ on the sphere is computed by summing up the current propelling forces of all of the attached bacteria. The force denotation and modeling rules are also applied to the motor reaction torque $\boldsymbol{\tau}$, as shown in the first term in the summation of Eq. 5.2, where the second term in the summation computes the force-induced toque by the propelling force. Thus, the torque contribution of a bacterium includes two parts, the motor reaction torque and the force-induced torque; summing them over all of the attached bacteria gives the instantaneous driving toque $\boldsymbol{T}$ on the sphere, as described by Eq. 5.2.

Bacteria-driven microrobots typically operate at Reynolds numbers below 10^{-4}, in which inertial effects are neglected and fluid motion is governed by the Stokes equation. Considering the spherical rigid body in our model, instantaneous fluid drag force ($\boldsymbol{F}_{drag}$) and torque ($\boldsymbol{T}_{drag}$) can be expressed in terms of the velocity and the angular velocity of the moving sphere,

respectively, as follows:

$$\boldsymbol{F}_{drag} = -6\pi\eta R\boldsymbol{v}, \tag{5.3}$$

$$\boldsymbol{T}_{drag} = -8\pi\eta R^3\boldsymbol{\omega}, \tag{5.4}$$

where η is the dynamic viscosity of the fluid medium, R indicates the radius of the sphere, and $\boldsymbol{v}$ and $\boldsymbol{\omega}$ are the instantaneous velocity and the angular velocity of the sphere. Because the drag force and torque are always balanced by the propulsive force and torque, respectively, i.e., $\boldsymbol{F} = -\boldsymbol{F}_{drag}$ and $\boldsymbol{T} = -\boldsymbol{T}_{drag}$, we can infer the instantaneous velocity and angular velocity of the sphere from its present propulsive force and torque. At each time step of the model simulation, rigid body translation and rotation are performed for the sphere and the attached bacteria to update their positions and orientations.

5.2.2 Bacterial Signaling Pathway Model

Although bacterial attachment to microrobots could block some of the ligand binding sites of some methyl-accepting chemotaxis proteins (MCP, a transmembrane protein of bacteria for sensing extracellular concentrations of molecules and transducing the signals to intracellular regulators) physically, it is unlikely that their signaling pathway, which occurs mostly inside the cell body, can be significantly affected by the attachment. Therefore, we adopted the chemotaxis signaling pathway models established recently as the basic component of chemical sensing and response for the bacteria attached to microrobots. Details of the signaling pathway models are described as follows.

The chemotaxis signaling pathway of *E. coli* was modeled with three major components, and their corresponding models were adapted from recent studies [79, 81, 84, 85, 86, 91, 94]. The first component, MCP complex, was represented with a Monod-Wyman-Changeux (MWC) model [125] to describe the allosteric effects of receptor clusters with identical receptors. Each MCP complex switches rapidly between active (on) and inactive (off) states, determined by a

free-energy difference F as follows [79, 81, 85]:

$$F(m,[L]) = f_m(m) + \ln\left(1+\frac{[L]}{K_a}\right) - \ln\left(1+\frac{[L]}{K_i}\right), \tag{5.5}$$

where m is the total methylation level of the receptor complex, $[L]$ indicates the ligand concentration, K_a and K_i are the dissociation constants of active and inactive receptors, respectively, and $f_m(m) = \alpha(m_0 - m)$, with $\alpha \approx 1.7$ and $m_0 \approx 1$ [77], is the methylation level-dependent free energy difference. The suggested dissociation constants are $K_a = 3$ mM and $K_i = 18.2$ μM [126] but may be shifted slightly in simulation to match the most sensitive ligand concentration. Hence the receptor kinase activity can be expressed as [81, 85]

$$a = \frac{1}{1+\exp(F(m,[L]))}, \tag{5.6}$$

where N is the number of receptors in a receptor complex ($N = 6$ for *Tar* receptor and $N = 13$ for *Tsr* receptor [100]). The methylation kinetics was described by [86]

$$\frac{\mathrm{d}m}{\mathrm{d}t} = k_R(1-a) - k_B a, \tag{5.7}$$

where K_R and K_B are methylation and demethylation rates of the receptor, respectively; their values were determined by fitting the experimental data on bacterial chemotaxis response. The second component models the signal transduction from kinase activity to the concentration of Che-Y-P, Y_p, and we adopted a linear relationship in our simulation [81, 94], $Y_p = \beta a(t)$. The third component in the signaling pathway deals with the flagellar rotation dynamics in response to Y_p. Enlightened by Sneddon et al. [94], we treated all the flagella of a bacterium as a single stochastic bistable system bearing the transition rates k_+ and k_- to running and tumble state,

respectively, which were modeled as a function of Y_p:

$$k_{\pm} = \omega_0 \exp\Big\{ \pm \Big[\frac{g_0}{4} - \frac{g_1}{2}\Big(\frac{Y_p(t)}{Y_p + K_D}\Big)\Big]\Big\}, \tag{5.8}$$

where the parameter values were $\omega_0 = 1.3\ \mathrm{s}^{-1}$, $g_0 = g_1 = 40\ k_BT$, $K_D = 3.06\ \mu$M [94].

The bacterial chemotaxis signaling pathway model simulates the signal transduction from the local chemical concentration of a bacterium to its flagellar motor rotation response. Bacteria typically sense a wide range of chemical concentration (gradient), spanning a total of $3 \sim 4$ orders of magnitude, by a receptor adapting mechanism. The bacterial flagellar motors can produce biased tendency of rotation in CCW or CW direction, depending on the local chemical concentration changes. The signaling pathway model captures these biophysical behaviors, and the model simulation was compared to the corresponding experimental measurements [94, 100], which served as the benchmark tests of the signaling pathway model. To verify the correctness of our implementation of the model, we performed such benchmark tests, as shown in Fig. 5.2, and which results confirms a correct implementation.

As a summary, the signal flow of the integrated model for bacteria-driven microrobots is depicted in Fig. 5.3.

5.3 Simulation Setup and Experimental Methods

5.3.1 Simulation Setup

The simulated environmental conditions were 20°C in temperature and 1 cP in viscosity, simulating the room temperature and the liquid medium used in experiments, and these conditions were common to all simulations. The boundary condition, however, was different depending on the simulation. For motion study of bacteria-driven microrobots, no boundaries were set, which approximated the far-wall condition of the experimental measurements. In the chemotaxis stud-

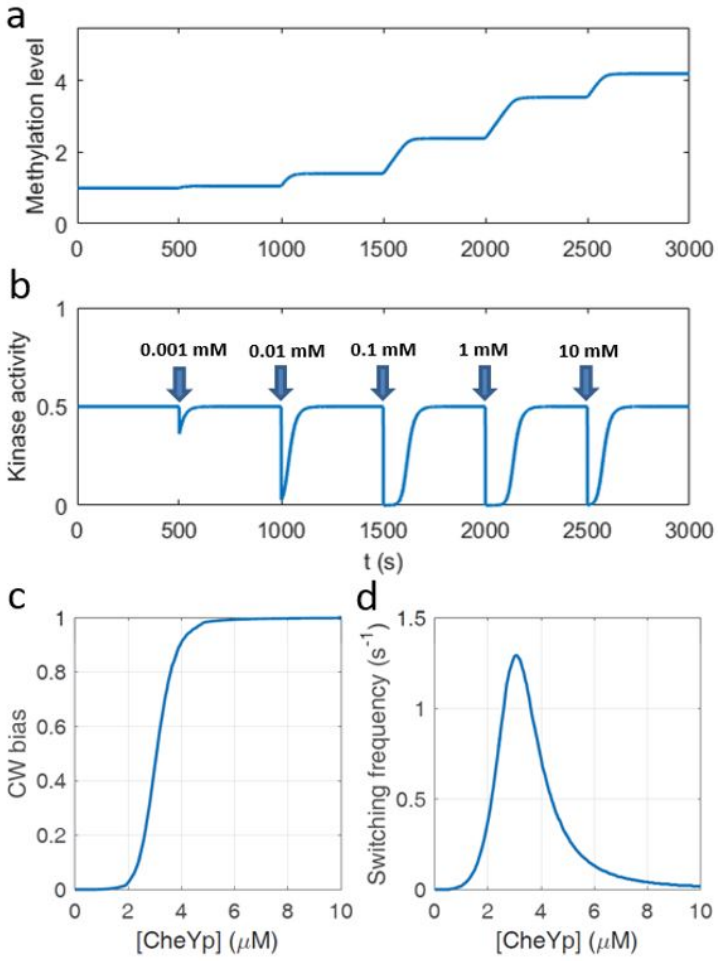

Figure 5.2: Tests of bacterial chemotaxis signaling pathway model. (a) Methylation level adaptation and (b) kinase activity dynamics when a series different environmental concentration were applied over time. (c) Flagellar motor counterclockwise (CW) rotation bias and (d) rotation direction switching frequency as a function of intracellular CheYp concentration.

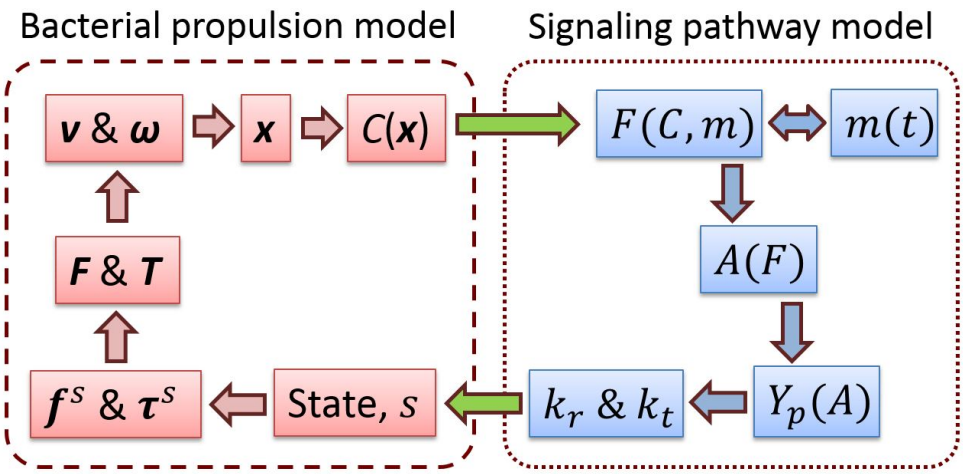

Figure 5.3: Signal flow of the integrated model for bacteria-driven microrobots, including the bacterial propulsion model and the chemotaxis signaling pathway model.

ies of free-swimming bacteria and bacteria-driven microrobots, a bounded environment was simulated to mimic the microfluidic channel in the gradient generator. Specifically, the motion of the simulated agents (bacteria or bacteria-driven microrobots) was constrained in a box with dimensions $x \times y \times z = 500 \times 500 \times 250$ μm^3, where the linear chemoattractant gradient was applied along the x dimension, as shown in Fig. 5.4. Since the experimental measurements were taken far away from the walls perpendicular to the y-axis and z-axis, the wall effect along these two dimensions were simply set to be reflecting the agent's (bacteria or bacteria-driven microrobots) motion upon hitting a wall, as illustrated in Fig. 5.5(a), which avoided affecting the agents' transportation along the x-axis while preserved the total number of agents in the simulated box. The wall effect along the x-axis (the gradient direction) was treated differently between the free-swimming bacteria and bacteria-driven microrobots, based on experimental observations. Once a free-swimming bacterium reached a wall perpendicular to the x-axis, it could be trapped into swimming along the wall for couple seconds [81] before leaving the wall, as depicted in Fig. 5.5. However, the bacteria-driven microrobots would mostly become immobilized if they swim into the x-walls [56], and thus this wall effect was reflected as a permanent trapping in our simulations, as illustrated in Fig. 5.5.

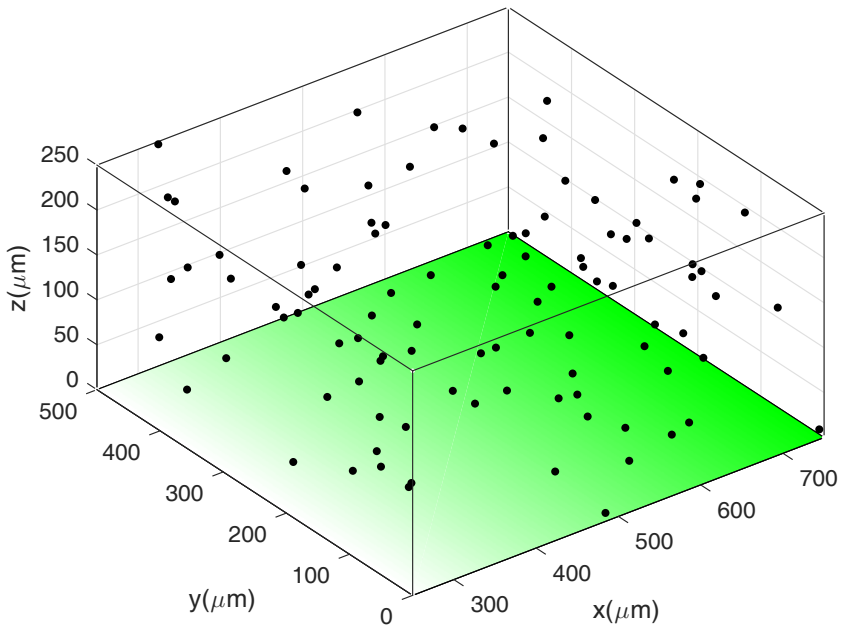

Figure 5.4: The bounded simulation space with a number of randomly distributed simulation agents upon initialization.

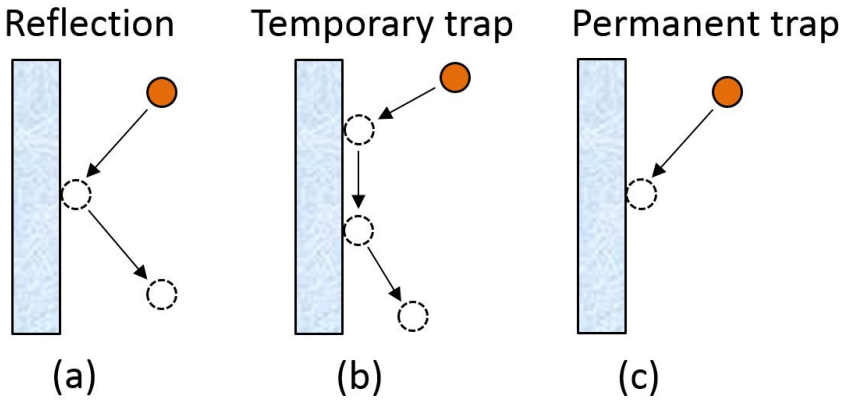

Figure 5.5: Different types of simulated wall effects: (a) reflection, (b) temporary trap, and (c) permanent trap.

A program was developed in Matlab (R2016a, The MathWorks, Inc., Natick, MA, USA) to simulate the proposed models. A simulation was conducted in two steps: initialization and iteration. In the initialization step, a given number of agents were randomly placed within the simulation environment, as shown in Fig. 5.4, and their associated state variables, e.g., signaling pathway states, were initialized according to the statistics of experimental measurements. The iteration step kept updating the position and other state variables of each agent, based on its local chemoattractant concentration input, the agent's swimming dynamics, and the predefined wall effects, until the end of the given simulation duration. Fig. D.1 shows the procedure of the simulation program for bacteria-driven microrobots. Necessary state traces, such as positions and pathway activities, were recorded over the iteration step for further analysis.

5.3.2 Prototyping Bacteria-driven Microrobots

The bacteria-driven microrobots for motion study were fabricated by randomly attaching *E. coli* bacteria to 2.2μm diameter Poly(methyl methacrylate) (PMMA) (PolyAn, Berlin, Germany) spherical particles, where the specific and strong attachment was enabled through biotin-streptavidin bonding. The fabrication process of the microrobots is briefly described as follows. First, 1 ml of the bacterial liquid culture was washed with PBS (centrifuged at 1500 g for 5 min) for a total of 3 cycles, with a final suspension of 1 ml. Then, an aliquot of a biotin conjugated *E. coli* LPS antibody (Thermo Fisher Scientific, Waltham, Massachusetts, USA) was added to the bacterial suspension to reach a dilution of 1:50, followed by an 1 hr incubation of the mixture on a shaker (300 rpm, 30°C). Subsequently, the bacteria-antibody mixture was washed with PBS for 3 cycles to remove the excess, unconjugated antibodies, and the streptavidin functionalized PMMA particles was washed with PBS (centrifuged at 5000 g for 1 min) for 3 cycles to eliminate the surfactant that came with the particles. Finally, the antibody-conjugated bacteria was mixed with the particles at an appropriate density ratio and incubated on a shaker (600 rpm, 30°C) for 30 min to allow for biotin-streptavidin interactions between the bacteria and

particles. To enhance motility, the assembled bacteria-driven microrobots were suspended in a motility medium (0.01 M KH_2PO_4, 0.067 M NaCl, 10^{-4} M EDTA, 0.01 M glucose, pH = 7.0) for experimental observations.

5.3.3 Imaging and Visual Tracking

Two optical systems, an inverted microscope (Zeiss Axio Observer A1, Oberkochen, Germany) and a digital holographic microscope (DHM T-1000, Lyncée Tec SA, Lausanne, Switzerland), were applied to study the chemotaxis of free-swimming bacteria and the 3D motion of bacteria-driven microrobots, respectively. The distribution of bacteria in the sample channel of the gradient generator was observed using a 20x (NA 0.50) objective, and phase contrast images were acquired and analyzed using an in house program developed in Matlab (R2016a, The MathWorks, Inc., Natick, MA, USA). The holograms of the bacteria-driven microrobots were observed using a 40x (NA 0.75) objective, which gives a 2D field of view around 165×165 μm^2. The numerical reconstruction was conducted by a commercial software (Koala, Lyncée Tec) to obtain the $z-$stacked images of the view volume, which was $110 \times 110 \times 110$ μm^3 with a chosen z-range of 110 μm. Further, the reconstructed image stacks were analyzed by an in-house program developed in Python 2.7 to detect the 3D positions of the bacteria-driven microrobots in the view volume and perform 3D motion tracking. The 3D positioning and tracking algorithms used in this program is included in Appendix C.

5.4 Model Calibration and Validation

We first calibrated and validated the bacterial chemotaxis model and the bacterial propulsion model separately. Then the two models were combined to simulate the chemotaxis in bacteria-driven microrobots, which results were compared to the experimental characterizations from our previous study.

5.4.1 Chemotaxis of Free-Swimming Bacteria

Before integrating the chemotaxis signaling pathway model with the bacterial propulsion model to simulate the motion and the chemotaxis of bacteria-driven microrobots, we studied the chemotaxis response of free-swimming bacteria via both simulations and experiments, to verify the model and to estimate the model parameters.

The chemotaxis response of free-swimming *E. coli* bacteria was tested in a three-channel concentration gradient generator [70, 71], which has been widely used to characterize bacterial chemotaxis. The device generates a one-dimensional (1D) stable linear gradient in a quiescent microfluidic channel, featuring a minimum yet controllable condition for observing bacterial chemotactic drift. Our previous study shows that the bacterial distribution in the test channel can reach a steady state [54], resulting from a balance between bacterial random diffusion and chemotactic drift. Here, we characterized the steady-state distribution of *E. coli* against different magnitudes of linear L-aspartate gradients, in a quantity called "chemotaxis migration coefficient (CMC)" [70], which quantifies how the distribution is biased along the gradient. CMC is defined as CMC $= \sum_i (x_i - x_0)/w$, where x_i indicates the position of the i-th bacteria along the direction of interest (i.e., the gradient direction), x_0 is a reference position, usually defined to be the middle of the channel, and w is the width of the channel. Fig. 5.6(a) is an example image showing the biased distribution of bacteria under a gradient of 0.1 mM/mm along the vertical direction. For each experimental data point showed in Fig. 5.7, we computed the CMC based on hundreds of such distribution images, and multiple samples were analyzed to obtain the averages and the standard deviations. Side by side, the simulation results of biased bacterial distribution and chemotactic response are presented in Figs. 5.6(b) and 5.6(c), respectively (details about the simulation conditions are explained in Section 5.3.1). The inset in Fig. 5.7 traces the dynamic transition of the simulated bacterial distribution before it reaches a steady state, as shaded in yellow; the CMC data in Fig. 5.7 were calculated based on steady-state distributions. In the simulated pathway model, the methylation and demethylation rates $K_R = K_B = 0.008$

s^{-1}, as model parameters [81], were determined by creating the best fit of the simulation to the experimental data over the entire range of gradients. From the close match displayed between the model simulation and the experimental result, we can conclude that the fitted model is able to describe the chemotaxis response of the studied bacterial type towards L-aspartate.

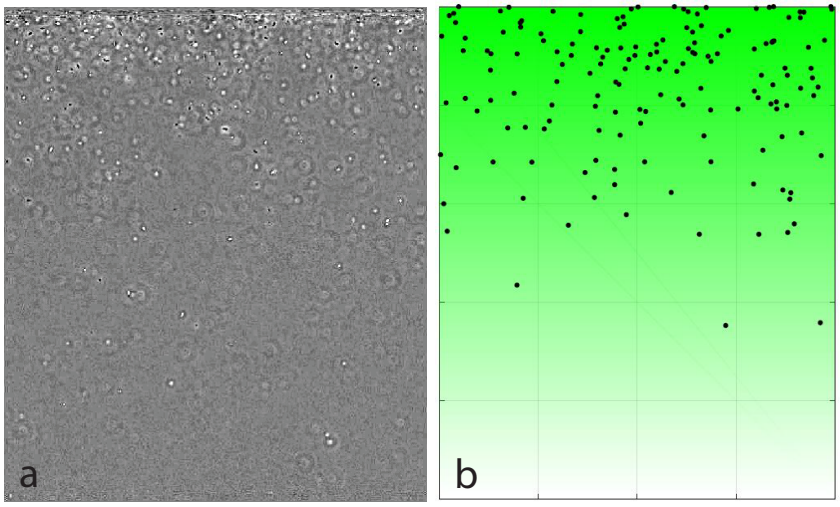

Figure 5.6: Bacterial chemotaxis in a bounded channel with a linear attractant gradient. (a) Steady-state distribution of *E. coli* under a linear concentration gradient of L-aspartate, where the white and black blobs indicate bacterial cell bodies. The linear gradient is 0.1 mM/mm and is along the vertical direction of the image, with the top having a higher concentration. (b) Simulated steady-state distribution of bacteria under the same gradient condition (i.e., *E. coli* against 0.1 mM/mm L-aspartate), where the black dots indicates bacteria and the color profile represents the concentration gradient field.

5.4.2 3D Motion of Bacteria-driven Microrobots

3D swimming trajectories of microrobots driven by a small number of bacteria were studied to validate the proposed multi-cellular propulsion model. The microrobots were fabricated by randomly attaching *E. coli* bacteria to 2.2μm diameter PMMA microspheres, each of which had one to three bacteria attached, observed from SEM images. The 3D motion of the microrobots were observed and visually tracked using a digital holographic microscopy (DHM) system. A total of 87 trajectories were collected, and 10 sample trajectories are plotted in Figs. 5.8(a)

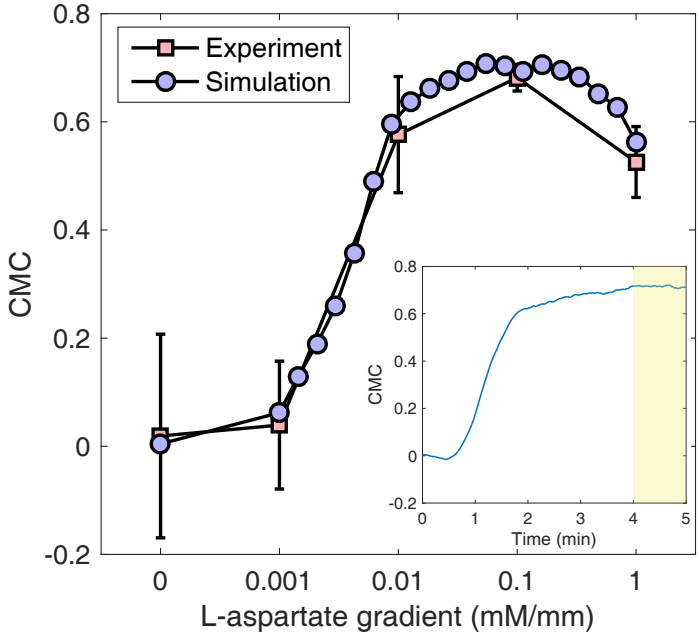

Figure 5.7: Bacterial chemotaxis response, measured in CMC, over different magnitudes of linear L-aspartate gradients. The inset plot shows a typical CMC dynamics during simulation, and the chemotaxis response (CMC) was measured from the yellow-shaded region, where a steady-state distribution was formed.

and 5.8(b), in 3D and 2D, respectively; the trajectory length varies from 4 to 40 seconds. As can be seen from the plots, one prominent shape of the trajectories is helical or near-helical, similar to what has been reported by Edwards et al. [34] on 5μm diameter beads propelled by *S. marcescens* bacteria. A basic free body diagram of the system indicates that, while tracing helices, the propulsion dynamics of the microrobots is dominated by a near-constant force and a near-constant torque which are not colinear. As another important characteristic of the trajectories, there are apparent interruptions between the consistent helices, which provide drastic reorientations for the helices; this phenomenon resembles the tumbling behavior of free-swimming bacteria. The sudden divergence from a previous helical orientation is due to changes in the exerted force and torque, and presumably, it is the flagellar morphological transformation that causes the propulsion changes. Enlightened by this observation, our model indeed incorporates a mechanism that allows changes in the propulsive force and torques ex-

erted by a bacterium upon its state transition. For the running state, the average propulsive force $||\bar{\boldsymbol{f}}||$ and motor reaction torque $||\bar{\boldsymbol{\tau}}||$ were estimated from the stable helical trajectories produced by single bacteria-driven microrobots [34], using the instantaneous speed and the approximated period of a helix, as illustrated in Fig. 5.9. In the tumble state, the average propulsive force was set to zero, considering the near-zero translation during bacterial tumble, and the average motor reaction torque was reduced by a factor based on the difference of flagellar rotational frequency [121]. The average propulsive force and motor reaction torque used in our simulation are summarized in Table 5.1. The magnitudes of the oscillation components in Eqs. 5.1 and 5.2 are set to be about 10% of the corresponding predefined components to mimic the system uncertainties.

Table 5.1: Average propulsive force and torque

Parameter	Symbol	Value
Average force on run	$\|\|\bar{\boldsymbol{f}}^r\|\|$	0.3 pN
Average motor reaction torque on run	$\|\|\bar{\boldsymbol{\tau}}^r\|\|$	0.7 pN·μm
Average force on tumble	$\|\|\bar{\boldsymbol{f}}^t\|\|$	0 pN [66]
Average motor reaction torque on tumble	$\|\|\bar{\boldsymbol{\tau}}^t\|\|$	0.4 pN·μm [121]

We simulated the model with conditions similar to those of experiments, and compared the trajectory pattern/shape and the motility characteristics, including the mean squared displacement (MSD) and tumble angle, between simulations and experiments to validate the propulsion model. Figs. 5.10(a) and 5.10(b) present 10 simulated sample trajectories in 3D and 2D, respectively, whose length is about 15 seconds, matching the average length of the experimentally captured trajectories. Clearly, the model reproduces the helical pattern that are generally observed along the trajectories from experiments, and the simulated helices morphologically resemble the measured ones in terms of the pitch and size of helix turns.

Considering the likely random reorientations occurred among the helical tracks, motility of the microrobots was studied using MSD, the most common motion measurement for random walk systems. As shown in Fig. 5.11, the MSD is examined within two different regimes, bal-

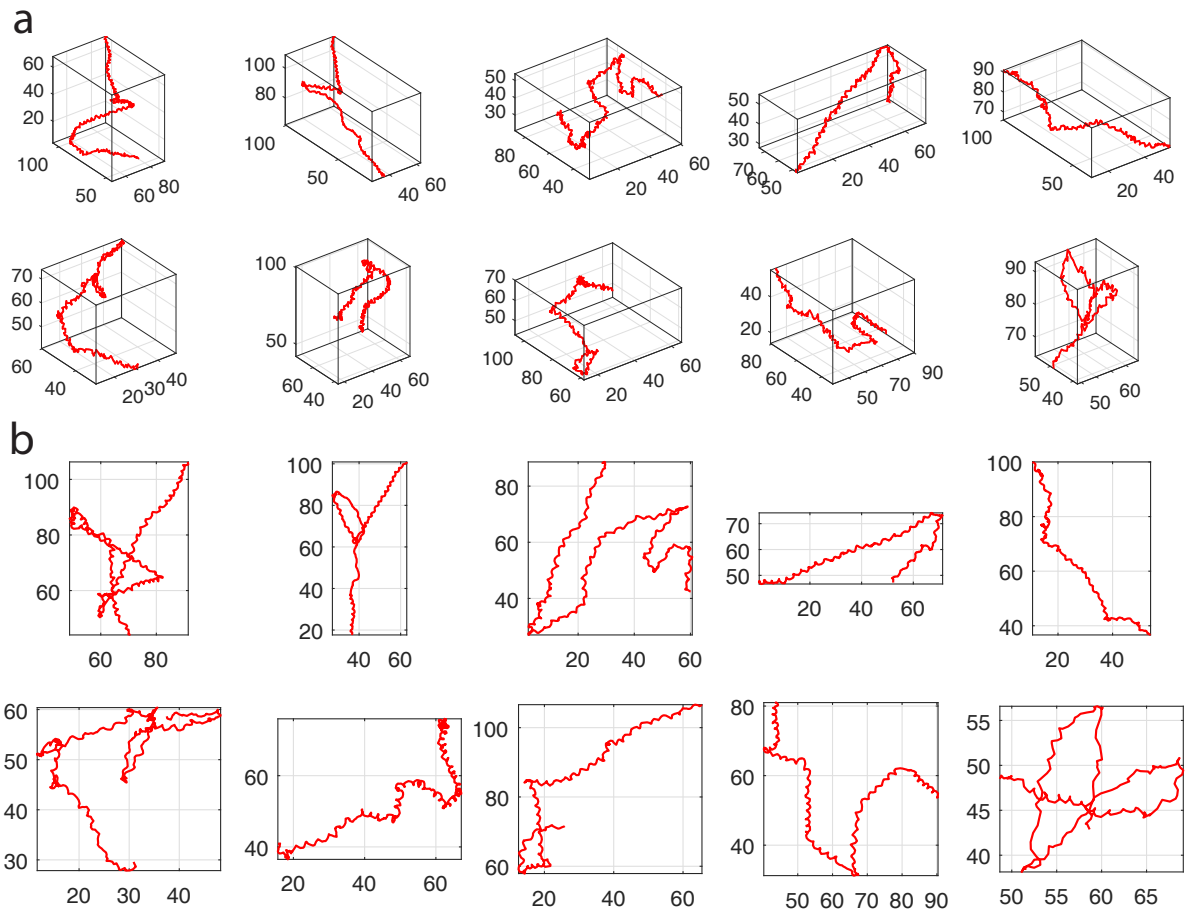

Figure 5.8: Motion of microrobots propelled by a few attached bacteria (experiment). 3D trajectories (a) and their xy-plane (2D) projections (b) of 10 example microrobots.

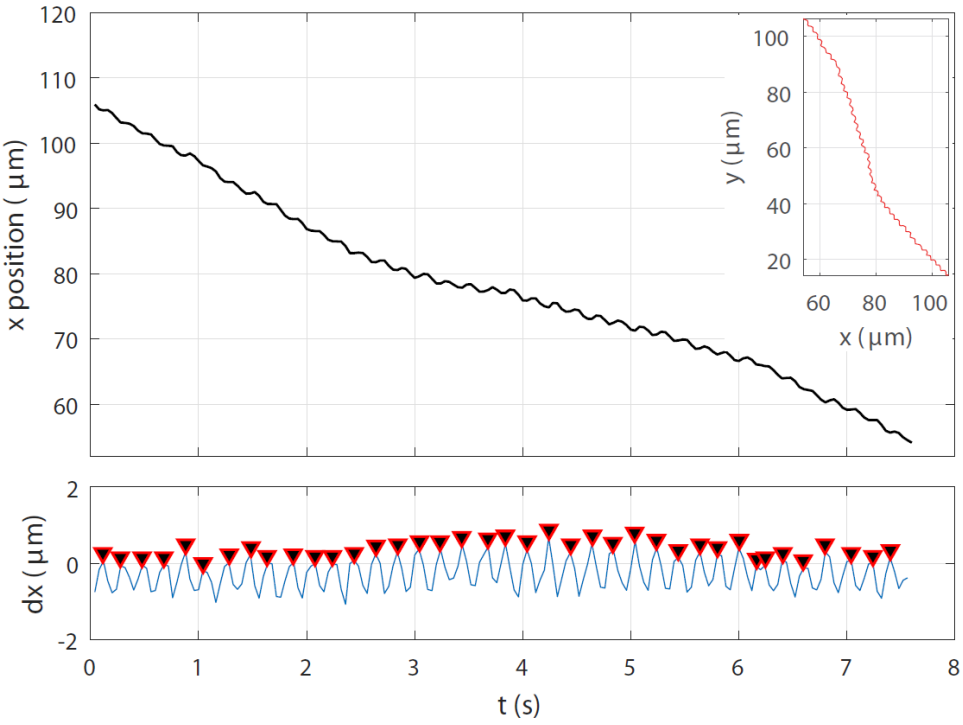

Figure 5.9: Illustration of angular velocity evaluation from the 2D projection of a helical trajectory. (a) x-position over time, where the inset shows the 2D projection. (b) Count number of helical turns using periodicity along dx.

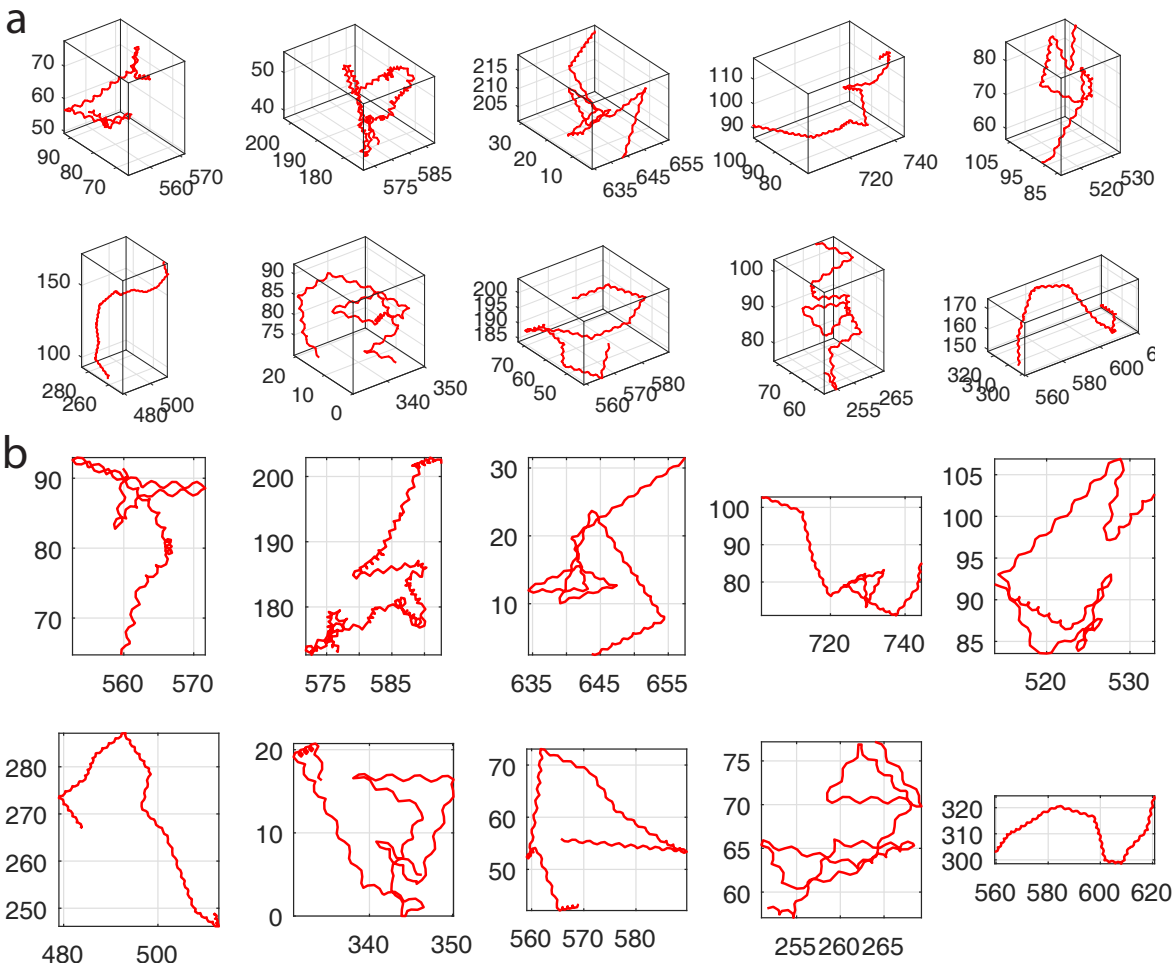

Figure 5.10: Motion of microrobots propelled by a few attached bacteria (simulation). 3D trajectories (a) and their xy-plane (2D) projections (b) of 10 example microrobots.

listic and diffusive regimes, which are determined by a characteristic time $\tau_R = 1.5$ s, estimated through fitting the MSD formula to the experimental data [127]. Manifested by the quadratic shape of the MSD plots at short time intervals (considerably shorter that τ_R), as shown in Figs. 5.11(a) and 5.11(c), the microrobots exhibit ballistic behavior, and the fitted mean speed of the simulation, $v_{\text{mean}} = 9.9$ μm/s, approximates that of the experiment, 10.9 μm/s. The MSD over larger time intervals (considerably longer than that τ_R) traces a linear profile, as shown in Figs. 5.11(b) and 5.11(d), revealing a diffusive motility of the swimming motion over long time scales. The effective diffusion coefficients drawn from line fittings are 30.1 μm^2/s for simulation and 22.4 μm^2/s for experiment; the lower experimental value is caused by the fact that the faster microrobots are hard to track for a long time, as shown in Fig. 5.11(d), and thus biasing the measurement towards slower instances.

Besides, it has been shown that the random diffusivity of the "run-and-tumble" type of random walk strongly depends on the reorientation angle following a tumble event [68]. Thus, we analyzed the helical reorientation angle of the swimming trajectories, as demonstrated with a sample trajectory in Fig. 5.12(a). Fig. 5.12 shows the probability distributions of the reorientation angle, where the simulation closely matches the experiment and both of them appear to follow a normal distribution, with a most probable value around 80 degrees. The comparable trajectory and matched motility characterizations imply that the propulsion model captures the fundamental mechanisms associated with the physical system of multi-bacteria driven microrobots.

5.4.3 Chemotaxis of Bacteria-Driven Microrobots

By assuming that the individual bacteria attached to a microrobot sense their own local chemical concentrations and perform signal transduction independently, we propose an integrated model for the chemotaxis of multi-bacteria driven microrobots, which combines the multi-cellular propulsion model and the bacterial chemotaxis pathway model. All of the model parameters

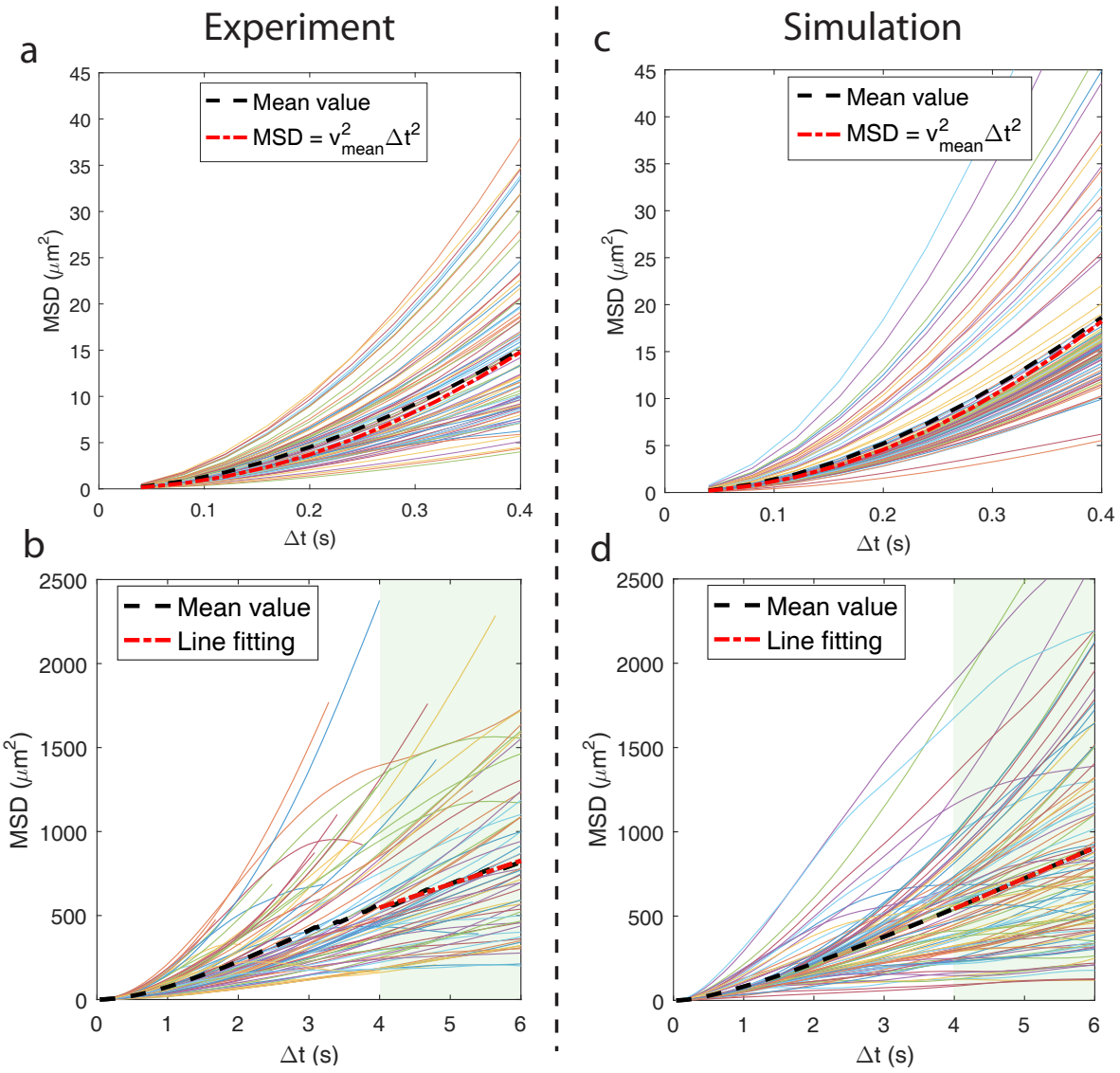

Figure 5.11: MSD of bacteria-driven microrobots attached by a few bacteria. (a) 3D MSD plots of all the experimentally collected tracks and swimming speed fitted in the ballistic regime. (b) 3D MSD plot and random motility estimation by line fitting in the diffusive regime (green shaded). (c) and (d) show the corresponding results from the model simulations.

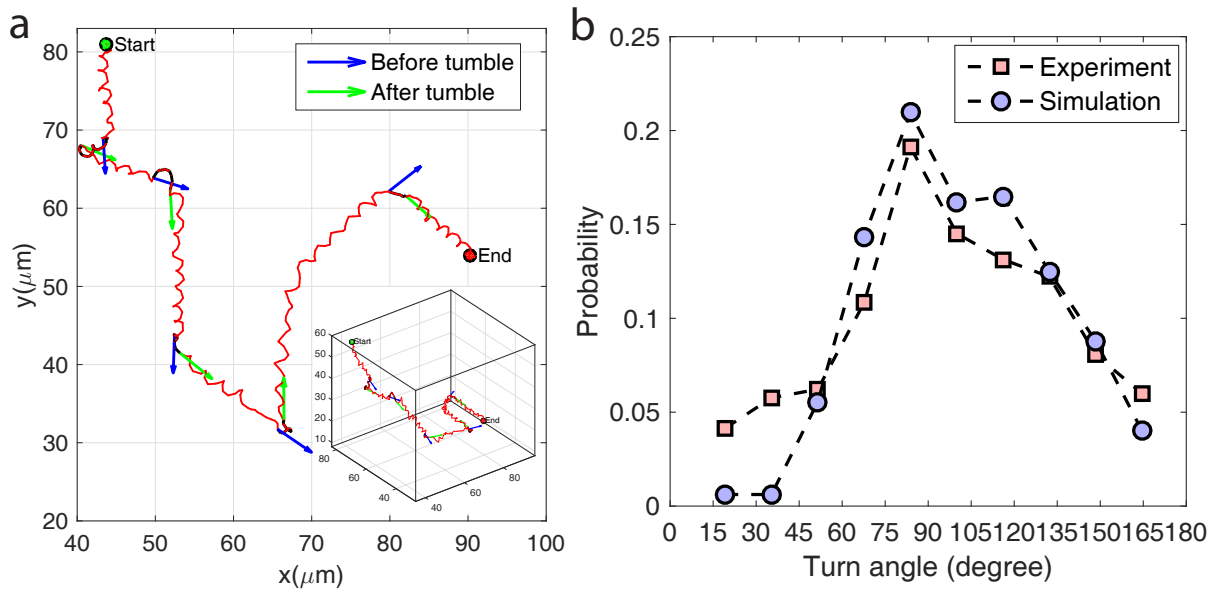

Figure 5.12: Tumble reorientation angle of bacteria-driven microrobots. (a) A sample trajectory with five tumbles detected, and the orientations before (blue) and after (green) each tumble are marked with arrows. (b) A comparison of probability distribution of tumble angles between experiment and simulation, where the most probable tumble angle lies around 80 degrees. About 90 trajectories were assessed in both experiment and simulation.

were derived from the chemotaxis of free-swimming bacteria and bacteria-driven microrobots under isotropic conditions. The model was simulated and qualitatively validated via comparisons with the chemotaxis experiment data from our previous study [56]. Specifically, we considered the situation of randomly placing a swarm of microrobots in a bounded channel holding a linear attractant concentration gradient and observing how their distribution changed over time, mainly along the direction of interest (i.e., along the gradient).

Figs. 5.13(a) and 5.13(b) show the drifting dynamics of a swarm of microrobots from simulation and experiment, respectively, where the microrobots are made of 3μm diameter spheres driven by 6-12 attached bacteria. Although the two quantities, CMC and COM-y (the y-component of center of mass, computed as the mean y-position of all microrobots in the field of view), are defined differently, they are all linear functions of the microrobots' positions, and thus linearly related to each other. Both results show that, starting with a nearly uniform distribution, the swarm undergoes an approximately linear drifting process, associated with a constant chemotactic drift velocity, and eventually it settles down to a biased distribution, in which the microrobots are more concentrated on the side with a higher concentration of the attractant. Note that such a final distribution is formed because the gradient is bounded by walls, which constrain the motion of the microrobots. The simulated drifting process, however, appears to be faster than the experimental one, reaching a steady state distribution after 4 min as compared to 8 min for experiment; this could be resulted from the fact that, compared with a simulated ideal system, the experimental system of microrobots bears various imperfections, such as the existence of non-motile instances and the aggregations of microrobots. The analysis on the simulated trajectories suggests that the swimming direction of a microrobot is more persistent when it travels up the gradient than when it moves reversely, and this is consistent with experimental observations [56, 57]. When projected onto one axis, such biased motion can be quantified by the "relative reversing rate bias" [57], defining the bias in the direction reversing rate over the heading of an object performing an 1D random walk; the quantity contributes to

the chemotactic drift velocity as a linear factor [72]. As shown in Fig. 5.14, the simulation and experiment agree that the relative reversing rate bias increases with the mean speed, which in further means that the chemotactic drift velocity is enhanced on faster microrobots.

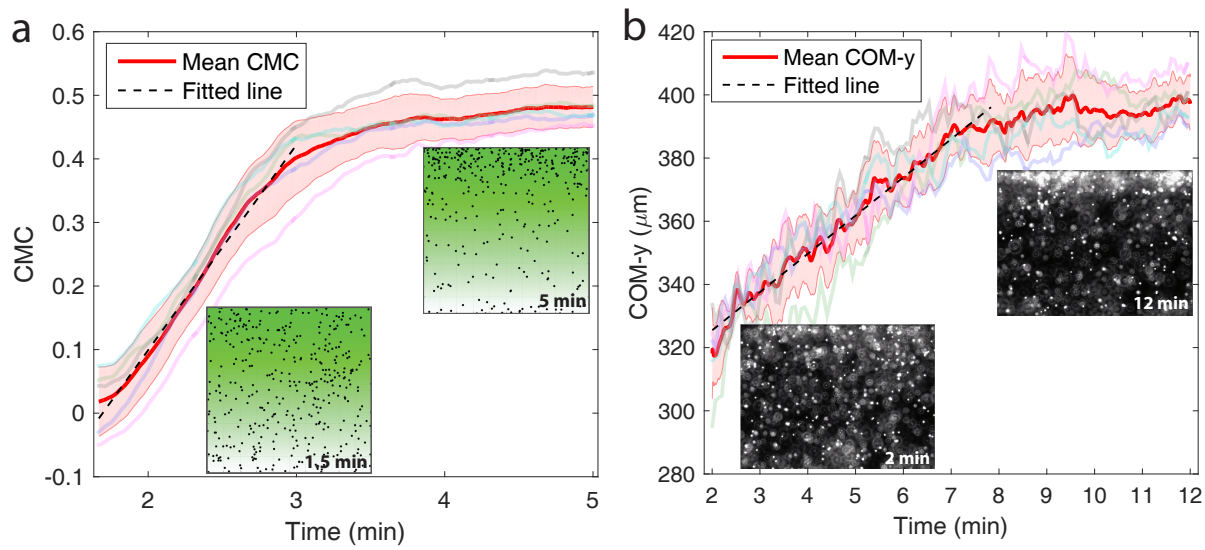

Figure 5.13: Chemotaxis of multi-bacteria driven microrobots. (a) The drifting dynamics (quantified in CMC) of a swarm of simulated microrobots in a channel with a linear attractant gradient. The mean CMC is assessed from five independent samples, and the red shading represents their standard deviation. The two insets show the distribution profile of the microrobots at 1.5 min, when they are randomly located, and 5 min, when the distribution is biased towards the side with a higher attractant concentration. (b) Experimental measurement of the drifting process of a swarm of microrobots propelled by *S. marcescens* bacteria, where the quantity COM-y indicates y component of the center-of-mass. The two insets are fluorescent images representing the distribution profile of the microrobots at 2 min (initial stage) and 12 min (final stage). This figure is reprinted from [56].

Although the chemotactic drift of bacteria-driven microrobots can be phenomenologically explained by the heading persistence bias, it is not readily understandable why the multiple bacteria attached to a microrobot in random orientations can perform chemotaxis in a seemingly cooperative fashion. However, our model, which successfully traces the chemotaxis of the microrobots, rules out any explicit chemical or physical interactions among the attached bacteria on a microrobot. But the group of physically interlocked bacteria must have an implicit avenue to "agree" with each other in order to perform chemotaxis, because the otherwise ran-

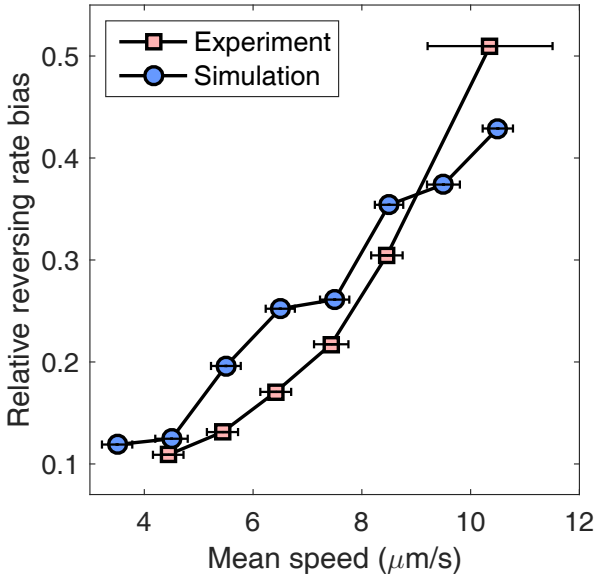

Figure 5.14: Dependence of the relative direction reversing rate bias of the microrobots on their swimming speed.

dom competition among them would lead to a pure random walk in the microrobot. Since the integrated model is supposed to explicitly account the essential biophysical components of the multi-bacteria driven system, all of the states of each involved bacterium is observable throughout a simulation, and thus we can identify the functioning mechanism that enables them to agree on chemotaxis. A quick conjecture is that such consensus is implicitly obtained through their mechanical bonding, by attaching to a common microsphere. To prove this, we plotted the MCP kinase activity dynamics of the bacteria attached to a microrobot, and eight different microrobots were examined and displayed in Fig. 5.15. Interestingly, despite their independent signaling pathway, the kinase activities of the group of bacteria attached to a common microsphere are highly synchronized, and such synchronization tends to produce a downstream run-and-tumble synchronization among these bacteria. Based on the nature of the signaling pathway model, the synchronization must be produced by a similar concentration input trace for the group of bacteria, which is indeed guaranteed as they are interlocked in close proximity to each other by the microsphere. It is highly possible that the synchronization of signaling

pathways, which explains the chemotaxis in our model, could be the reason for the chemotaxis in the experimental system, given the biophysical formulation of the model and the high level resemblance between the model simulation and experiment.

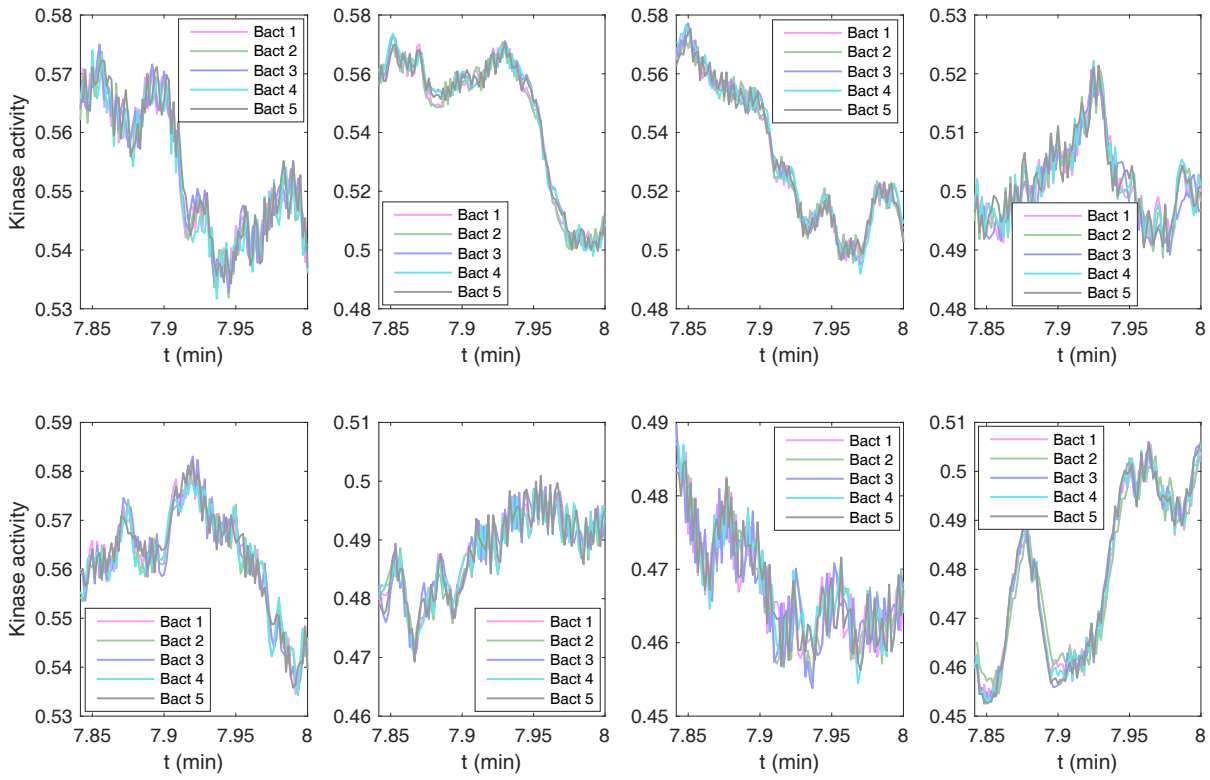

Figure 5.15: Synchronized MCP kinase activity of the multiple bacteria attached to a microrobot (simulation). Eight different microrobots are presented, where each microrobot has five bacteria attached randomly in both position and orientation.

5.5 Parameter Studies

The development of bacteria-driven microrobots has been based on experimental intuition thus far, and the dependencies of microrobots' performance on system parameters has not been addressed before, leaving the design optimization of of the biohybrid system challenging. Here, we propose an approach to optimize the design of bacteria-driven microrobots through model-based simulation. Chemotactic guidability and motility are the two most important consider-

ations for the application of the bacteria-driven microrobots; therefore, focusing on these two performance indicators, we studied their dependencies on certain system parameters that could be easily configured in experiment. Fig. 5.16 shows the chemotaxis response of microrobots over different attractant concentration gradients, which has a profile very similar to that of free-swimming bacteria (Fig. 5.7(c)), and the optimal concentration gradient for chemotactic guidance is around 0.1 mM/mm. However, for the microrobots that are significantly slower than free-swimming bacteria, we expect their strongest chemotaxis occurs at a higher concentration gradient (see Discussions). The dependencies of chemotaxis and speed on the size of microrobots is presented in Fig. 5.17(a), where the number of bacteria attached to a microsphere is proportional to its surface area and the number density is 1 bacterium per 7 μm^2. It shows that increasing the body size of microrobots does not affect the motility notably but causes significant decrease in CMC, almost dropping to zero for a body size over 9 μm in diameter. Larger body size would increase the average distance between cells, making the attached bacteria sense rather different concentrations and hence reducing the synchronization of the signaling pathway behavior among them, as shown in Fig. 5.18. This indicates that, to achieve better chemotactic guidance, microrobots with smaller body size are strongly preferable. Finally, we examined the effect of the number of bacteria attached on chemotaxis and motility. As shown in Fig. 5.17(b), the CMC is generally insensitive to the number of bacteria, while the speed increases almost linearly with the number of bacteria. However, the potential interactions among the attached bacteria would become more and more prominent as the number of bacteria increases, and since such interactions are not accounted in our model, the trends in Fig. 5.17(b) might not hold true for any arbitrary ranges.

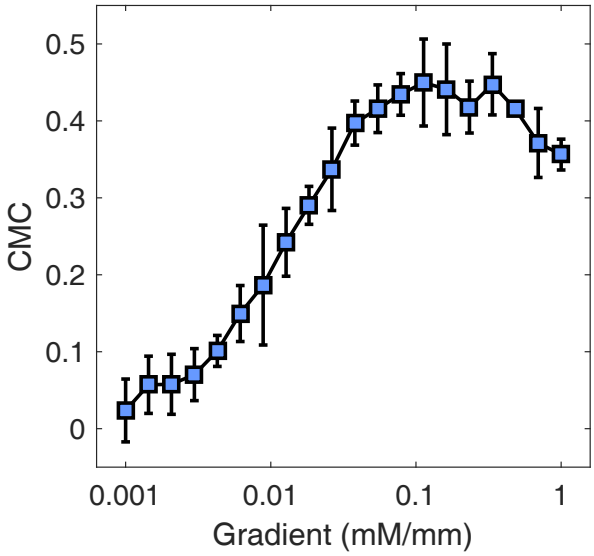

Figure 5.16: Chemotaxis response of microrobots over different attractant concentration profiles. Chemotaxis (CMC) is evaluated based on the final distribution of the simulated microrobots in the bounded channel. The configuration of the simulations is 3μm diameter microspheres, with around 5 bacteria attached to each microrobot.

5.6 Discussion and Summary

5.6.1 Discussion

We have developed a mathematical model to describe the propulsion mechanisms of a type of biohybrid microrobot driven by a few attached flagellated bacteria. The simulations of the model produces 3D trajectories and motility characteristics that resemble those of experiments. The model, in combination with the signaling pathway models of bacterial chemotaxis, also traces out the chemotaxis behavior of bacteria-driven microrobots reported by recent studies [36, 48, 49, 50, 51, 52, 56, 57]. The agreement between simulation and experiment implies that our model assumptions are reasonable and the model captures the fundamental biophysical mechanisms of of the system. Furthermore, our simulation data suggests that the seemingly cooperative chemotaxis of multiple bacteria attached to a microrobot could be explained by a synchronized signaling pathway response among these bacteria. However, proof of such predic-

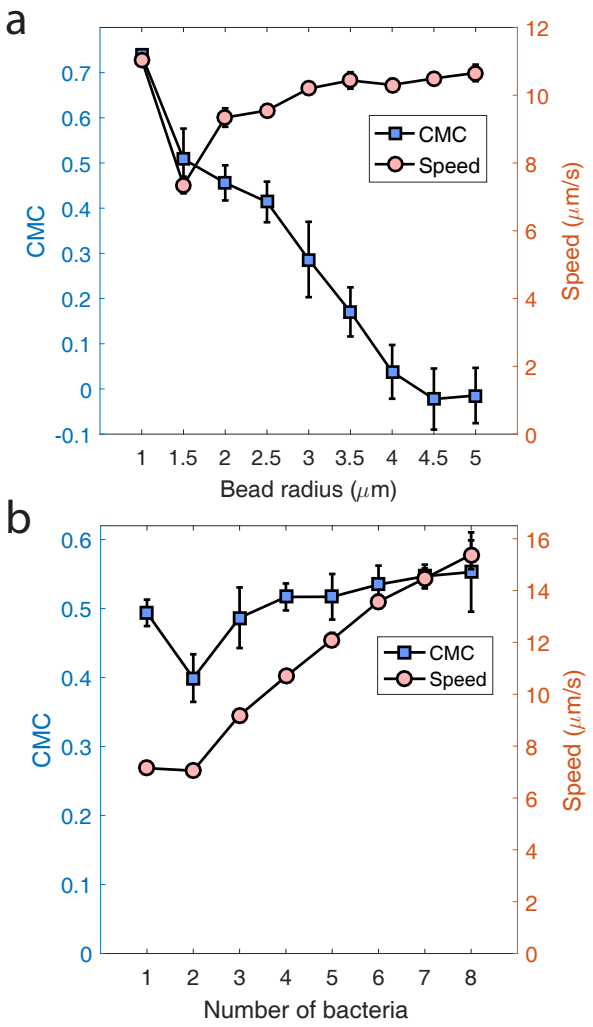

Figure 5.17: Performance of bacteria-driven microrobots on system parameters (simulation). Dependences of chemotaxis and motility on the size of microrobots (b) and the number of bacteria attached to a microrobot (c). Chemotaxis (CMC) is evaluated based on the final distribution of the simulated microrobots in the bounded channel. Unless studied as a parameter or stated otherwise, the default configuration of the simulations is 3μm diameter microspheres, with around 5 bacteria attached to each microrobot, and under an attractant gradient of 0.1 mM/mm.

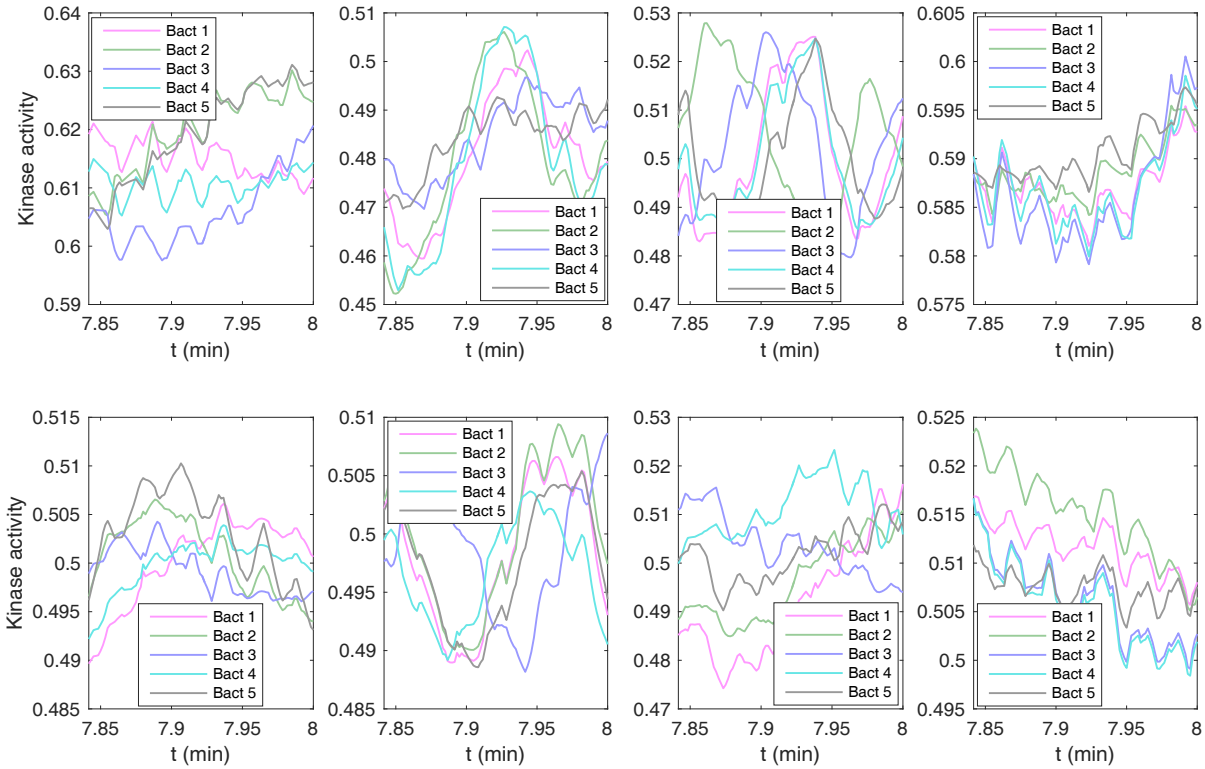

Figure 5.18: Unsynchronized MCP kinase activity of the multiple bacteria attached to a big microrobot (simulation). Eight different microrobots are presented, where each microrobot has five bacteria attached randomly in both position and orientation.

tion may need molecular level characterizations of the bacterial cells that are operated under a similar condition. In addition, the model reveals the potential dependences of the microrobots' performances (motility and chemmotactic guidability) on system parameters, including the attractant gradient, microrobot body size, and number of bacteria attached; such dependences may offer useful clues for the optimized design of bacteria-driven microrobots in future.

In the multi-cellular propulsion model, we adopted a relatively stiff model for the bacterial flagellar bundle, which has a preferred orientation that is not affected by its local fluid field. This choice, in part illuminated by an experimental observation, appears to be rather critical for the resulting motion behaviors of the model. However, the simulation based on a purely soft flagellar bundle model (i.e., the flagellar bundle is aligned with its local flow) demonstrates a similar level of chemotaxis as the stiff flagella model. This implies that a predefined flagellar bundle orientation is not a necessity to generate chemotactic drift for the model, although it might be the case that flagellar bundles bear their own preferred orientations, and so is the preferred orientations of flagellar filaments. Besides, the consideration of flagellar oscillation in the model serves to represent the noise in the real system, and including it could introduce minor irregularities to the helical shaped trajectories, but does not fundamentally alter the average motion behavior or chemotaxis of the simulated system. The flagellar motor reaction torque, however, is essential for producing the helical shaped trajectories. This has been proven on single bacterium-driven microrobots: failure to include the motor reaction torque would yield circular trajectories in our simulation, instead of the helical motions observed experimentally.

Although the motion of bacteria-driven microrobots is highly stochastic over long timescales, their short-term motion could be rather deterministic, as shown by the helical-shaped tracks in [34] and this study. Previous models [53, 123] for bacteria-driven microrobots, fail to reproduce the recurrent helical shapes along the swimming trajectories; instead, purely stochastic motions over all timescales were simulated by these models. The major cause of their failures is oversimplified representation of biophysical components in the system. For example, both

models describe each bacterium attached to a microrobot as a single point force exerted on the microrobot, ignoring the motor reaction torque(s) associated with the rotating flagellar bundle (or flagella). In addition, considerations of stochastic/noisy contributions could possibly smear the short-term deterministic behaviors. In the model by Cho et al., part of the propulsion on microrobots was contributed from the free-swimming bacteria, by stochastically colliding with the microrobots [123]. Likewise, a Brownian effect was considered in the model by Arabagi et al. [53]. As our major goal is investigating how propulsion is generated for microrobots driven by multiple attached bacteria, other unrelated contributions were mostly ruled out in both simulations and experiments.

Bacteria naturally sense temporal changes of an attractant concentration, by comparing the presently sensed value with that of the immediate past; this temporal sensing ability allows them to sense spatially varying signals by constantly moving around. Therefore, in a given spatial concentration gradient, the magnitude of the temporal gradient seen by a bacterium is dependent on its swimming speed, and hence the chemotactic response is speed dependent. Fig. 5.19 shows the signaling pathway states of two bacteria with rather different swimming speed, 2 μm/s and 20 μm/s, but under a same linear chemoattractant gradient; clearly, the one with higher swimming speed manifests a significantly stronger signaling pathway response. It follows from this observation that the chemotaxis of bacteria-driven microrobots should also be speed dependent: the higher the swimming speed, the stronger the chemotactic response, as demonstrated in Fig. 5.13(c). From the perspective of design, within a certain range, optimizing the swimming speed of bacteria-driven microrobots is expected to enhance their chemotactic guidability. Potential methods to enhance the speed of bacteria-driven microrobots include patterning the attachment location of bacteria on microrobots, aligning the attached bacteria, and using species with higher motility.

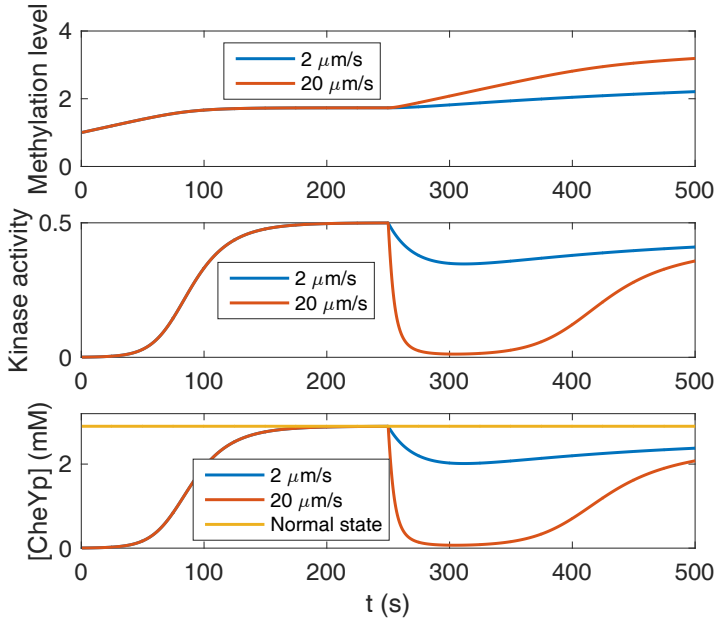

Figure 5.19: Dependency of signaling pathway response on bacterial swimming speed under a linear spacial concentration gradient, where a stronger response is observed on the bacteria with higher speed.

5.6.2 Summary

Despite the large body of experimental work on biohybrid microsystems, few studies have focused on theoretical modeling of such systems, which is essential for us to understand their underlying functioning mechanisms and hence design them optimally for a given application task. Therefore, this chapter focuses on developing a mathematical model to describe the 3D motion and the chemotaxis of a type of widely studied biohybrid microrobot, where spherical microparticles are driven by multiple attached bacteria. The model was developed based on the biophysical observations of the experimental system and has been validated by comparing the model simulation with experimental 3D swimming trajectories and other motility characteristics, including mean squared displacement (MSD), speed, diffusivity, and turn angle. The chemotaxis results of bacteria-driven microrobots from the model simulation also agree well with the experiments, where a collective chemotactic behavior among multiple bacteria is observed. The simulation result implies that such collective chemotaxis behavior is due

to a synchronized signaling pathway across the multiple bacteria attached to the same microrobot. Furthermore, by simulating the model, we studied the dependences of the motility and the chemotaxis of the microrobots on certain system parameters, such as the attractant concentration gradient, microrobot's body size, and number of attached bacteria, towards an optimized design of such biohybrid system. The optimized microrobots would be used in targeted cargo, e.g., drug, imaging agent, gene, and RNA, transport and delivery inside the stagnant or low-velocity fluids of the human body as one of their potential future biomedical application. The developed model not only helps us gain more insights into the biophysical mechanisms of bacteria-driven microrobots, but also serve as a potential means to optimize the design of such systems.

Chapter 6

Conclusions and Future Work

6.1 Conclusions

Biohybrid microrobots have shown the potential of overcoming the grand challenges in miniaturization of on-board actuation and power supply. Flagellated bacteria are among the leading candidates for the actuators of biohybrid swimming microrobots. However, bacteria propulsion maintains high intrinsic stochasticity, which constitutes a major reason why the motion of bacteria-driven microrobots are hard to regulate at the swarm level by conventional methods, such as magnetic steering. Instead, this thesis focuses on addressing the motion guiding of bacteria-driven microrobots using the natural taxis behaviors of free-swimming bacteria. Critical questions regarding this topic have been approached systematically, such as (a) how to find an optimal concentration profile used for motion guiding of bacteria-driven microrobots, (b) what could be the guiding performances and the physical mechanisms of the typical taxes, such as chemotaxis and pH-taxis, in bacteria-driven microrobots, and (c) how to biophysically model the bacteria-driven microrobotic system to describe its motion and chemotaxis.

The first task addressed was to develop a systematic method to characterize chemotaxis in free-swimming bacteria. To this end, we have proposed an experimental and modeling framework which characterizes the chemotactic motion of a typical flagellated bacterial species, such

as *E. coli* and *S. marcescens*, under a linear concentration gradient of a canonical chemoattractant, such as L-aspartate and L-serine. Specifically, the framework first measures the *chemotactic velocity* of the species across different linear concentration gradients of the chemoattractant, generating a chemotaxis response curve, and the result is then fitted by a bacterial chemotaxis signaling pathway model to determine the model parameters that are specific to the species. We demonstrated the framework by characterizing the chemotaxis of *S. marcescens* against L-aspartate. The chemotactic response of *S. marcescens* was quantified over a range of concentration gradients (10^{-3} to 5 mM/mm) and average concentrations (0.5×10^{-3} to 2.5 mM). Through the analysis of a large number of bacterial swimming trajectories, the tumble rate of the bacteria was found to have a significant bias with respect to their swimming directions. The optimal concentration gradient of L-aspartate that yielded the highest chemotactic velocity was 0.2 mM/mm. We also verified the relative gradient sensing machinery in the chemotaxis of *S. marcescens* by measuring the change of V_C against the average concentration and the gradient. The signaling pathway model with fitted parameters agreed with the experimental results, and thereby describes the chemotaxis of *S. marcescens* towards L-aspartate biophysically. Finally, we showed that our measurements based on the individual bacteria in a population lead to the determination of the motility coefficient μ (7.25×10^{-6} cm^2/s) of the population. The proposed chemotaxis characterization framework can also be readily adapted to study other bacterial tactic behaviors, such as pH-taxis and salt-taxis.

The second task addressed was to study the chemotaxis of a multi-bacteria driven microrobotic system. Using the bacterial chemotaxis characterization framework, we first studied the chemotactic response of *S. marcescens* towards a potent chemoattractant L-serine and determined the optimal concentration gradient to be 0.1 mM/mm. Under this optimal concentration profile, in a microrobotic system driven by multiple *S. marcescens* bacteria, we quantified the chemotactic drift of the microrobots and elucidated the physical mechanisms of the chemotactic motion by the statistical analysis of over a thousand swimming trajectories of the bacteria-

driven microrobots. Our results showed that the microrobots had a strong heading preference for moving up the L-serine gradient, while their speeds did not change considerably when moving up and down the gradient; therefore, the heading bias was the major factor that produced the chemotactic drift. The heading direction of a microrobot was found to be significantly more persistent when it was moving up the L-serine gradient than traveling down the gradient; this effect caused the apparent heading preference of the microrobots and is the crucial physical mechanism that drives the chemotactic drift in the bacteria-driven microrobots. Additionally, we found that the chemotactic drift velocity of the microrobots increases superquadratically with their mean swimming speed, suggesting that chemotaxis could be enhanced by designing and building faster microrobots.

Besides chemotaxis, the third task addressed was exploring the potential of utilizing the ambient pH to guide the motion of bacteria-driven microrobots. Under three specifically configured pH gradients, we demonstrated that the bacteria-driven microrobots, the same prototype used in chemotaxis study, exhibit both unidirectional and bidirectional pH-tactic behaviors, which were also observed in free-swimming bacteria. Thus, we were able to conclude that the ambient pH constitutes an effective means to perform motion guiding of the microrobotic swarms. Through trajectory analysis, we found that a swimming direction bias and a speed bias are two major factors that contribute to their tactic drift motion. The motion analysis of the microrobots also shed important light on the propulsion dynamics of flagellated bacteria as micro-actuators. The resemblances in the physical mechanism of the chemotaxis and pH-taxis in bacteria-driven microrobots suggest that a similar signaling pathway is shared between bacterial chemotaxis and pH-taxis. By demonstrating pH-taxis in the bacteria-driven microrobots and identifying the physical mechanism of the pH-tactic motion, we have opened up an new avenue towards improving the control of bacteria-driven microrobots. Presumably, if it is possible to tune the preferred pH of bacteria by genetic engineering, bacteria-driven microrobots could potentially be guided by the pH gradients induced by cancerous cells inside the human body and thus

perform targeted delivery of cargoes, such as drugs, genes, and stem cells.

The fourth task addressed was to develop a biophysical model to describe the propulsion and the chemotaxis in bacteria-driven microrobots, on the one hand to better understand the system and on the other hand for optimizing the design of the system in terms of its performances. To this end, we have developed a bacterial propulsion model that describes the exertion of forces and torques on a microrobot by its attached bacterial motors. This model, in combination with a bacterial chemotaxis signaling pathway model, not only simulated the helical featured trajectories observed in experiments, but also traced out a chemotactic drift motion similar to that of a real physical system. The model simulation also suggests that a synchronization of the signaling pathways of the multiple bacteria attached to a microrobot could be the mechanism of the associated bacterial collective chemotaxis in bacteria-driven microrobots, but further biophysical characterizations are necessary to corroborate this conjecture. Furthermore, by simulating the model, we studied the dependences of the motility and the chemotactic guidability of bacteria-driven microrobots on their common system parameters, including the chemoattractant gradient, microrobot body size, and number of attached bacteria, which results could be important guidelines for the design optimization of bacteria-driven microrobots.

6.2 Future Work

6.2.1 Salt-Taxis of Bacteria-Driven Microrobots

Ambient salt concentration is crucial for bacteria to maintain a normal cellular osmotic pressure and the intracellular ion concentrations. It has been shown that *E. coli* is attracted by the optimum concentrations of various salts [128], and such tactic behaviors are highly dependent on MCP-I, a major chemotaxis receptor. Therefore, it is reasonable to expect that appropriate salt concentration profiles can be used to guide the motion of bacteria-driven microrobots. However, this has never been tested out experimentally. Although salt-taxis potentially shares the

signaling pathway with chemotaxis, it might elicit different levels of tactic behavior in bacteria and thus becomes meaningful to be characterized separately. Here, we qualitatively demonstrate that a salt gradient can bias the distribution of a swarm of bacteria-driven microrobots, which were initially randomly distributed in the gradient. Specifically, in the three-channel microfluidic device, we input the source channel with a motility buffer (0.01 M KH_2PO_4, 0.067 M NaCl, 10^{-4} M EDTA, pH = 7.0), which is a saline buffer used to maintain the normal bacterial activity, input the sink channel with DI water (close to zero concentrations for any salts), and loaded the sample (middle) channel with the same motility buffer containing a concentration of bacteria-driven microrobots. A flow rate of 5 μl/min were maintained in the source and sink channels, while the middle channel was quiescent. Fig. 6.1 shows the effect of the ambient salt concentration profile on the distribution of the bacteria-driven microrobots, where the upside of the sample channel corresponds to a salt level close to the motility buffer while the bottom side has a much lower salt-level.

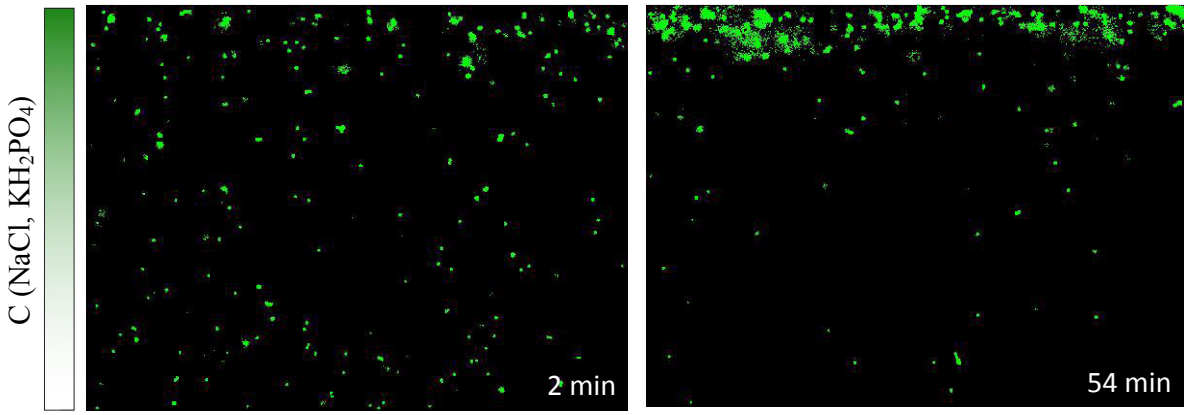

Figure 6.1: Distribution of microrobots in the sample channel at (a) 2 min and (b) 54 min after the initiation of the source and sink flows.

Suggested future work includes:

- Characterizing prominent salt-taxis in free-swimming bacteria using the chemotaxis characterization framework;

- Observing the salt-tactic drift process of bacteria-driven microrobots;
- Quantifying the salt-taxis of bacteria-driven microrobots by trajectory analysis and comparing the results with those of chemotaxis and pH-taxis.

6.2.2 Optimize the Design of Bacteria-Driven Microrobots

Parameter study via experiment

Our model for bacteria-driven microrobots only describes their motion and the chemotaxis behavior given that the assumptions are satisfied. These assumptions, however, might be only weakly held or even broken down in some situations of the real system development. For example, the model assumes negligible effect from the interactions among the attached bacteria on a microrobot, but the interactions could become a statistically significant effect as the distances among the bacteria decrease, which could be caused by increasing the average number of the bacteria attached to a microrobot. In such situations, the model simulation could be inaccurate or fail to describe the physical system and hence could not direct the design optimization sensibly. As a result, it is necessary to experimentally characterize the dependencies of the system performances on its major design parameters. Such experimental characterizations can solve the following problems:

- Determining the scope of the system parameters in which the model describes the system;
- Refining the model by including more biophysical components to fit experimental observations;
- Optimizing the design of bacteria-driven robots based on experimental parameter studies.

Here, we show an example of how the parameter study based on experiments could help reveal more biophysical aspects of the system of bacteria-driven microrobot. Fig. 6.2(a) shows the dependency of the swimming trajectory of a microrobot on the average number of attached bacteria, a major system parameter. It can be seen that the more the bacteria attached, the more

random the swimming motion is, manifested by the degraded regularity (helical shape) along the swimming trajectories as the number of attached bacteria increases. This could be due to the reason discussed previously, namely, the emergent interactions among the attached bacteria on a microrobot. As our model ignores such interactions, the model simulation, showed in Fig. 6.2(b), seems to have failed to capture this trend, although it agrees well with the experiment on the helical-shaped trajectories when there are only a few bacteria attached. If the bacterial interactions could be accounted appropriately in the model, it is expected to describe the system regardless of the number of bacteria attached (or the density of bacterial attachment).

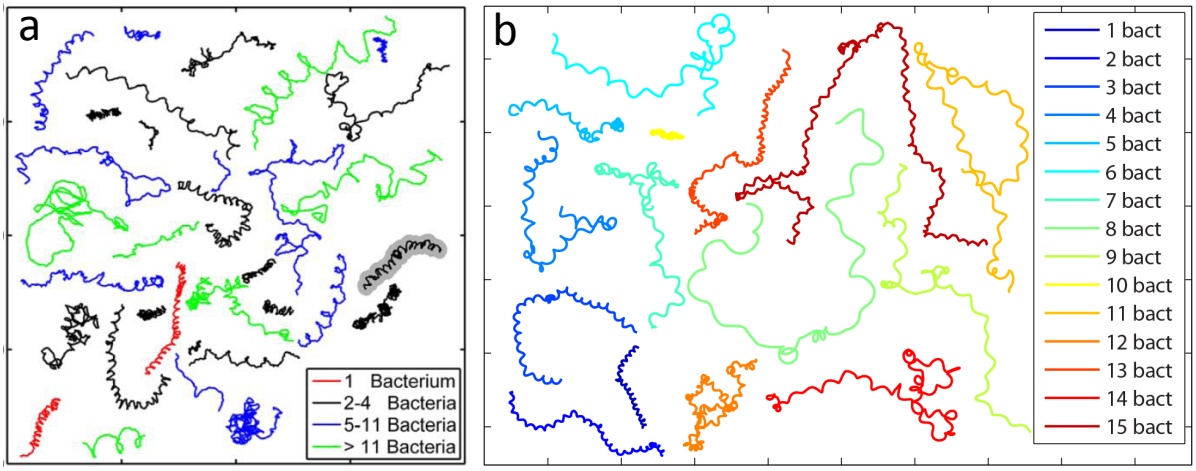

Figure 6.2: Effect of the number of attached bacteria on the swimming motion of bacteria-driven microrobots, (a) experimental characterization of 5μm diameter microrobots propelled by *S. marcescens* bacteria (figure reprinted from [34]) and (b) preliminary simulation based on the current model of bacteria-driven microrobots.

Towards a more accurate model

The current bacterial propulsion model is a coarse grained model in that it treats each bacterium as a single flagellar motor transitioning between run and tumble states. However, typical flagellated bacteria like *E. coli* usually have multiple flagellar filaments which rotate respectively about the cell body, and their rotation directions (either in CCW or CW) may not be

synchronized. The multi-flagellar configuration brings more intermediate motion states to free-swimming bacteria during the transition between the two classically acknowledged states, run and tumble. Along a running state, in which all flagella rotate in CCW, a tumble event can be triggered by one or more of the involved flagella change their rotation directions into CW. Relatively recently, the flagellar observation based on high-resolution fluorescent microscopy sheds more details on the state transition in multi-flagellated bacteria [121]; Fig. 6.3 depicts the idealized state transition sequence in an multi-flagellated bacteria, caused by the rotation direction change of a single flagellar motor. It can be seen that a multi-flagellated bacterium is not an ideal two-state machine, as has been adopted in our model, but a rather complicated and stochastic system with more states and state transition dynamics.

Moreover, in consequence of the multi-flagella of a bacterium, the bacterial state transition can be more complicated than the case of single-flagellum, as the tumble events can be triggered under different situations and behave heterogeneously. Sneddon et al. studied the effect of multi-falgella on a cell's swimming state transition using a probabilistic model [82]: compared to a single flagellar motor, multiple flagellar motors can help on reducing the latency of chemotactic response while shorten the expected length of runs. Based on their conclusion, the motion of bacteria-driven microrobots is likely to be less persistent due to the increased state transition frequency of the attached bacteria, although we are not clear about the exact implications of multi-flagella on the bacterial propulsion in bacteria-driven microrobots. To reveal this, we suggest to treat each bacterium as a multi-flagellated propeller and model its state transition accordingly. However, an appropriate model of the state transition under the condition of multi-flagella may need further experimental characterizations on the corresponding behaviors.

Accounting for the above complications would inevitably increase the complexity and stochasticity of the model, because each multi-flagellated bacterial propeller could have many states along its propulsion and which in turn allows for a significant number of state combinations for a multi-bacteria driven microrobotic system. However, it might be just the case that

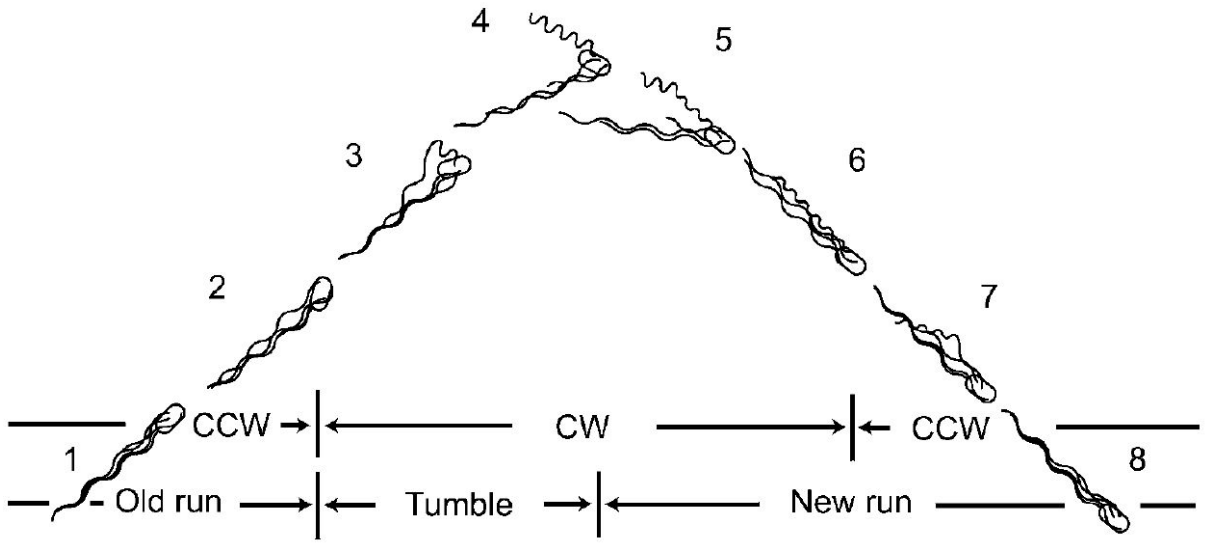

Figure 6.3: Idealized sequence of events in a tumble caused by the reversal of a single motor (figure reprinted from [121]). The upper timeline indicates the direction of motor rotation of the flagellum causing the tumble, and the lower timeline indicates the motion state of the bacterium. The transition can be documented in eight stages: (1) the bacterium in running state with all flagella rotate CCW; (2) a flagellum switching its rotation from CCW to CW, causing the flagellar bundle to start unbundling and the cell body to deflect slightly; (3) the flagellum starting to transition from the left-handed normal form to the right-handed semicoiled form, associated with a large deflection of the cell body; (4) completion of the morphological transition of the flagellum to be semicoiled and reorientation of the cell body; (5) movement of the cell body in the new orientation, propelled by a semicoiled (partially in curly-1 form) flagellum and a normal bundle by the rest of the flagella; (6) the flagellum completely in curly-1 form and be flexible enough to wrap around the bundle; (7) the flagellum switching its rotation from CW to CCW, causing its morphological transition from curly-1 to normal left-handed; and (8) the bacterium back to normal run after the flagellum joining the bundle.

such biohybrid systems would exhibit a broad spectrum of behaviors and high stochasticity, as has been observed on the microrobots driven by relatively more (over 10) bacteria.

Suggested future work includes:

- Experimentally characterize the dependences of the swimming behaviors (trajectory, motility and chemotaxis) of bacteria-driven microrobots on their major design parameters, such as body size, bacterial attachment density, and attachment patterning;
- Compare the parameter study results between experiments and model simulations, and improve the model by accounting for more biophysical aspects of the system, such as the interactions among the bacteria on a microrobot;
- Refine the model by including more characterized bacterial transition states and being aware of the consequences of multi-flagella on a cell's state transition dynamics and propulsion.

List of Author's Articles Related to This Thesis

- **J. Zhuang**, G. Wei, R. W. Carlsen, M. R. Edwards, R. Marculescu, P. Bogdan, and M. Sitti, "Analytical modeling and experimental characterization of chemotaxis in Serratia marcescens," *Physical Review E*, vol. 89, 2014.
- **J. Zhuang**, R. W. Carlsen, and M. Sitti, "pH-taxis of biohybrid microsystems," *Scientific Reports*, vol. 5, 2015.
- **J. Zhuang** and M. Sitti, "Chemotaxis of biohybrid multiple bacteria-driven microswimmers," *Scientific Reports*, vol. 5, 2016.
- **J. Zhuang**, BW Park, and M. Sitti, "Propulsion and chemotaxis in bacteria-driven microswimmers: modeling and experiments," *in preparation*, 2017.
- M. R. Edwards, R. W. Carlsen, **J. Zhuang**, and M. Sitti, "Swimming motility characterization of Serratia marcescens," *Journal of Micro-Bio Robotics*, vol. 9, pp. 47-60, 2014.

- E. Diller, **J. Zhuang**, G. Z. Lum, M. R. Edwards, and M. Sitti, "Continuously distributed magnetization profile for millimeter-scale elastomeric undulatory swimming," *Applied Physics Letters*, vol. 104, 2014.
- BW Park, **J. Zhuang**, O. Yasa, and M. Sitti, "Engineered bacteria-driven microswimmers for active targeted drug delivery," *submitted*, 2017.
- R. W. Carlsen, M. R. Edwards, **J. Zhuang**, C. Pacoret, and M. Sitti, "Magnetic steering control of multi-cellular biohybrid microswimmers," *Lab on a Chip*, vol. 14, pp. 3850-3859, 2014.
- Babak Mostaghaci , Oncay Yasa, **J. Zhuang**, and M. Sitti, "Bioadhesive bacterial microswimmers for targeted drug delivery in the urinary and gastrointestinal tracts," *submitted*, 2016.
- H. Koorehdavoudi, P. Bogdan, G. Wei, R. Marculescu, **J. Zhuang**, R. W. Carlsen, and M. Sitti, "Multi-scale analysis reveals nonlinear and multi-fractal behavior in chemotactic bacteria population dynamics," *submitted*, 2016.

Appendix A

Bacteria and Growth Conditions

A.1 Serratia marcescens

Serratia marcescens (ATCC 274, American Type Culture Collection, Manassas, VA) was initially cultured to exponential growth phase in a nutrient broth (25 g Difco LB Miller Broth and 1 L deionized (DI) water, pH 7.0) on a shaker at 37 °C for 3.5 - 4 hours. Then an aliquot of 2.0 μL of the liquid culture was transfered to an agar plate (25 g Difco LB Miller Broth, 6 g Bacto Agar, 5 g glucose, 1 L de-ionized water), followed by an incubation of the agar plate at 30°C for 16 - 20 hours. After the incubation, the culture is ready for use. Fig. A.1 shows a sample plate culture of *S. marcescens* with different colony locations labeled.

A.2 Escherichia coli

The *Escherichia coli* (*E. coli*) strain MG1655 (Yale University, New Haven, USA) was cultured in 5 ml LB broth (Sigma-Aldrich, St. Louis, MO, USA) at 30 °C for 4 h to its exponential growth phase. The resulted liquid culture was directly diluted with PBS (Thermo Fisher Scientific, Waltham, Massachusetts, USA) for the chemotaxis response test of free-swimming bacteria. To prepare bacteria-driven microswimmers, the resulted liquid culture was washed with PBS

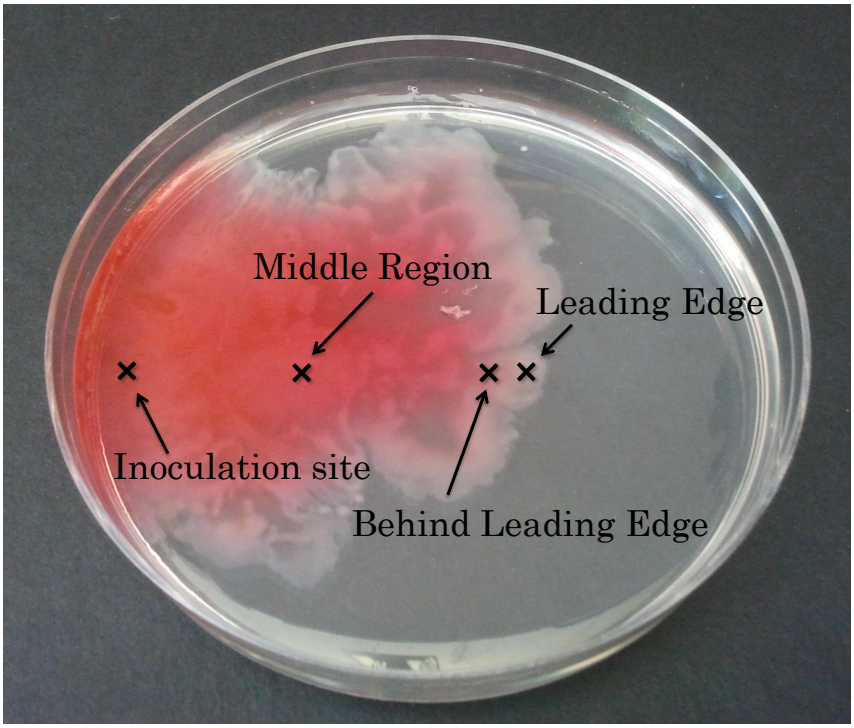

Figure A.1: A plate culture of *S. marcescens*.

before mixed with particles.

Appendix B

Microfluidic Setup

The microfluidic concentration gradient generator was assembled from a molded hydrogel chip containing the channel features [71]. To mold the hydrogel chip, a master mold of the channel patterns was fabricated by a standard soft lithography method. To increase the channel height, two layers of photoresist were used. The hydrogel chips were molded by pouring 4% (weight ratio) hot agarose (Eiken Chemical Co.) solution onto the silicon master mold, where the channel patterns were surrounded by polydimethylsiloxane (PDMS) enclosures. After the agarose gels were cured, the outlets of the source and sink channels were punched into the gel. Subsequently, the sample solution to be tested was carefully pipetted into the sample (middle) channel ensuring that there was neither overflow nor much vacant space left in the sample channel. The channel-patterned side of the agarose gel was covered with a cover slip immediately after loading the sample solution. To complete the assembly of the gradient generator, the agarose gel chip (including the diffusion section, a PDMS enclosure and a cover slip) was sandwiched between two acrylic panels. Fig. B.1 shows the detailed configuration of the microfluidic device.

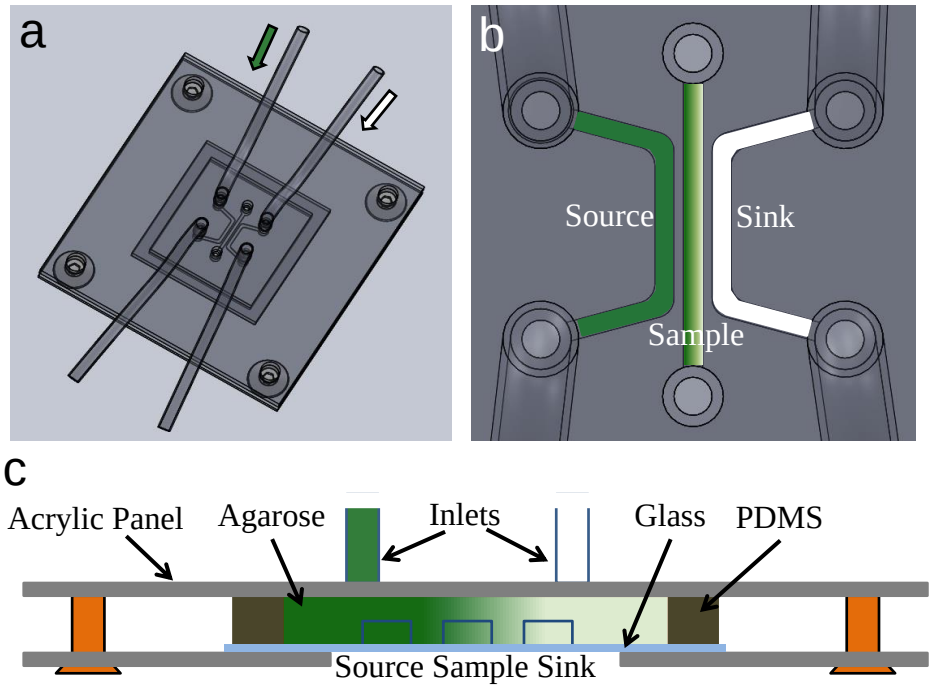

Figure B.1: Three-channel microfluidic concentration gradient generator. (a) 3D, (b) *top*, and (c) *side views* of the device. A linear gradient is created in the sample channel between the high concentration source channel and lower concentration sink channel.

Appendix C

Tracking Algorithms

Algorithm 1 2D and 3D tracking

```
function TRACKBACT(v)                ▷ Where v - the input video, a list of 2D or 3D frames
    maxDist ← max distance between two consecutive frames
    n ← total number of frames
    openTracks ← empty list of open tracks
    closedTracks ← empty list of closed tracks
    Bacts ← empty list of bacterial cell bodies
    for i = 1 : n do
        tmpOpenTracks ← empty list of open tracks for next iteration
        frame ← v.getFrame(i)
        if 2D then
            bacts ← findBactPoses2D(frame)
        else if 3D then
            bacts ← findBactPoses3D(frame)
        end if
        for pos : bacts do
            closestTrack ← None
            curMinDist ← maxDist
            for track : openTracks do
                curDist ← findDistance(track.getPos(end), pos)
                if curDist < curMinDist then
                    closestTrack ← track
                    curMinDist ← curDist
                end if
            end for
            if closestTrack ≠ None then
                track.append(pos)
                tmpOpenTracks.add(openTracks.remove(track))
            else
                tmpOpenTracks.add(createNewTrack(pos))
            end if
        end for
        closedTracks.addAll(openTracks)
        openTracks ← tmpOpenTracks
    end for
    closedTracks.addAll(openTracks)
    return closedTracks
end function
```

Algorithm 2 Find island features in a 2D image

1: **function** FINDBACTPOS2D(img) ▷ Where img - the input image, a 2D matrix (or 3D if chromatic)
2: $img \leftarrow basicFilter(img)$
3: $bactPoses \leftarrow regionProps(img)$ ▷ Where $regionProps()$ is a standard Matlab function
4: **end function**

Algorithm 3 Find 3D position in z-stack (DHM)

function FINDBACTPOS3D(imgStack) ▷ Where imgStack - the input image stack, a list of images
    $max2DDist \leftarrow$ max 2D (xy) distance to consider z-correlation
    $n \leftarrow$ total number height of z-stack
    $openPoses \leftarrow$ empty list of open poses
    $closedPoses \leftarrow$ empty list of closed poses
    $poses2D \leftarrow$ empty list of feature positions in 2D
    for $i = 1 : n$ **do**
        $tmpOpenPoses \leftarrow$ empty list of open positions for next a higher stack
        $img \leftarrow v.getStack(i)$
        $poses2D \leftarrow findBactPoses2D(img)$
        for $pos2D : poses2D$ **do**
            $closestPos \leftarrow$ None
            $curMinDist \leftarrow max2DDist$
            for $pos : openPoses$ **do**
                $curDist \leftarrow findDistance(pos.get2DPos(end), pos2D)$
                if $curDist < curMinDist$ **then**
                    $closestPos \leftarrow Pos$
                    $curMinDist \leftarrow curDist$
                end if
            end for
            if $closestPos \neq$ None **then**
                $pos.append(pos2D)$
                $tmpOpenPoses.add(openPoses.remove(pos))$
            else
                $tmpOpenPoses.add(createNewPos(pos2D))$
            end if
        end for
        $closedPoses.addAll(openPoses)$
        $openPoses \leftarrow tmpOpenPoses$
    end for
    $closedPoses.addAll(openPoses)$
    $poses3D \leftarrow$ empty list of 3D positions
    for $pos : closedPoses$ **do**
        $poses3D.add(pos.get3DPos())$
    end for
    return $poses3D$
end function

Algorithm 4 Connect tracks with small gaps

function CONNECTTRACK(tracks) ▷ Where tracks - 2D or 3D raw tracks
    $unconnectedTracks \leftarrow sortByStartingFrame(tracks)$
    $connectedTracks \leftarrow emptylistoftracks$
    $maxFrameGap \leftarrow$ max frame gap to be considered connected
    $maxDist \leftarrow$ max 2D or 3D distance to be considered connected
    while $unconnectedTracks.size() \geq 2$ **do**
        $curTrack \leftarrow unConnectedTracks.get(1)$ ▷ Get the first track
        $closestTrack \leftarrow$ None
        $curMinDist \leftarrow maxDist$
        for $i = 2 : unconnectedTracks.size()$ **do**
            $tmpTrack \leftarrow unconnectedTrack.get(i)$
            if $tmpTrack.startFrame \leq curTrack.endFrame + maxFrameGap$ **then**
                $curDist \leftarrow getDistanceGap(curTrack, tmpTrack)$
                if $curDist \leq curMinDist$ **then**
                    $curMinDist \leftarrow curDist$
                    $closestTrack \leftarrow tampTrack$
                end if
            end if
        end for
        if $closestTrack \neq$ None **then**
            $connect(curTrack, closestTrack)$ ▷ Simply connect the two tracks by putting linearly spaced vector over the frame gap, and update the start and end frame of *curTrack*
            $unconnectedTracks.remove(closestTrack)$
        else
            $connectedTracks.add(unconnectedTracks.remove(curTrack))$
        end if
    end while
    $connectedTracks.addAll(unconnectedTracks)$
    return $connectedTracks$
end function

Appendix D

Microrobot Simulation Flow

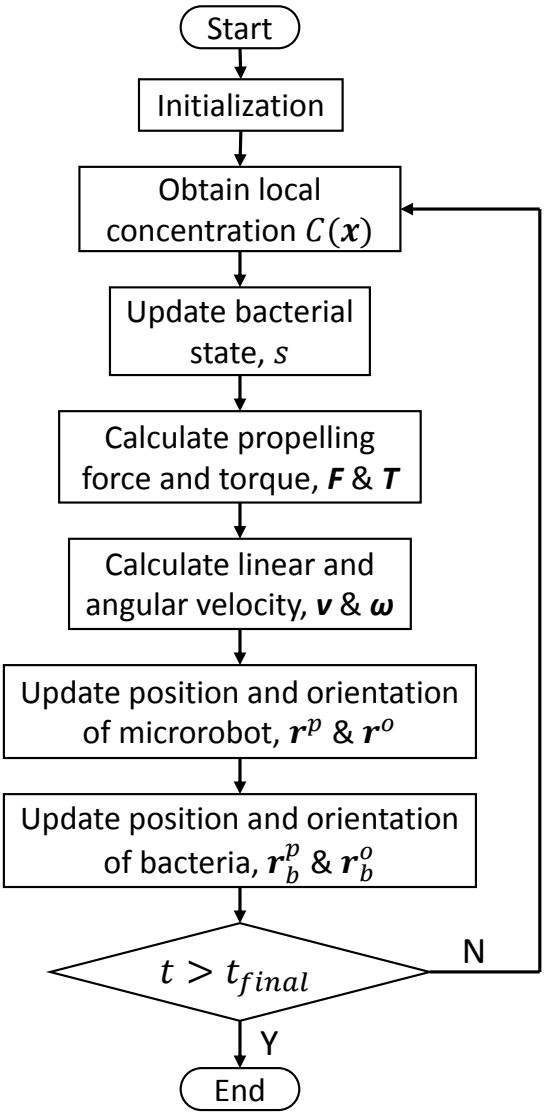

Figure D.1: Flowchart showing the simulation procedure of bacteria-driven microrobots.

Bibliography

[1] M. Sitti, "Voyage of the microrobots," *Nature*, vol. 458, no. 7242, pp. 1121–1122, 2009. 1.2.1, 1.2.2

[2] R. Fernandes and D. H. Gracias, "Toward a miniaturized mechanical surgeon," *Materials Today*, vol. 12, pp. 14–20, Oct. 2009. 1.2.1

[3] B. J. Nelson, I. K. Kaliakatsos, and J. J. Abbott, "Microrobots for minimally invasive medicine.," *Annual review of biomedical engineering*, vol. 12, pp. 55–85, Aug. 2010. 1.2.1

[4] M. A. Zeeshan, K. Shou, K. M. Sivaraman, T. Wuhrmann, S. Pané, E. Pellicer, and B. J. Nelson, "Nanorobotic drug delivery If I only had a heart…," *Materials Today*, vol. 14, pp. 54–54, Jan. 2011. 1.2.1

[5] S. Fusco, F. Ullrich, J. Pokki, G. Chatzipirpiridis, B. Özkale, K. M. Sivaraman, O. Ergeneman, S. Pané, and B. J. Nelson, "Microrobots: a new era in ocular drug delivery," *Expert Opin Drug Deliv.*, vol. 11(11), pp. 1815–26, 2014. 1.2.1

[6] K. Ishiyama, M. Sendoh, A. Yamazaki, and K. Arai, "Swimming micro-machine driven by magnetic torque," *Sensors and Actuators A: Physical*, vol. 91, pp. 141–144, June 2001. 1.2.1

[7] L. Zhang, J. Abbott, L. Dong, B. Kratochvil, D. Bell, and B. Nelson, "Artificial bacterial flagella: fabrication and magnetic control," *Applied Physics Letters*, vol. 94, p. 064107, 2009. 1.2.1

[8] A. Ghosh and P. Fischer, "Controlled propulsion of artificial magnetic nanostructured propellers.," *Nano letters*, vol. 9, pp. 2243–5, June 2009. 1.2.1

[9] S. Tottori, L. Zhang, F. Qiu, K. K. Krawczyk, A. Franco-Obregón, and B. J. Nelson, "Magnetic helical micromachines: Fabrication, controlled swimming, and cargo transport," *Advanced Materials*, vol. 24, pp. 811–816, 2012. 1.2.1

[10] R. Dreyfus, J. Baudry, M. L. Roper, M. Fermigier, H. a. Stone, and J. Bibette, "Microscopic artificial swimmers.," *Nature*, vol. 437, pp. 862–5, Oct. 2005. 1.2.1

[11] S. Martel, J. Mathieu, O. Felfoul, A. Chanu, E. Aboussouan, S. Tamaz, P. Pouponneau, G. Beaudoin, G. Soulez, and M. Mankiewicz, "Automatic navigation of an untethered device in the artery of a living animal using a conventional clinical magnetic resonance imaging system," *Applied Physics Letters*, vol. 90, p. 114105, 2007. 1.2.1

[12] M. Kummer, J. Abbott, B. Kratochvil, R. Borer, A. Sengul, and B. Nelson, "OctoMag: An electromagnetic system for 5-DOF wireless micromanipulation," *Robotics, IEEE Transactions on*, vol. 26, no. 6, pp. 1006–1017, 2010. 1.2.1

[13] S. Floyd, C. Pawashe, and M. Sitti, "Modeling and Experimental Characterization of an Untethered Magnetic Micro-Robot," *The International Journal of Robotics Research*, vol. 28, no. 8, pp. 1077–1094, 2009. 1.2.1

[14] B. Donald and C. Levey, "An untethered, electrostatic, globally controllable MEMS micro-robot," *Journal of Microelectromechanical Systems*, vol. 15, no. 1, pp. 1–15, 2006. 1.2.1

[15] O. Sul, M. Falvo, R. Taylor, S. Washburn, and R. Superfine, "Thermally actuated untethered impact-driven locomotive microdevices," *Applied Physics Letters*, vol. 89, p. 203512, 2006. 1.2.1

[16] A. Búzás, L. Kelemen, A. Mathesz, L. Oroszi, G. Vizsnyiczai, T. Vicsek, and P. Ormos, "Light sailboats: Laser driven autonomous microrobots," *Applied Physics Letters*,

vol. 101, no. 4, p. 041111, 2012. 1.2.1

[17] W. Hu, K. S. Ishii, and A. T. Ohta, "Micro-assembly using optically controlled bubble microrobots," *Applied Physics Letters*, vol. 99, no. 9, p. 094103, 2011. 1.2.1

[18] J. Li, T. Li, T. Xu, M. Kiristi, W. Liu, Z. Wu, and J. Wang, "Magneto-acoustic hybrid nanomotor," *Nano Letters*, vol. 15, pp. 4814–4821, 2015. 1.2.1

[19] A. a. Solovev, Y. Mei, E. Bermúdez Ureña, G. Huang, and O. G. Schmidt, "Catalytic microtubular jet engines self-propelled by accumulated gas bubbles.," *Small (Weinheim an der Bergstrasse, Germany)*, vol. 5, pp. 1688–92, July 2009. 1.2.1

[20] N. Darnton, L. Turner, K. Breuer, and H. C. Berg, "Moving fluid with bacterial carpets," *Biophys J*, vol. 86, pp. 1863–70, Mar. 2004. 1.2.2, 2.1, 4.1

[21] S. Tung and J. W. Kim, "Microscale hybrid devices powered by biological flagellar motors," *IEEE Transactions on Automation Science and Engineering*, vol. 3, pp. 260–263, 2006. 1.2.2

[22] S. Martel, C. C. Tremblay, S. Ngakeng, and G. Langlois, "Controlled manipulation and actuation of micro-objects with magnetotactic bacteria," *Appl Phys Lett*, vol. 89, no. 23, p. 233904, 2006. 1.2.2, 1.2.3, 5.1

[23] Y. Hiratsuka, M. Miyata, T. Tada, and T. Q. P. Uyeda, "A microrotary motor powered by bacteria," *Proceedings of the National Academy of Sciences*, vol. 103, pp. 13618–23, Sept. 2006. 1.2.2, 2.1

[24] B. Behkam and M. Sitti, "Bacterial flagella-based propulsion and on/off motion control of microscale objects," *Appl Phys Lett*, vol. 90, no. 2, p. 023902, 2007. 1.2.2, 2.1, 5.1, 5.2.1

[25] M. J. Kim and K. S. Breuer, "Controlled mixing in microfluidic systems using bacterial chemotaxis," *Anal. Chem*, vol. 79, pp. 955–959, 2007. 1.2.2

[26] M. J. Kim and K. S. Breuer, "Microfluidic pump powered by self-organizing bacteria,"

Small, vol. 4, pp. 111–8, Jan. 2008. 1.2.2, 2.1

[27] L. Angelani, R. D. Leonardo, and G. Ruocco, "Self-starting micromotors in a bacterial bath," *Physical Review Letters*, vol. 102, p. 048104, 2009. 1.2.2, 2.1, 5.1

[28] A. Sokolov, M. M. Apodaca, B. A. Grzybowski, and I. S. Aranson, "Swimming bacteria power microscopic gears," *Proc Natl Acad Sci USA*, vol. 107, pp. 969–74, Jan. 2010. 1.2.2, 2.1, 5.1

[29] S. J. Park, H. Bae, J. Kim, B. Lim, J. Park, and S. Park, "Motility enhancement of bacteria actuated microstructures using selective bacteria adhesion," *Lab on a Chip*, vol. 10, pp. 1706–1711, 2010. 1.2.2, 2.1, 3.2, 5.1, 5.2.1

[30] R. Di Leonardo, L. Angelani, D. Dell'Arciprete, G. Ruocco, V. Iebba, S. Schippa, M. P. Conte, F. Mecarini, F. De Angelis, and E. Di Fabrizio, "Bacterial ratchet motors," *Proc Natl Acad Sci U S A*, vol. 107, pp. 9541–5, May 2010. 1.2.2, 2.1, 5.1

[31] R. Fernandes, M. Zuniga, F. R. Sassine, M. Karakoy, and D. H. Gracias, "Enabling cargo-carrying bacteria via surface attachment and triggered release," *Small*, vol. 7, pp. 588–92, Mar. 2011. 1.2.2, 2.1, 5.1

[32] M. Kojima, Z. Zhang, M. Nakajima, and T. Fukuda, "High efficiency motility of bacteria-driven liposome with raft domain binding method," *Biomed Microdevices*, vol. 14, pp. 1027–1032, 2012. 1.2.2, 2.1, 3.3, 5.1, 5.2.1

[33] Q. Ma, C. Chen, S. Wei, C. Chen, L.-F. Wu, and T. Song, "Construction and operation of a microrobot based on magnetotactic bacteria in a microfluidic chip," *Biomicrofluidics*, vol. 6, pp. 24107–2410712, June 2012. 1.2.2, 2.1, 5.1

[34] M. R. Edwards, R. Wright Carlsen, and M. Sitti, "Near and far-wall effects on the three-dimensional motion of bacteria-driven microbeads," *Appl Phys Lett*, vol. 102, no. 14, p. 143701, 2013. 1.2.2, 1.2.4, 2.1, 3.3, 3.7.1, 5.1, 5.2.1, 5.4.2, 5.6.1, 6.2

[35] N. Koumakis, A. Lepore, C. Maggi, and R. D. Leonardo, "Targeted delivery of colloids

by swimming bacteria," *Nature Communications*, vol. 4, 2013. 1.2.2, 5.1, 5.2.1

[36] S. J. Park, S.-H. Park, S. Cho, D.-M. Kim, Y. Lee, S. Y. Ko, Y. Hong, H. E. Choy, J.-J. Min, J.-O. Park, and S. Park, "New paradigm for tumor theranostic methodology using bacteria-based microrobot," *Scientific Reports*, 2013. 1.2.2, 1.2.3, 5.1, 5.2.1, 5.6.1

[37] O. Felfoul, M. Mohammadi, S. Taherkhani, D. de Lanauze, Y. Z. Xu, D. Loghin, S. Essa, S. Jancik, D. Houle, M. Lafleur, L. Gaboury, M. Tabrizian, N. Kaou, M. Atkin, T. Vuong, G. Batist, N. Beauchemin, D. Radzioch, and S. Martel, "Magneto-aerotactic bacteria deliver drug-containing nanoliposomes to tumour hypoxic regions," *Nature Nanotechnology*, 2016. 1.2.2, 1.2.3, 5.1

[38] D. B. Weibel, P. Garstecki, D. Ryan, W. R. DiLuzio, M. Mayer, J. E. Seto, and G. M. Whitesides, "Microoxen: Microorganisms to move microscale loads," *Proc Natl Acad Sci U S A*, vol. 102, pp. 11963–11967, 2005. 1.2.2

[39] J. Xi, J. J. Schmidt, and C. D. Montemagno, "Self-assembled microdevices driven by muscle," *Nature Materials*, vol. 4, pp. 180–184, 2005. 1.2.2

[40] J. Kim, J. Park, S. Yang, J. Baek, B. Kim, S. H. Lee, E.-S. Yoon, K. Chun, and S. Park, "Establishment of a fabrication method for a long-term actuated hybrid cell robot," *Lab on a Chip*, vol. 7, pp. 1504–1508, 2007. 1.2.2, 2.1

[41] A. W. Feinberg, A. Feigel, S. S. Shevkoplyas, S. Sheehy, G. M. Whitesides, and K. K. Parker, "Muscular thin films for building actuators and powering devices," *Science*, vol. 317, pp. 1366–1370, 2007. 1.2.2

[42] B. J. Williams, S. V. Anand, J. Rajagopalan, and M. T. A. Saif, "A self-propelled biohybrid swimmer at low reynolds number," *Nature Communications*, vol. 5, pp. 1–8, 2014. 1.2.2

[43] E. B. Steager, M. S. Sakar, D. H. Kim, V. Kumar, G. J. Pappas, and M. J. Kim, "Electrokinetic and optical control of bacterial microrobots," *J Micromech Microeng*, vol. 21,

p. 035001, Mar. 2011. 1.2.2, 2.1

[44] R. W. Carlsen and M. Sitti, "Bio-hybrid cell-based actuators for microsystems," *Small*, vol. 10, pp. 3831–3851, 2014. 1.2.2

[45] V. Magdanz, S. Sanchez, and O. G. Schmidt, "Development of a sperm-flagella driven micro-bio-robot," *Advanced Materials*, vol. 25, pp. 6581–6588, 2013. 1.2.2, 1.2.3

[46] R. W. Carlsen, M. R. Edwards, J. Zhuang, C. Pacoret, and M. Sitti, "Magnetic steering control of multi-cellular bio-hybrid microswimmers," *Lab on a Chip*, vol. 14, pp. 3850–3859, 2014. 1.2.3, 5.1, 5.2.1

[47] C.-Y. Chen, C.-F. Chen, Y. Yi, L.-J. Chen, L.-F. Wu, and T. Song, "Construction of a microrobot system using magnetotactic bacteria for the separation of staphylococcus aureus," *Biomed Microdevices*, vol. 16, pp. 761–70, 2014. 1.2.3

[48] M. Traoré, A. Sahari, and B. Behkam, "Computational and experimental study of chemotaxis of an ensemble of bacteria attached to a microbead," *Phys Rev E Stat Nonlin Soft Matter Phys*, vol. 84, pp. 1–6, Dec. 2011. 1.2.3, 2.1, 3.1, 3.7.1, 5.1, 5.2.1, 5.6.1

[49] D. Kim, A. Liu, E. Diller, and M. Sitti, "Chemotactic steering of bacteria propelled microbeads," *Biomed Microdevices*, vol. 14, pp. 1009–1017, Sept. 2012. 1.2.3, 2.1, 3.1, 3.7.1, 5.1, 5.2.1, 5.6.1

[50] D. Park, S. J. Park, S. Cho, Y. Lee, Y. K. Lee, J.-J. Min, B. J. Park, S. Y. Ko, J.-O. Park, and S. Park, "Motility analysis of bacteria-based microrobot (bacteriobot) using chemical gradient microchamber," *Biotechnology and Bioengineering*, vol. 111(1), pp. 134–143, 2014. 1.2.3, 2.1, 3.1, 3.2, 3.7.1, 3.7.1, 5.1, 5.2.1, 5.6.1

[51] A. Sahari, M. A. Traore, B. E. Scharf, and B. Behkam, "Directed transport of bacteria-based drug delivery vehicles: bacterial chemotaxis dominates particle shape," *Biomed Microdevices*, vol. 16(5), pp. 717–725, 2014. 1.2.3, 2.1, 3.1, 3.2, 3.7.1, 3.7.1, 5.1, 5.2.1, 5.6.1

[52] S. Suh, M. A. Traore, and B. Behkam, "Bacterial chemotaxis-enabled autonomous sorting of nanoparticles of comparable sizes," *Lab on a Chip*, 2016. 1.2.3, 5.1, 5.2.1, 5.6.1

[53] V. Arabagi, B. Behkam, E. Cheung, and M. Sitti, "Modeling of stochastic motion of bacteria propelled spherical microbeads," *Journal of Applied Physics*, vol. 109, p. 114702, 2011. 1.2.4, 2.1, 5.1, 5.6.1

[54] J. Zhuang, G. Wei, R. W. Carlsen, M. R. Edwards, R. Marculescu, P. Bogdan, and M. Sitti, "Analytical modeling and experimental characterization of chemotaxis in serratia marcescens," *Physical Review E*, vol. 89, 2014. 1.3, 3.3, 4.1, 5.4.1

[55] M. R. Edwards, R. W. Carlsen, J. Zhuang, and M. Sitti, "Swimming motility characterization of *Serratia marcescens*," *Journal of Micro-Bio Robotics*, vol. 9, pp. 47–60, 2014. 1.3, 2.4.1, 2.4.2, 3.3, 3.3, 3.6.2, 3.7.1, 4.1

[56] J. Zhuang and M. Sitti, "Chemotaxis of bio-hybrid multiple bacteria-driven microswimmers," *Scientific Reports*, 2016. 1.3, 5.1, 5.2.1, 5.3.1, 5.4.3, 5.13, 5.6.1

[57] J. Zhuang, R. W. Carlsen, and M. Sitti, "ph-taxis of biohybrid microsystems," *Scientific Reports*, vol. 5, 2015. 1.3, 4.1, 5.1, 5.2.1, 5.4.3, 5.6.1

[58] B. Behkam and M. Sitti, "Effect of quantity and configuration of attached bacteria on bacterial propulsion of microbeads," *Appl Phys Lett*, vol. 93, no. 22, p. 223901, 2008. 2.1, 5.1

[59] S. Martel, M. Mohammadi, O. Felfoul, Z. Lu, and P. Pouponneau, "Flagellated Magnetotactic Bacteria as Controlled MRI-trackable Propulsion and Steering Systems for Medical Nanorobots Operating in the Human Microvasculature," *Int J Rob Res*, vol. 28, pp. 571–582, Apr. 2009. 2.1

[60] T.-H. Tran, D. Hyung Kim, J. Kim, M. Jun Kim, and D. Byun, "Use of an AC electric field in galvanotactic on/off switching of the motion of a microstructure blotted by *Serratia marcescens*," *Appl Phys Lett*, vol. 99, no. 6, p. 063702, 2011. 2.1

[61] M. S. Sakar, E. B. Steager, D. H. Kim, A. A. Julius, M. Kim, V. Kumar, and G. J. Pappas, "Modeling, control and experimental characterization of microbiorobots," *Int J Rob Res*, vol. 30, pp. 647–658, Jan. 2011. 2.1

[62] M. Kojima, Z. Zhang, M. Nakajima, K. Ooe, and T. Fukuda, "Construction and evaluation of bacteria-driven liposome," *Sensors and Actuators B: Chemical*, 2013. 2.1, 5.1, 5.2.1

[63] J. S. Dickson and M. Koohmaraie, "Cell surface charge characteristics and their relationship to bacterial attachment to meat surfaces," *Applied and Environmental Microbiology*, vol. 55, pp. 832–836, 1989. 2.1, 4.1

[64] L. Xie, T. Altindal, S. Chattopadhyay, and X.-L. Wu, "Bacterial flagellum as a propeller and as a rudder for efficient chemotaxis," *Proc Natl Acad Sci USA*, vol. 108, pp. 2246–2251, 2011. 2.1

[65] M. Theves, J. Taktikos, V. Zaburdaev, H. Stark, and C. Beta, "A bacterial swimmer with two alternating speeds of propagation," *Biophysical Journal*, vol. 105, pp. 1915 – 1924, 2013. 2.1

[66] H. C. Berg and D. A. Brown, "Chemotaxis in *Escherichia coli* analysed by three-dimensional tracking," *Nature*, vol. 239, pp. 500–504, 1972. 2.1, 2.5.2, 2.6.1, 3.1, 3.3, 4.1, 5.1, 5.1

[67] D. A. Brown and H. C. Berg, "Temporal stimulation of chemotaxis in *Escherichia coli*," *Proc. Nat. Acad. Sci. USA*, vol. 71, pp. 1388–1392, 1974. 2.1, 3.1, 4.6.1

[68] M. A. Rivero, R. T. Tranquillo, H. M. Buettner, and D. A. Lauffenburger, "Transport mmodel for chemotactic cell-populations based on individual cell behavior," *Chem. Eng. Sci*, vol. 44, pp. 2281–2897, 1989. 2.1, 2.2.2, 3.3, 4.5.6, 5.4.2

[69] H. B. Mao, P. S. Cremer, and M. D. Manson, "A sensitive, versatile microfluidic assay for bacterial chemotaxis," *Natl. Acad. Sci.*, vol. 100, pp. 5449–5454, 2003. 2.1, 2.6.1

[70] J. Diao, L. Young, S. Kim, E. A. Fogarty, S. M. Heilman, P. Zhou, M. L. Shuler, M. Wu, and M. P. DeLisa, "A three-channel microfluidic device for generating static linear gradients and its application to the quantitative analysis of bacterial chemotaxis," *Lab on a Chip*, vol. 6, pp. 381–388, 2006. 2.1, 2.2.2, 2.5.2, 2.6.1, 2.6.1, 4.2, 5.4.1

[71] S.-Y. Cheng, S. Heilman, M. Wasserman, S. Archer, M. L. Shulerac, and M. Wu, "A hydrogel-based microfluidic device for the studies of directed cell migration," *Lab Chip*, vol. 7, pp. 763–769, 2007. 2.1, 2.2.2, 2.3.2, 2.5.1, 2.6.1, 4.2, 5.4.1, B

[72] T. Ahmed and R. Stocker, "Experimental verification of the behavioral foundation of bacterial transport parameters using microfluidics," *Biophysical Journal*, vol. 95, pp. 4481–4493, 2008. 2.1, 2.2.2, 2.5.1, 2.5.2, 3.3, 5.4.3

[73] T. Long and R. M. Ford, "Enhanced transverse migration of bacteria by chemotaxis in a porous t-sensor," *Environ. Sci. Technol.*, vol. 43, p. 15461552, 2009. 2.1

[74] H. Jeon, Y. Lee, S. Jin, S. Koo, C.-S. Lee, and J. Y. Yoo, "Quantitative analysis of single bacterial chemotaxis using a linear concentration gradient microchannel," *Biomed Microdevices*, vol. 11, pp. 1135–1143, 2009. 2.1, 2.3.2, 2.5.1, 2.6.1

[75] D. L. Englert, M. D. Manson, and A. Jayaraman, "Flow-based microfluidic device for quantifying bacterial chemotaxis in stable, competing gradients," *Appl. Environ. Microbiol.*, vol. 75, pp. 4557–4564, 2009. 2.1

[76] T. Ahmed, T. S. Shimizu, and R. Stocker, "Bacterial chemotaxis in linear and nonlinear steady microfluidic gradients," *Nano Lett.*, vol. 10(9), pp. 3379–3385, 2010. 2.1, 2.2.2, 2.5.1, 2.6.1

[77] Y. V. Kalinin, L. Jiang, Y. Tu, and M. Wu, "Logarithmic sensing in *Escherichia coli* bacterial chemotaxis," *Biophysical*, vol. 96, pp. 2439–2448, 2009. 2.1, 2.2.1, 2.2.1, 2.2.1, 2.2.1, 2.2.1, 2.2.2, 2.1, 2.5.2, 2.5.2, 2.6.1, 2.6.1, 3.3, 3.3, 5.2.2

[78] Y. Tu, "Quantitative modeling of bacterial chemotaxis: Signal amplification and accurate

adaptation," *Annual Review of Biophysics*, vol. 42, pp. 337–359, 2013. 2.2.1, 2.2.1

[79] R. G. Endres and N. S. Wingreen, "Precise adaptation in bacterial chemotaxis through "assistance neighborhoods"," *Proceedings of the National Academy of Sciences*, vol. 103, no. 35, pp. 13040–13044, 2006. 2.2.1, 5.1, 5.2.2

[80] N. Vladimirov, L. Løvdok, D. Lebiedz, and V. Sourjik, "Dependence of bacterial chemotaxis on gradient shape and adaptation rate," *PLoS Computational Biology*, vol. 4, no. 12, p. e1000242, 2008. 2.2.1

[81] L. Jiang, Q. Ouyang, and Y. Tu, "Quantitative modeling of escherichia coli chemotactic motion in environments varying in space and time," *PLoS Computational Biology*, vol. 6, no. 4, p. e1000735, 2010. 2.2.1, 2.2.1, 5.1, 5.2.2, 5.2.2, 5.2.2, 5.3.1, 5.4.1

[82] M. W. Sneddon, W. Pontius, and T. Emonet, "Stochastic coordination of multiple actuators reduces latency and improves chemotactic response in bacteria," *Proceedings of the National Academy of Sciences*, vol. 109, no. 3, pp. 805–810, 2012. 2.2.1, 6.2.2

[83] T. Duke, N. Le Novere, and D. Bray, "Conformational spread in a ring of proteins: a stochastic approach to allostery," *Journal of Molecular Biology*, vol. 308, no. 3, pp. 541–553, 2001. 2.2.1

[84] C. H. Hansen, R. G. Endres, and N. S. Wingreen, "Chemotaxis in escherichia coli: a molecular model for robust precise adaptation," *PLoS Computational Biology*, vol. 4, no. 1, p. e1, 2008. 2.2.1, 5.1, 5.2.2

[85] C. M. Khursigara, X. Wu, P. Zhang, J. Lefman, and S. Subramaniam, "Role of hamp domains in chemotaxis signaling by bacterial chemoreceptors," *Proceedings of the National Academy of Sciences*, vol. 105, no. 43, pp. 16555–16560, 2008. 2.2.1, 2.1, 5.1, 5.2.2, 5.2.2

[86] Y. Tu, T. S. Shimizu, and H. C. Berg, "Modeling the chemotactic response of escherichia coli to time-varying stimuli," *Proceedings of the National Academy of Sciences*, vol. 105,

no. 39, pp. 14855–14860, 2008. 2.2.1, 5.1, 5.2.2, 5.2.2

[87] A. Vaknin and H. C. Berg, "Physical responses of bacterial chemoreceptors," *Journal of Molecular Biology*, vol. 366, no. 5, pp. 1416–1423, 2007. 2.2.1

[88] N. Barkai and S. Leibler, "Robustness in simple biochemical networks," *Nature*, vol. 387, no. 6636, pp. 913–917, 1997. 2.2.1, 2.2.1

[89] H. Park, C. C. Guet, T. Emonet, and P. Cluzel, "Fine-tuning of chemotactic response in e. coli determined by high-throughput capillary assay," *Current microbiology*, vol. 62, no. 3, pp. 764–769, 2011. 2.2.1

[90] X. Zhu, G. Si, N. Deng, Q. Ouyang, T. Wu, Z. He, L. Jiang, C. Luo, and Y. Tu, "Frequency-dependent escherichia coli chemotaxis behavior," *Physical Review Letters*, vol. 108, no. 12, p. 128101, 2012. 2.2.1

[91] T. Emonet and P. Cluzel, "Relationship between cellular response and behavioral variability in bacterial chemotaxis," *Proceedings of the National Academy of Sciences*, vol. 105, no. 9, pp. 3304–3309, 2008. 2.2.1, 5.1, 5.2.2

[92] S. B. van Albada and P. R. ten Wolde, "Differential affinity and catalytic activity of chez in e. coli chemotaxis," *PLoS Computational Biology*, vol. 5, no. 5, p. e1000378, 2009. 2.2.1

[93] Y. Tu and G. Grinstein, "How white noise generates power-law switching in bacterial flagellar motors," *Physical Review Letters*, vol. 94, no. 20, p. 208101, 2005. 2.2.1

[94] M. W. Sneddon, J. R. Faeder, and T. Emonet, "Efficient modeling, simulation and coarse-graining of biological complexity with nfsim," *Nature Methods*, vol. 8, no. 2, pp. 177–183, 2010. 2.2.1, 5.1, 5.2.2, 5.2.2, 5.2.2

[95] P. Cluzel, M. Surette, and S. Leibler, "An ultrasensitive bacterial motor revealed by monitoring signaling proteins in single cells," *Science*, vol. 287, no. 5458, pp. 1652–1655, 2000. 2.2.1

[96] E. F. Keller and L. A. Segel., "Model for chemotaxis," *J. Theor. Biol*, vol. 30, pp. 225–234, 1971. 2.2.2

[97] K. C. Chen, R. M. Frod, and P. T. Cummings, "Perturbation expansion of alt's cell balance equations reduces to segel's one-dimensional equations for shallow chemoattractant gradients," *Nature. Appl. Math*, vol. 59, pp. 35–57, 1998. 2.2.2

[98] I. G. Portillo, D. Campos, and V. Mendéz, "Intermittent random walks: transport regimes and implications on search strategies," *Journal of Statistical Mechanics: Theory and Experiment*, p. P02033, 2011. 2.2.2

[99] F. Thiel, L. Schimansky-Geier, and I. M. Sokolov, "Anomalous diffusion in run-and-tumble motion," *Physical Review E*, vol. 86, p. 021117, 2012. 2.2.2

[100] G. Wei, P. Bogdan, and R. Marculescu, "Efficient modeling and simulation of bacteria-based nanonetworks with bnsim," *Selected Areas in Communications, IEEE Journal on*, vol. 31, no. 12, pp. 868–878, 2013. 2.5.2, 5.2.2, 5.2.2

[101] B. A. Mello and Y. Tu, "Effects of adaptation in maintaining high sensitivity over a wide range of backgrounds for *Escherichia coli* chemotaxis," *Biophysical Journal*, vol. 92, no. 7, pp. 2329–2337, 2007. 2.1

[102] P. Lewus and R. M. Ford, "Quantification of random motility and chemotaxis bacterial transport coefficients using individual-cell and population-scale assays," *Biotechnology and Bioengineering*, vol. 75, pp. 291–304, 2001. 2.5.2

[103] B. Behkam, *Bacteria as Actuators for Hybrid (Biotic/Abiotic) Swimming Micro-robots: Design, Modeling, and Implementation*. PhD thesis, Carnegie Mellon University, 2008. 3.2

[104] R. Mesibov and J. Adler, "Chemotaxis toward amino acids in *Escherichia coli*," *Journal of Bacteriology*, vol. 112(1), pp. 315–326, 1972. 3.3

[105] F. W. Dahlquist, R. A. Elwell, and P. S. Lovely, "Studies of bacterial chemotaxis in

defined concentration gradients. a model for chemotaxis toward l-serine," *Journal of Supramolecular Structure*, vol. 4, pp. 329–342, 1976. 3.3

[106] R. R. Vuppula, M. S. Tirumkudulu, and K. V. Venkatesh, "Chemotaxis of *Escherichia coli* to l-serine," *Physical Biology*, vol. 7, p. 026007, 2010. 3.3

[107] J. Adler, "Chemoreceptors in bacteria," *Science*, vol. 166, pp. 1588–1597, 1969. 3.3

[108] S. Clarke and J. D. E. Koshland, "Membrane receptors for aspartate and serine in bacterial chemotaxis," *Journal of Biological Chemistry*, vol. 254(19), pp. 9695–9702, 1979. 3.3

[109] Y. Kalinin, S. Neumann, V. Sourjik, and M. Wu, "Responses of escherichia coli bacteria to two opposing chemoattractant gradients depend on the chemoreceptor ratio," *Journal of Bacteriology*, vol. 192(7), pp. 1796–1800, 2010. 3.3

[110] Y. Yang and V. Sourjik, "Opposite responses by different chemoreceptors set a tunable preference point in escherichia coli ph taxis," *Molecular Microbiology*, vol. 86(6), pp. 1482–1489, 2012. 3.7.1, 4.1, 4.1, 4.3.1, 4.3.2

[111] B. Hu and Y. Tu, "Behaviors and strategies of bacterial navigation in chemical and non-chemical gradients," *PLOS Computational Biology*, vol. 10(6), 2014. 3.7.1, 4.1, 4.1, 4.6.1

[112] I. R. Booth, "Regulation of cytoplasmic ph in bacteria," *Microbiological Reviews*, vol. 49(4), pp. 359–378, 1985. 4.1

[113] T. A. Krulwich, G. Sachs, and E. Padan, "Molecular aspects of bacterial ph sensing and homeostasis," *Nature Reviews Microbiology*, vol. 9, pp. 330–343, 2011. 4.1

[114] B. Hu and Y. Tu, "Precision sensing by two opposing gradient sensors: How does escherichia coli find its preferred ph level?," *Biophysical Journal*, vol. 105, pp. 276 – 285, 2013. 4.1, 4.3.1, 4.3.2

[115] I. F. Tannock and D. Rotin, "Acid ph in tumors and its potential for therapeutic exploita-

tion," *Cancer Research*, vol. 49, pp. 4373–4384, 1989. 4.1

[116] J. Griffiths, "Are cancer cells acidic?," *British Journal of Cancer*, vol. 64, pp. 425–427, 1991. 4.1

[117] B. He, Z. Wang, C. Liu, Y. Li, and R. Shen, "Swimming behavior analysis based on bacterial chemotaxis in solution," *Journal of Bionic Engineering*, vol. 9, pp. 315–321, 2012. 4.2

[118] A. V. Singh and M. Sitti, "Bacteria-driven particles: Patterned and specific attachment of bacteria on biohybrid bacteria-driven microswimmers," *Advanced Healthcare Materials*, vol. 5, no. 18, pp. 2306–2306, 2016. 5.1

[119] M. Sitti, H. Ceylan, W. Hu, J. Giltinan, M. Turan, S. Yim, and E. Diller, "Biomedical applications of untethered mobile milli/microrobots," *Proceedings of the IEEE*, vol. 103, pp. 205–224, Feb 2015. 5.1

[120] Z. Hosseinidoust, B. Mostaghaci, O. Yasa, B.-W. Park, A. V. Singh, and M. Sitti, "Bio-engineered and biohybrid bacteria-based systems for drug delivery," *Advanced Drug Delivery Reviews*, vol. 106, Part A, pp. 27 – 44, 2016. Biologically-inspired drug delivery systems. 5.1

[121] N. C. Darnton, L. Turner, S. Rojevsky, , and H. C. Berg, "On torque and tumbling in swimming *Escherichia coli*," *Journal of Bacteriology*, 2007. 5.1, 5.4.2, 5.1, 6.2.2, 6.3

[122] S. Chattopadhyay, R. Moldovan, C. Yeung, , and X. L. Wu, "Swimming efficiency of bacterium *Escherichia coli*," *Proceedings of the National Academy of Sciences*, 2006. 5.1

[123] S. Cho, Y. J. Choi, S. Zheng, J. Han, S. Y. Ko, J.-O. Park, and S. Parkb, "Modeling of chemotactic steering of bacteria-based microrobot using a population-scale approach," *Biomicrofluidics*, 2015. 5.1, 5.6.1

[124] G. H. Wadhams and J. P. Armitage, "Making sense of it all: bacterial chemotaxis," *Nature*

Reviews Molecular Cell Biology, 2004. 5.1

[125] J. Monod, J. Wyman, and J.-P. Changeux, "On the nature of allosteric transitions: A plausible model," *Journal of Molecular Biology*, 1965. 5.2.2

[126] B. A. Mello and Y. Tu, "Effects of adaptation in maintaining high sensitivity over a wide range of backgrounds for¡ i¿ escherichia coli¡/i¿ chemotaxis," *Biophysical Journal*, vol. 92, no. 7, pp. 2329–2337, 2007. 5.2.2

[127] J. R. Howse, R. A. L. Jones, A. J. Ryan, T. Gough, R. Vafabakhsh, and R. Golestanian, "Self-motile colloidal particles: From directed propulsion to random walk," *Phys. Rev. Lett.*, vol. 99, p. 048102, Jul 2007. 5.4.2

[128] Y. Qi and J. Adler, "Salt taxis in *Escherichia coli* bacteria and its lack in mutants," *Proc Natl Acad Sci U S A*, vol. 86, pp. 8358–8362, 1989. 6.2.1